Dissertation

submitted to the
Combined Faculties for the Natural Sciences and for Mathematics
of the Ruperto-Carola University of Heidelberg, Germany
for the degree of
Doctor of Natural Sciences

Put forward by
Dipl.-Phys. Rebecca Boll
Born in Hagen

Oral examination on July 2, 2014

Imaging Molecular Structure with Photoelectron Diffraction

Referees: Prof. Dr. Joachim Ullrich

Prof. Dr. Selim Jochim

Abstract

The possibility to study the structure of polyatomic gas-phase molecules by photoelectron diffraction is investigated with the goal of developing a method capable of imaging ultrafast photochemical reactions with femtosecond temporal and sub-Ångström spatial resolution. The fluorine 1*s*-level of adiabatically laser-aligned 1-ethynyl-4-fluorobenzene (C_8H_5F) molecules was ionized by X-ray pulses from the *Linac Coherent Light Source* Free-Electron Laser, and the angular distributions of photoelectrons with kinetic energies between 30 and 60 eV were recorded by velocity map imaging. Comparison with density functional theory calculations allows relating the measured distributions to the molecular structure. The results of an IR-pump, X-ray-probe experiment on aligned 1,4-dibromobenzene ($C_6H_4Br_2$) molecules are presented to explore the potential of photoelectron diffraction for time-resolved imaging. The influence of the alignment laser pulse on the pumping and probing step is discussed. Laser-alignment is contrasted with determination of the molecular orientation by photoelectron-photoion coincidences for an exemplary data set on 1-ethynyl-4-fluorobenzene molecules recorded at the PETRA III synchrotron. Both methods are evaluated with respect to their applicability to record time-dependent snapshots of molecular structure. The results obtained in this work indicate possible future avenues for investigating ultrafast molecular dynamics using X-ray Free-Electron Lasers.

Zusammenfassung

In dieser Arbeit wird untersucht, inwieweit die geometrische Struktur mehratomiger Moleküle in der Gasphase mittels Photoelektronenbeugung bestimmt werden kann. Das Ziel ist es, eine Methode zu finden, die eine Zeitauflösung von wenigen Femtosekunden und eine räumliche Auflösung von unter einem Ångström bietet, um schnell ablaufende chemische Prozesse auf atomarer Ebene abzubilden. 1-Ethinyl-4-fluorbenzol (C_8H_5F) Moleküle wurden mit einem Laserpuls adiabatisch ausgerichtet und die Fluor 1*s*-Schale durch einen Röntgenpuls des *Linac Coherent Light Source* Freie-Elektronen-Lasers ionisiert. Die Winkelverteilungen der resultierenden Photoelektronen mit kinetischen Energien von 30 bis 60 eV wurden mit der *Velocity-Map-Imaging* Technik gemessen und mit Hilfe von Dichtefunktionaltheorie mit der Molekülstruktur verknüpft. Außerdem werden Resultate eines Pump-Probe Experimentes diskutiert, in dem ausgerichtete 1,4-Dibrombenzol ($C_6H_4Br_2$) Moleküle zunächst mit einem infraroten Laserpuls dissoziiert und anschließend die Brom 2*p*-Schale von einem Röntgenpuls ionisiert wurde. Es wird gezeigt, dass der Laserpuls, der für die Molekülausrichtung benutzt wird, sowohl den Pump-, als auch den Probeprozess beeinflussen kann. Der Laserausrichtung wird als Alternative eine an der Synchrotronquelle PETRA III durchgeführte Elektronen-Ionen Koinzidenzmessung gegenübergestellt und die Methoden werden hinsichtlich ihrer Eignung zum Untersuchen von Molekülgeometrie beurteilt. Die Resultate zeigen Konzepte auf, wie zukünftig Moleküldynamik untersucht werden könnte.

Contents

About Trotting Horses

In October 1878, Scientific American published an article on a new technique to visualize motion by taking multiple snapshot photographs with only two millisecond exposure time, invented by Eadweard Muybridge [1]. These photographs would later become famous as the first movie ever taken, answering the question whether, at any point in time, all four feet of a trotting horse are off the ground at the same time. In this article, it is stated:

> *The most careless observer of these figures will not fail to notice that the conventional figure of a trotting horse in motion does not appear in any of them, nor anything like it. Before these pictures were taken no artist would have dared to draw a horse as a horse really is when in motion.* [...]
>
> [The photographs] *not only make a notable addition to our stock of positive knowledge, but must also effect a radical change in the art of depicting horses in motion.* [...] *However truthful, an artist's work cannot have the convincing force of a photograph.*

Today, more than a century later, these statements are still true, demonstrating the necessity for the development of new techniques to look at processes that already seemed commonly understood with a new precision, from a new perspective, and thereby revealing new, unexpected insights. Only the direct observation of an object in motion can provide full understanding of how it functions. Even if, *a priori*, it may not be clear what to expect from this new technique, history shows that almost every time a more precise observation became technically possible, something surprising was found.

Macroscopic mechanical and biological processes have been extensively studied and much is known already about microscopic chemical processes, for example in living cells. Now the question of *how does this work?* has reached the fundamental level of the movement of single nuclei and electrons. Complex macroscopic processes, like photosynthesis, could suddenly become fundamentally better understood if it was possible to watch every step of it on an atomic length and time scale. The presented work is meant to take a small step forward in this direction.

1 Imaging Ultrafast Chemical Reactions

Systematic observation of nature and understanding of its underlying concepts is the most fundamental driving force behind all natural sciences. Every time a new, more precise observation method is developed, a leap of insight usually follows. The revelation that all matter consists of a limited number of atoms changed our perception of the world radically – but to resolve the structure of an object on the atomic level is not enough to comprehend how it functions. In order to fully understand a process, such as photosynthesis, the underlying *dynamics* are essential. To see nature in action, on the atomic level, a tool needs to be developed that can resolve the movement of single atoms, and thus record real-time movies of the forming and breaking of chemical bonds.

1.1 Introduction to Femtochemistry

Traditionally, chemical reactions are studied in a before-after-fashion. Reactants and products are often well-characterized, but what happens in between, on the atomic level, usually remains unobserved. Figure 1.1 illustrates the photoelimination reaction of a 1,2-diiodoperfluoroethane molecule after absorption of a UV photon. Both iodine atoms are dissociated from the molecule, but it was long unknown through which of the two predicted reaction intermediates the transition proceeds [2].

Photochemistry is omnipresent in everyday life, as nearly every organism requires sunlight to survive. Through photoabsorption, it is possible to promote a molecule to a desired final state by tuning the photon energy to a specific transition. Recent research activities even aim at manipulating the probability of specific reaction

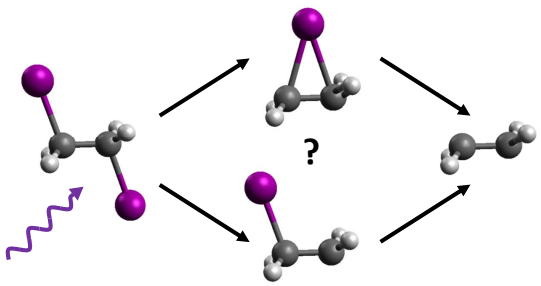

Figure 1.1: Schematic of the photoelimination reaction in 1,2-diiodoperfluoroethane ($C_2F_4I_2$). The equilibrium geometry of the molecule is depicted on the left, and the final state after absorption of a UV photon on the right. Two possible reaction intermediates have been predicted (middle). For a direct measurement of the intermediate structure, see section 1.2.2.

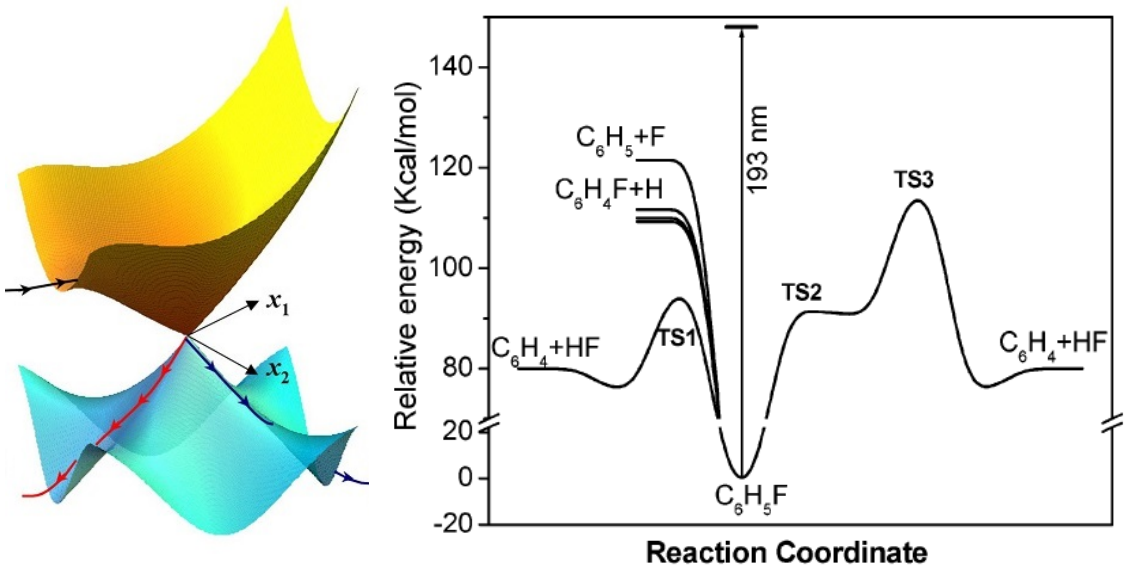

(a) (b)

Figure 1.2: (a) Schematic illustration of the ground (blue) and excited state (yellow) of a molecule that form a conical intersection. The excited-state reaction pathway and two ground-state reaction pathways are shown. The figure is taken from reference [3]. (b) Different reaction pathways of fluorobenzene (C_6H_5F) upon UV absorption. The dissociation to the end products $C_6H_4 + HF$ can occur via different transition states TS1, TS2, TS3. The figure is taken from reference [4].

pathways by tailoring the light pulse to special temporal shapes [5–7]. An example of molecular potential energy surfaces in two dimensions is shown in Fig. 1.2(a). Here, the ground and the excited states form a *conical intersection*. The system that has been promoted to the excited state follows the reaction pathway indicated by the black arrows and then relaxes to the ground state through a radiationless transition. It can either return to its original configuration via the pathway shown in red, or form a new configuration via the pathway indicated in blue. These transitions can occur very fast, and are responsible for important biological processes such as the stability of DNA molecules with respect to UV radiation [8]. Another example in Fig. 1.2(b) illustrates the evolution of a fluorobenzene molecule after absorption of a UV photon. Conventionally, the *reaction coordinate* is plotted that leads smoothly from the initial state to the final state and follows the path along the largest gradient of the potential [9]. Different reaction pathways are shown that represent trajectories on multi-dimensional potential energy surfaces. Along these pathways, saddle points can be encountered; the molecular configuration at this point is called a *transition state*. The investigation of such ultrafast processes in molecules is referred to as *femtochemistry*, for which the Nobel Prize in chemistry was awarded to Ahmed Zewail in 1999 “for his studies of the transition states of chemical reactions using femtosecond spectroscopy” [10].

Directly imaging the motion of single atoms in space and time is challenging and has been hardly achieved yet due to the molecular dimensions and the reaction time scales. The typical bond distance between two atoms in a molecule is on the order of 1 Ångström (10^{-10} m) and rearrangement of atoms can happen on a time scale faster than 100 femtoseconds (100×10^{-15} s). Unlike Muybridge's trotting horses, molecules have to be treated as quantum objects that are subject to the uncertainty relation, thus the position of a nucleus at a given point in time has to be described by a probability density rather than by an absolutely sharp location. Still, in certain cases, the achievable resolution is high enough to obtain information on transient structures, for example to distinguish between the two intermediate structures depicted in Fig. 1.1 [11]. An important prerequisite for a quantum concept of atomic motion that comes close to classical dynamics is the excitation of the molecule to a coherent superposition of excited states, giving rise to a wave packet that is localized within the dimension of interest [12].

In order to probe the time-dependent probability density of the nuclei, one measurement at a given instant of time is not sufficient. Instead, the same measurement has to be repeated on many identical molecules, yielding different snapshots of the probability density. This means that it is fundamentally impossible to 'see' a single quantum mechanical horse run by taking snapshot images at different points in time, but it is necessary to let the horse run multiple times, take many snapshots at a given time, and then place the camera at different positions. In this way, one probes the time-dependent evolution of the wave packet. An illustrative example where the wave function of an H_2 molecule is directly imaged by cold target recoil-ion momentum spectroscopy is given in reference [13].

The objective of this work is to investigate whether imaging of an ultrafast photochemical reaction on isolated gas-phase molecules with atomic resolution can be achieved with photoelectron diffraction. Small to medium-sized molecules with less than twenty atoms are considered here, but the goal is to develop a method that can also be extended to larger systems. Particularly interesting is the option to image a specific part of an extended target, for example the movement of a certain atom or group of atoms within a large protein. Admittedly, most of everyday chemistry happens in solution, but studying isolated molecules is a necessary first step to disentangle phenomena that are absent in the gas phase, such as anomalous fluorescence [14], from the single-molecule response.

The following section shortly describes existing methods for investigating ultrafast photochemistry and for imaging single molecules, and concludes by explaining the method of femtosecond photoelectron diffraction that is used in this work.

1.2 Experimental Approaches to Molecular Imaging

A large variety of experimental observables can yield information on processes following photoabsorption in molecules, such as ultrafast dissociation mechanisms. Such measurements do not necessarily have to be time-resolved. For example, when the lifetime of a core-excited molecular state is similar to the timescale on which dissociation starts, Doppler splitting can be observed in Auger electron spectroscopy that allows to draw conclusions about the dissociation dynamics on the timescale of a few femtoseconds, despite the use of synchrotron light pulses with picosecond duration [15]. Another example is the fragmentation of methylselenol molecules after absorption of intense X-ray pulses of femtosecond duration [16]. Here, the kinetic energy of two ionic fragments measured in coincidence allows to draw conclusions about the onset of the dissociation process that happens on a similar timescale. In some cases, the detection of end products proves that a reaction intermediate must have been present prior to the dissociation. For instance, linear acetylene molecules (HCCH) that absorb a photon in the soft X-ray regime can result in methylene (CH_2) fragments that can be detected microseconds after the actual interaction with the light pulse [17]. The mere existence of this fragment shows that one hydrogen has to have migrated from one end of the molecule to the other, temporarily forming a vinylidene (CCH_2). A similar process is found for 1-ethynyl-4-fluorobenzene molecules in this work, see chapter 4.1.

In order to systematically study such molecular dynamics, it is however preferable to trace the atomic movement on its natural time scale, rather than to deduce information indirectly from the end products. This can be achieved by first *pumping*, i. e. exciting the molecule with a light pulse, thus initiating atomic motion, and then *probing* the emerged geometry with a second pulse after a certain time delay. Two main requirements need to be fulfilled in order to resolve atomic motion:

- The time it takes to sample the molecular structure has to be short compared to the time it takes the atoms to move, otherwise different structures are probed simultaneously. The typical speed of atomic motion is 1 km/s, thus pulses as short as 10 fs are needed to resolve changes of 0.1 Å in position [12].
- The absolute timing between the initialization of the reaction and the sampling of the structure has to be known with the same precision. If this is not the case, the single photographs may be put together in the wrong order and no consistent movement can be seen.

Modern lasers making use of mode-locking schemes can readily provide pulses with durations of a few femtoseconds today, which meet the first requirement. A typical pump-probe measurement is carried out by splitting the femtosecond laser pulse into two pulses with a beam splitter, and delaying one of the pulses by increasing the path length that it has to travel to the interaction region. Both pulses are

then spatially overlapped on the target, and as they are created from the same initial pulse they are intrinsically synchronized, thus fulfilling the second criterion. Different observables can be analyzed after the probing to gain information on the ultrafast processes, some examples are given in the following.

In time-resolved *absorption spectroscopy*, the spectrum of light that is transmitted through the sample is recorded for different time delays between pump and probe pulse. Initial and final states, as well as potential intermediate geometries can have different absorption spectra, thus the delay-dependent absorption can yield information on the time scale of a reaction. *Laser-induced fluorescence* is a closely related technique that relies on the probe pulse being absorbed by an intermediate geometry, resulting in an excited state that decays via fluorescence. The energy of the emitted photon is characteristic for the created excited state.

Moreover, electrons and ionic fragments can be detected which are created if the probe pulse ionizes the molecules. In *time-resolved electron spectroscopy*, one ionizes the molecule with the probe pulse, and the energy spectrum of the emitted photoelectrons [18] or Auger electrons is recorded. Information can also be extracted from pump-probe *mass spectrometry*, as some ionic fragments may be created only from molecules that have a structure close to the equilibrium geometry or only when part of the molecule is already fragmented. However, it is usually necessary to make use of *ion-ion coincidence techniques*, from which specific fragmentation channels can be directly identified. When combined with *ion momentum imaging*, three-dimensional momenta of individual ionic fragments and electrons can be recorded by using time- and position-sensitive detectors. In this way, more detailed information can be collected, in certain cases up to kinematically complete experiments [19]. For the previously mentioned acetylene isomerization reaction, an XUV pump-probe experiment making use of ion momentum imaging revealed that the rearrangement takes place within 52 ± 15 fs [20].

The methods mentioned above provide different approaches to the detection of short-lived, intermediate states. Although information about timescales of dynamics can be obtained from these experiments, it is often difficult to extract information about the intermediate molecular structure. The aim of this work is to develop a method to *image* the time-dependent geometry as directly as possible, in the sense of recording a real-time movie that minimizes the room for interpretation. Different approaches to molecular imaging are briefly described in the following.

1.2.1 X-Ray Diffraction

In order to obtain a sharp image of an object, it is necessary to illuminate it with radiation whose wavelength is comparable to the size of the object or smaller. To resolve a typical molecular bond distance of 1 Ångström with electromagnetic radiation, a photon energy of $E = hc/\lambda = 12.4\,\text{keV}$ is thus required, corresponding to the spectral range of hard X-rays. Since their discovery in 1895 [23], X-rays have been

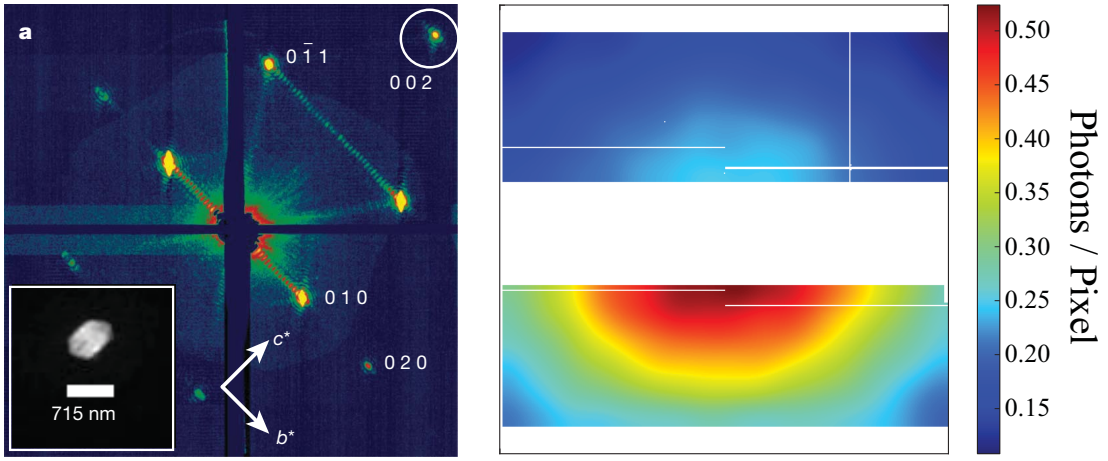

(a) (b)

Figure 1.3: X-ray diffraction images. (a) Single-shot image of a photosystem I nanocrystal irradiated by 1.8 keV photons. The figure is taken from reference [21]. (b) Integrated X-ray signal for diiodobenzonitrile ($C_7H_3I_2N$) molecules for 5×10^6 pulses of 2 keV photons. The figure is taken from reference [22].

extensively applied for studying structure. When X-rays are scattered from atoms or molecules that are arranged in a periodic crystal lattice, sharp intensity maxima, so-called *Bragg-peaks* arise at certain scattering angles that correspond to directions of constructive interference between neighboring scatterers. From the location of these peaks, the crystal structure can be derived [24]. In principle, the periodicity of the lattice is not needed for structure determination though. Every object scatters X-rays to a continuous intensity pattern that is related to the structure by Fourier transformation. However, for single, small objects these signals are very weak, thus for a long time it has only been possible to infer structures of samples that can be crystallized to large arrays.

With the advent of fourth generation light sources in the X-ray regime, the *X-ray Free-Electron Lasers* (XFELs), it has become possible to image particles that are not crystallizable or form only small crystals with the very short, very intense pulses [25] in a 'diffraction before destruction' approach [26]. Femtosecond X-ray diffraction has been implemented for large biomolecules and nano-objects with great success [21, 27–30]. Figure 1.3(a) shows an exemplary single-shot image for a photosystem I nanocrystal that is imaged with X-rays of 6.9 Å wavelength; individual Bragg peaks are clearly visible. When summing over several thousands of such patterns, after determining the crystal orientation for each individual image, the structure of photosystem I can be determined with a resolution of 8.5 Å. However, single-shot imaging of non-reproducible objects with atomic resolution, one of the major driving forces for the development of XFELs, has not been achieved yet.

For small, gas-phase molecules, X-ray diffraction suffers from the fact that elastic photon scattering contributes at most 10% to the total cross section at a pho-

ton energy of around 10 keV [31] and for light atomic constituents as typical for biomolecules, which makes it hard to achieve sufficiently good signal-to-noise ratios. Figure 1.3(b) shows the integrated diffraction signal from an aligned ensemble of diiodobenzonitrile molecules after 9 hours of data taking [22]. No clear diffraction rings are visible and most of the signal is caused by helium background. A possible way to overcome the problem of low elastic scattering cross sections is to image the molecules with electrons instead of photons.

1.2.2 Electron Diffraction

Electron beams are routinely used for determination of structure with atomic resolution, for example in transmission electron microscopes that image thin, solid samples. The de Broglie wavelength λ of an electron with a kinetic energy E_{kin} is

$$\lambda = \frac{h}{p} = \frac{h}{\sqrt{2E_{kin}m_e}} \qquad \Rightarrow \qquad \lambda[\,\text{Å}] = \frac{12.26}{\sqrt{E_{kin}[\text{eV}]}} \tag{1.1}$$

where h is the Planck constant, p is the nonrelativistic electron momentum, and m_e is the electron mass. An electron with $E_{kin} = 100\,\text{eV}$ thus has a wavelength of $\lambda = 1.2\,\text{Å}$, which is on the order of typical bond distances in molecules. An X-ray with the same wavelength has an energy of 10.3 keV, but its elastic scattering cross section on an atom is about nine orders of magnitude lower than the electron elastic scattering cross section at 100 eV [31, 32]. Electron sources with energies of around 30 keV, corresponding to $\lambda = 0.07\,\text{Å}$ are readily available today.

Electron diffraction can not only be applied to solids, but also to small, gas-phase molecules [33–36]. When an ensemble of randomly oriented molecules is imaged by a pulse of electrons, the diffracted signal shows rings of different radii, called a *powder pattern*, see Fig. 1.4(a). From these radii, all inter-atomic distances in the molecule can be reconstructed, provided that all atoms contribute to the scattering. If a pump laser triggers a photochemical process before the electron pulse arrives, it is possible to observe the changes in inter-atomic distance in the powder pattern. The difference radial distribution function $\Delta f(r)$ between the equilibrium geometry and the reaction intermediate is shown in Figs. 1.4(b) and 1.4(c). For comparison, the theoretical predictions of $\Delta f(r)$ for the two different transient structures of $C_2F_4I_2$ are shown. With this measurement, the reaction intermediate in the photodissociation could be identified as the classical structure depicted in Fig. 1.4(c) [11]. The powder pattern from randomly oriented molecules yields only information on inter-atomic distances, thus ambiguities about the structure can however occur when many similar distances exist. The time-dependent variation in the signal may in this case be superimposed with a strong, constant background. Recently it has been shown that if molecules are spatially aligned, for example by a laser field, it is possible to retrieve the full three-dimensional structure of small molecules directly from the data, with the only input being the atomic constituents [37].

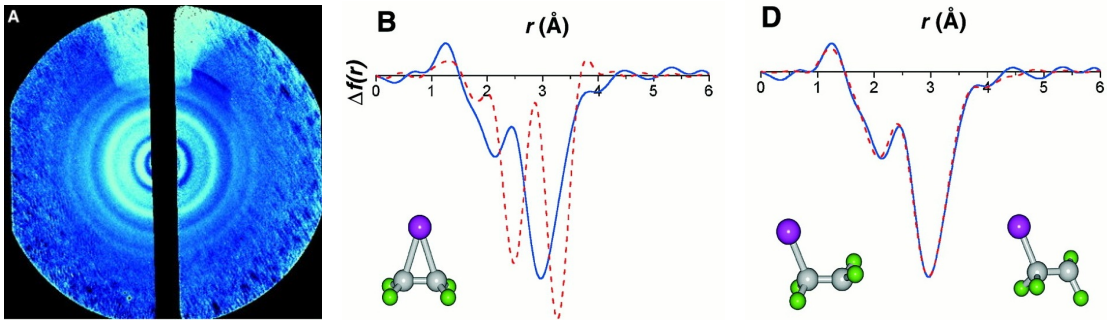

(a) (b) (c)

Figure 1.4: Electron diffraction on $C_2F_4I_2$ molecules. (a) Diffraction signal on the detector for the equilibrium geometry, recorded at an electron energy of 30 keV. (b) and (c) Difference between the radial distribution functions $f(r)$ of the equilibrium geometry and the structure after a 5 ps time delay between pump and probe pulse (blue). The comparison with calculations (red) for two different reaction intermediates is shown. All figures are taken from reference [11].

These results represent a big step forward towards the goal of single molecule movies. The major remaining issue is the achievable temporal resolution. What is called *ultrafast* electron diffraction in reference [11] refers to the picosecond time scale. However, many interesting dynamics such as isomerization reactions can happen much faster. As stated earlier, two factors limit the temporal resolution in a pump-probe experiment: the duration of pump and probe pulses and their relative synchronization. It is difficult to compress electrons to short, intense pulses because of space charge effects, but it has been demonstrated recently that pulse durations below 100 fs can be achieved for pulses of 10^6 electrons [38]. The synchronization between the arrival time of the pump laser pulse and electron pulse is uncritical when laser-driven photocathodes are used to create the electron bunches. However, in a laser-pump electron-probe experiment on gas-phase molecules, a different issue effectively limits the achievable synchronization: the laser pump-pulse travels at the speed of light, but the electrons have a finite mass and thus travel with lower velocity. This causes a *velocity mismatch* between the pump and the probe pulse for the case of an extended interaction region, meaning that the time delay between pump and probe pulse for a single shot varies throughout the sample. This has so far limited the achievable overall temporal resolution to > 850 fs [11, 34, 37]. Relativistic electron guns are developed at the moment, which operate at electron energies of a few MeV and shall achieve pulse lengths of a few ten fs [39–41]. This can improve the temporal resolution, as the electrons travel almost at speed of light, however, the elastic scattering cross section for high energies decreases by about three orders of magnitude, and electron impact ionization can become dominant, see Fig. 2.7.

An alternative approach is to create the electrons that are used for imaging directly inside of the molecule, thus avoiding the problem of velocity mismatch. Two different approaches that make use of this *imaging from the inside* are laser-induced electron diffraction and photoelectron diffraction.

1.2.3 Laser-Induced Electron Diffraction

Strong laser fields can be used to remove a valence electron from a molecule through tunneling ionization. The electron is strongly accelerated by the oscillating electric field, and depending on where in the cycle it is liberated, it either escapes from the nucleus or is driven back to the molecule. If it recombines with the nucleus, a photon is emitted. This process is called *high harmonic generation* (HHG) [42–44]; it can yield information on the initial state of the electron, the molecular valence orbital [45]. If no recombination takes place, the returning electron can scatter on the molecule, this is referred to as *laser-induced electron diffraction* (LIED). Imaging a molecule with its own recolliding electrons is an interesting option because it combines advantages of conventional electron diffraction imaging with a potentially very high spatiotemporal resolution below 1 Å and 1 fs [46, 47]. The maximum final kinetic energy of a rescattering electron is proportional to the intensity and to the square of the laser wavelength [46]. As the intensity can only be chosen moderately high in order not to destroy the molecules, high electron energies require the use of laser fields with long wavelengths in the near-infrared regime. Electron recollision energies of up to 110 eV created from a 2.3 μm laser field have been demonstrated [48].

In order to extract time-dependent information from LIED, two different approaches can be chosen [46]. In a laser-pump, LIED-probe experiment, the rescattered electron is created by a second laser pulse, in this case the temporal resolution is limited by the same factors as in a conventional pump-probe experiment. A second possibility is to use the ionization step of LIED as a pump, and the recolliding electron as a probe, which has the benefit of sub-cycle temporal resolution [48]. However, the initialization of molecular dynamics is in this case limited to wavelengths and field strengths that can be used for LIED. Delay times of more than a few femtoseconds are difficult to achieve, and for every delay a different laser wavelength is required.

For extracting a diffraction signal, monoenergetic electrons are selected from the continuous spectrum by time-of-flight or momentum imaging techniques. Even if statistics allow to select a narrow band of electrons, retrieval of molecular bond distances from the observed electron distribution is far from trivial. The returning electron wave front in LIED is treated as a plane wave over the molecular dimensions, which is a strongly idealized assumption that is reasonably valid only for small molecules, effectively limiting the method to small, non-dissociating molecules. Up to now, only diatomic molecules have been imaged with LIED [48, 49] and the applicability of the method to larger structures is questionable. Experimentally, further difficulties arise from the fact that in order to extract structural information from the scattered electrons, the molecules need to be fixed-in-space. Moreover, in the theoretical model that is used for extraction of the bond length, single scattering is assumed that is hardly applicable at electron kinetic energies of 27-38 eV as were used in reference [49]. Another principle limitation of LIED is that all molecular dynamics as well as probing of the structure happens in the presence of a strong laser field that usually strongly modifies the reaction dynamics and is hard to calculate.

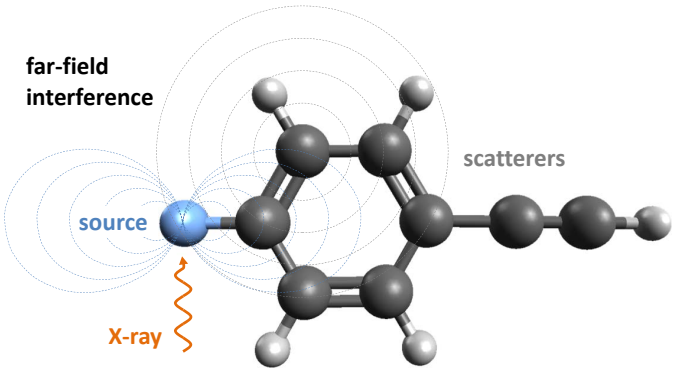

Figure 1.5: Concept of photoelectron diffraction. A photoelectron wave is created from the F(1s) core level in a C_8H_5F molecule. The direct wave can undergo intra-molecular scattering from carbon or hydrogen atoms, resulting in additional waves. In the far field, the interference between direct and scattered waves is recorded that contains information on the molecular structure.

1.2.4 Photoelectron Diffraction

A different way of creating an electron directly inside of the molecule is by inner-shell photoionization. *Photoelectron diffraction* is a well-established method for structure determination of solids and surfaces [50–52], and has also been applied to molecules adsorbed on surfaces [53, 54]. In this thesis, photoelectron diffraction is employed to study gas-phase molecules; the working principle is illustrated in Fig. 1.5. A photoelectron wave is emerging from a localized core level of a specific atom inside a molecule by X-ray absorption. The electron kinetic energy is determined by the photon energy and the electron binding energy, and the shape of the emitted wave is defined by the initial state of the electron and the X-ray polarization, see section 2.2. The outgoing wave can be scattered by other atoms within the same molecule, resulting in additional waves with their respective origin at the location of the scatterers. The resulting interference pattern between direct and scattered waves contains information on the molecular structure that has been encoded by intra-molecular scattering [55–61]. In order to be able to interpret the observed photoelectron distribution in terms of diffraction, it is crucial to create the direct photoelectron wave from a *localized orbital* of a unique atom within the molecule to assure a well-defined origin of the direct wave with respect to the molecular frame. Therefore, core levels are chosen, as valence orbitals can be de-localized, for example in benzene. In this sense, the approach presented here is complementary to recent experiments that study the time-dependent evolution of molecular valence orbitals with high-harmonic sources [62, 63]. The interference structure arises in the molecular frame, thus in order to record it in the laboratory frame, the molecules have to have a fixed orientation with respect to the detector, see also section 2.4.

The term *photoelectron holography* is also used sometimes [64, 65, 50–52]. Usually, holography is regarded as a special case of diffraction where direct and scattered wave are superimposed on the detector. In this case, it is, under certain conditions,

possible to retrieve the three-dimensional structure of the illuminated object, because the phase information is not lost [64, 66]. In X-ray and electron diffraction, the diffracted signal is usually recorded outside of the direct beam, such that no holograms are measured. For the case of photoelectron diffraction though, the direct wave emerges in the complete solid angle and is, thus, always superimposed with the scattered wave. The diffraction pattern can therefore be interpreted as a hologram [64, 65] from which the molecular structure can be directly reconstructed if higher-order scattering can be neglected [59].

Photoelectron diffraction makes use of the high elastic scattering cross sections of low-energy electrons as compared to X-rays, while at the same time avoiding the problem of velocity mismatch in conventional electron diffraction by effectively using two light beams for pumping and probing. The achievable spatial resolution is given by the kinetic energy of the photoelectron and by the degree of molecular alignment that can be obtained experimentally. The temporal resolution is determined by the durations of the pump and probe pulses and their respective synchronization. When a polyatomic molecule is irradiated with an X-ray pulse, photoelectrons are emitted from different atoms and electronic levels. The photoelectrons from a specific orbital of a specific atom of interest can, however, be easily identified by their characteristic kinetic energy. In addition, to create the majority of the photoelectrons at the desired emitter, the *element-specificity* of the photoionization process can be exploited, see section 2.1.1.

In contrast to X-ray or electron beam diffraction, where the impinging waves are described by plane waves, the amplitude of a photoelectron wave decreases as a function of radius, thus atoms close to the source always contribute stronger to the diffraction. On the one hand, this means that atoms further away from the source are difficult to image. On the other hand, this opens up the possibility of imaging only the local environment of an emitter, if an atom that serves as the source of a photoelectron wave can be introduced on purpose at the desired position in an extended molecule. For example, in a large biomolecule, only the part where a structural change takes place could be imaged.

In the following, a short introduction to the basic processes involved in photoelectron diffraction is given in chapter 2, the experimental set-up and data processing is explained in chapter 3. Experimental results on two different molecules are presented in chapters 4 and 5, followed by a critical discussion of opportunities and obstacles of using femtosecond photoelectron diffraction for imaging of ultrafast structural changes in molecules in chapter 6. A conclusion is given in chapter 7.

2 Fundamentals of Photoelectron Diffraction

In this chapter, basic physical processes involved in photoelectron diffraction are briefly discussed. First, the creation of photoelectrons from an atom or molecule is described, afterwards their angular distribution in the laboratory and in the molecular frame is investigated, and finally the principle of laser-alignment of molecules is explained.

2.1 Photoionization

For photon energies between 10 eV and 10 keV, the dominating process in the interaction between an atom and a photon is the *photoelectric effect* [31]. The photon is absorbed, and its energy is transfered to excitation or ionization of an electron. For higher photon energies, inelastic Compton scattering and pair production become important, but in this thesis only photon energies considerably lower than 10 keV are used. The term photoeffect is most often associated with the absorption of a single photon with an energy of $E_\gamma = \hbar\omega$ by an atom, resulting in the emission of an electron with a kinetic energy of

$$E_{kin} = \hbar\omega - E_b \tag{2.1}$$

where E_b is the binding energy of the electron. This process is depicted in Fig. 2.1(a). The minimum energy that is required to remove an electron from an atom in the ground state is referred to as the *ionization energy* E_i. If the photon energy is higher than E_i, the electron can be directly ionized into the continuum. If the photon energy is lower than the binding energy, it can still be possible to liberate an electron by *multi-photon ionization*, see Fig. 2.1(b), if the light intensity is high enough. The behavior of an atom or a molecule in a strong laser field depends on the intensity and the wavelength, and can be classified in accordance with the *Keldysh parameter*

$$\gamma = \sqrt{\frac{E_i}{2U_p}} \qquad \text{with} \qquad U_p = \frac{I}{4\omega^2} \tag{2.2}$$

where U_p is the *ponderomotive potential* and I is the intensity [67].

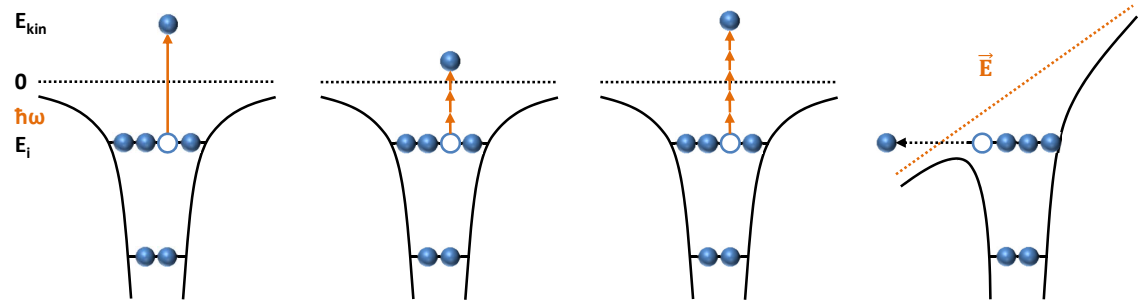

(a) single-photon ionization (b) multi-photon ionization (c) above-threshold ionization (d) strong-field ionization

Figure 2.1: Different photoionization mechanisms for an atom. Orange arrows depict energies of a single photon.

Multi-photon ionization can occur in the region $\gamma \gg 1$. For higher intensities or longer wavelengths, in the region of $\gamma > 1$, the electron can absorb more photons than needed to overcome the ionization threshold. This case is referred to as *above-threshold ionization* (ATI), and is illustrated in Fig. 2.1(c). Both, multi-photon and above-threshold ionization represent interactions of one atom with several photons simultaneously. At very high laser intensities it is no longer convenient to consider photons with discrete energies, and *strong-field ionization* is a more appropriate picture. As is illustrated in Fig. 2.1(d), for $\gamma \ll 1$ the electric field of the laser pulse is in this case strong enough to disturb the atomic potential, such that electrons can be removed by tunneling through the finite barrier, or because the barrier is decreased below the binding energy. Although this intuitive distinction in different regimes is commonly used, it should be noted that these processes are simplifications that only describe certain intensity regimes reasonably well. In a laser experiment, the data often contain different contributions due to focal averaging over different intensity regions along the beam direction and in the focal plane.

The electrons resulting from different ionization processes have different characteristics. In single-photon ionization, the kinetic energy of the electron has a discrete value that is determined by Eq. 2.1, which can be freely chosen if a source with a tunable photon energy is used. The emission direction of the electron depends on its initial state and on the photon polarization, as is described in section 2.2. In ATI, the electrons can have several discrete energy values, depending on the number of photons that are absorbed above the ionization threshold. The most probable electron energy is usually the lowest. The angular distributions of electrons created in above-threshold or strong-field ionization are in general complex, but often more electrons are emitted along the photon polarization direction, especially for higher electron energies. For the case of strong-field ionization, the final electron kinetic energy strongly depends on when in the laser cycle the electron is emitted.

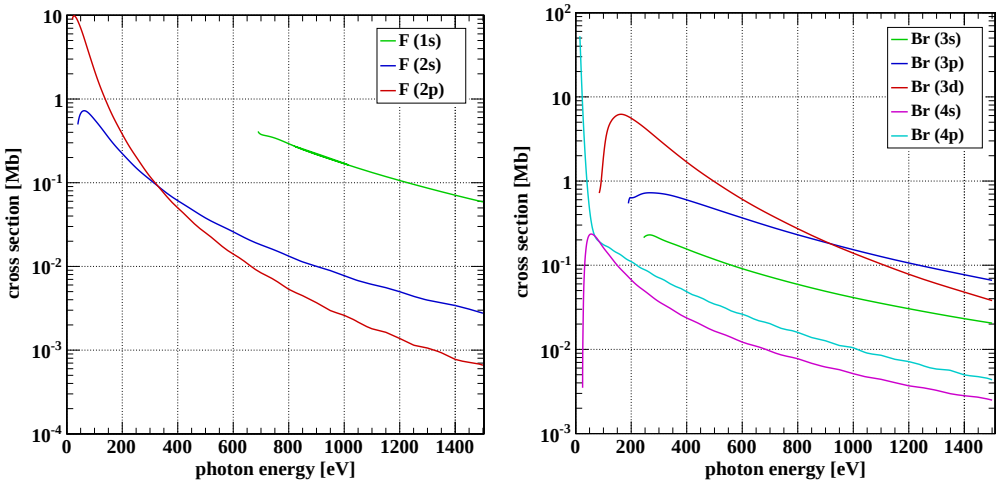

(a) fluorine (b) bromine

Figure 2.2: Partial absorption cross sections for different atomic levels as a function of photon energy. The data are taken from reference [68].

2.1.1 Photoabsorption Cross Sections

The photoabsorption cross section of an atomic species depends on its electronic structure and on the photon energy. Two general rules describe the evolution of the total absorption cross section σ_{tot} and the partial ionization cross section σ_{nl} [69]:

- The total absorption cross section is larger for heavier atoms, it rises approximately as $\sigma_{tot} \sim Z^5$ where Z is the atomic number.
- For a given electronic level (nl), the partial ionization cross section is highest for photon energies just above the ionization threshold, for high energies it decreases as $\sigma_{nl} \sim 1/E_\gamma^{7/2}$.

The combination of both statements implies that for sufficiently high photon energies, the heaviest atom in a molecule is usually most likely to absorb a photon. Photoabsorption cross sections of different atomic species can be very different at a given photon energy, thus the energy can sometimes be chosen such that almost exclusively one atomic species in the molecule absorbs the photon. This is referred to as the *element specificity* of photoabsorption. Figure 2.2(a) shows the partial absorption cross sections for all levels of atomic fluorine. The decrease for higher energies is clearly visible. The second statement suggests that for a given electronic configuration and a given photon energy, the photon is most likely to be absorbed by lowest-lying orbital (nl) that it can ionize. However, although the absorption probability for each electron decreases for higher angular momentum, the s-subshells are populated with only two electrons, whereas p- and d-shells contain up to six and ten electrons, respectively. Therefore, the total absorption cross section can be higher for higher-lying orbitals. This is shown for the example of bromine in Fig. 2.2(b). σ_3 is larger than σ_4 but σ_{3s} is smaller than σ_{3p} and σ_{3d}.

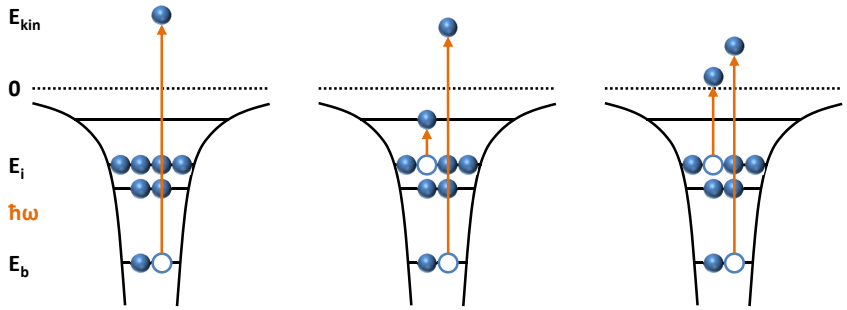

(a) direct ionization (b) shake-up (c) shake-off

Figure 2.3: Direct inner-shell photoionization and second-order processes that decrease the energy of the photoelectron.

2.1.2 Second-Order Processes in Photoionization

If an inner-shell electron is removed from an atom, as depicted in Fig. 2.3(a), its kinetic energy is given by Eq. 2.1. The corresponding spectral line has a certain width, ΔE, which depends on the lifetime of the core-ionized state Δt according to the uncertainty relation

$$\Delta E\,\Delta t \geq \frac{\hbar}{2} \qquad \Rightarrow \qquad \Delta E\,[\mathrm{eV}] \geq \frac{0.66}{\Delta t\,[\mathrm{fs}]} \tag{2.3}$$

Typical values for the $1s$ linewidth for $6 \geq Z \geq 10$ are 0.1 -0.25 eV [70], corresponding to lifetimes of 3 -7 fs. However, the fact that an atom is a multi-electron system can influence the photoelectron energy, when inelastic second-order interactions of the photoelectron with other electrons of the same atom occur. In a *shake-up* process, as depicted in Fig. 2.3(b), a valence electron is excited to an unoccupied orbital, such that the photoelectron loses a discrete amount of energy. The corresponding sub-structure lines of the photoelectron spectrum are called *satellites*. For a photon energy of $E_\gamma \geq E_b + E_i$, a *shake-off* can occur, see Fig. 2.3(c), where the valence electron is ionized and, thus, two electrons are emitted. Here, the energy of the photoelectron is no longer discrete, as the energy sharing of the two electrons results in a continuous spectrum.

After the photoelectron has left the atom, a core-ionized ion results. This is an instable state which usually decays by filling the core hole with an electron from a higher orbital. Two main mechanisms exist to liberate the additional energy: in *fluorescence*, a photon is emitted whose energy corresponds to the difference in binding energies between the two involved levels, see Fig. 2.4(a). On the other hand, the energy can be transferred to another electron via Coulomb interaction that is ionized to the continuum. This non-radiative decay process is called *Auger decay*, see Fig. 2.4(b). One decay results in a doubly charged ion, but in heavy atoms or molecules, decay cascades can occur, resulting in multiply charged ions.

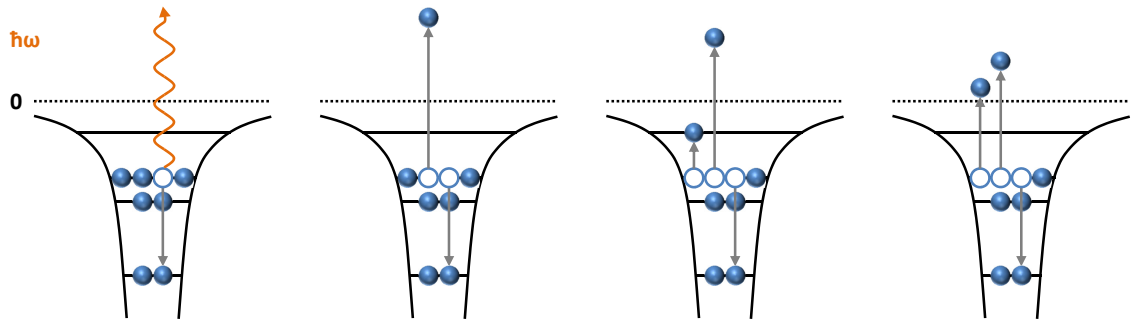

(a) fluorescence (b) Auger decay (c) Auger + shake-up (d) Auger + shake-off

Figure 2.4: Decay processes for a core-ionized atom. In (a) a photon is emitted, whereas (b) to (d) depict multi-electron processes.

The relative probability for fluorescence and Auger decay depends on the atomic number. For atoms with atomic numbers $Z \leq 10$ the probability for fluorescence is $\leq 5\%$ [31] and Auger decay is the dominant process when energetically possible. Additional interactions with the valence electrons can occur during the Auger decay. Figures 2.4(c) and 2.4(d) illustrate combined Auger decay and shake processes. If the atom is bound in a molecule or a cluster, inter-atomic effects can occur in addition [71–73].

2.1.3 Molecular Photoionization

If an atom is not free, but bound in a molecule, the electronic structure of the atom is modified by the neighboring atoms. The electrons move in the electric field of all nuclei and all electrons, thus the resulting potential is no longer spherical. Molecular orbitals can be constructed from a linear combination of the atomic orbitals (LCAO) [74] that may result in very different shapes as compared to the orbitals of the individual atoms. Valence orbitals can become delocalized over several atoms, or even the complete molecule, such that electrons can move almost freely between atoms.

The core levels of an atom that is bound in a molecule, however, remain localized at the atomic site. Thus, they can often, to good approximation, be described by atomic orbitals, except for a shift in the binding energy. This is referred to as the *chemical shift* in photoelectron spectroscopy. The molecular energy levels depend on the internuclear distance, thus potential energy curves arise. If a potential curve has a minimum, the state is stable and the molecule remains bound, which is always the case for the ground state of a molecule. If the molecule is electronically excited, for example by photoabsorption, the system is promoted to a higher potential energy curve that may not have a minimum. This is called a *dissociative state* which causes fragmentation of the molecule into two or more parts.

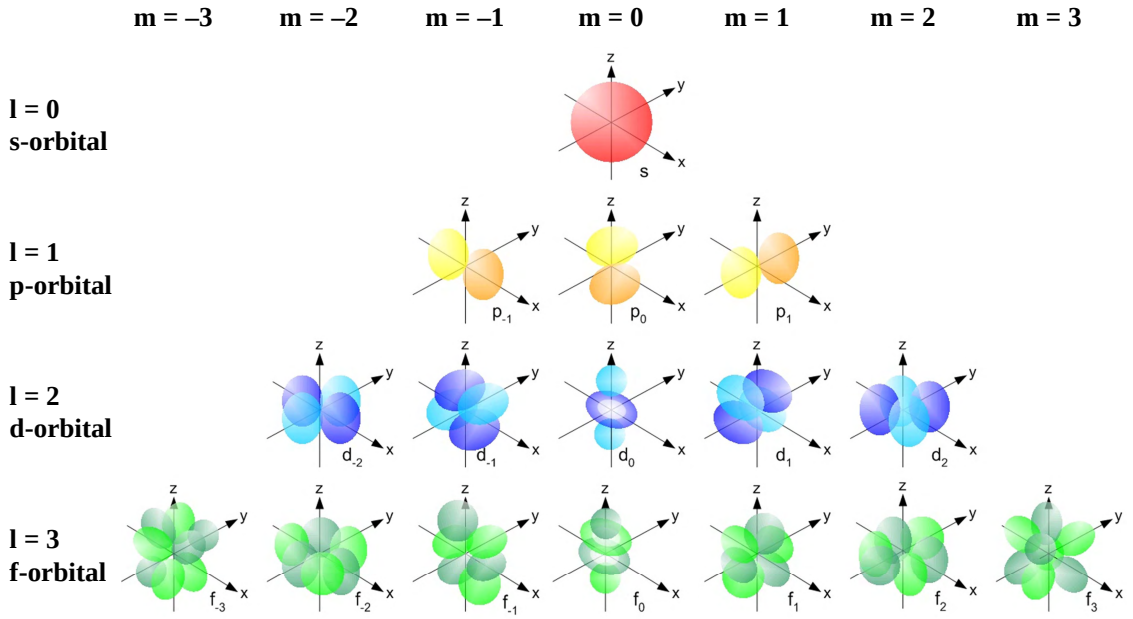

Figure 2.5: Atomic orbitals for different values of the quantum numbers (l, m). The figure is taken from reference [75].

2.2 Laboratory-Frame Photoelectron Angular Distributions

For single-photon ionization of an atomic orbital, the resulting *photoelectron angular distribution* (PAD) is determined by the initial state of the photoelectron and by the light polarization. Atomic orbitals are characterized by quantum numbers (n, l, m) where n is the principal quantum number, $l \leq n-1$ is the angular momentum quantum number, and the magnetic quantum number m is the projection of l. The probability of finding an electron at a position (θ, ϕ) in a spherically symmetric potential, where θ and ϕ are the azimuthal and the polar angle respectively, can be described by the square of spherical harmonics $|Y_l^m(\theta,\phi)|^2$ [76]. These are defined by

$$Y_l^m(\theta,\phi) = \sqrt{\frac{(2l+1)}{4\pi}\frac{(l-m)!}{(l+m)!}} P_l^m(\cos\theta) e^{im\phi}, \tag{2.4}$$

where P_l^m are the associated Legendre polynomials [77]. Figure 2.5 shows the atomic orbitals for $l \leq 3$ and all possible projections m. Partial photoelectron waves that are created in photoionization can be characterized by the same angular shapes, and are referred to as *s*-, *p*-, *d*-, and *f*-waves, respectively. The photon transfers its angular momentum $l_\gamma = 1$ to the electron, thus the final photoelectron angular momentum is $l_f = l \pm 1$ where l is the angular momentum of the initial state. For linearly polarized light, $m_\gamma = 0$, thus $m_f = m$. For circularly polarized light, $m_\gamma = \pm 1$, thus $m_f = m \pm 1$.

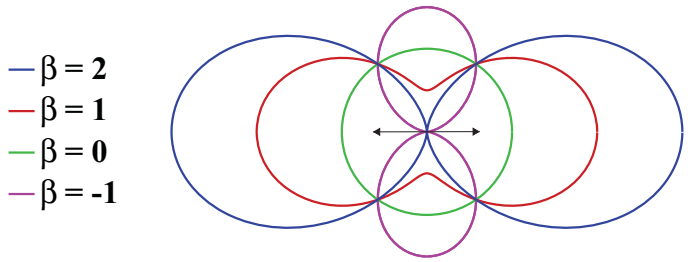

Figure 2.6: Differential photoionization cross sections with different values of the asymmetry parameter β. The distributions are cylindrically symmetric around the light polarization direction that is indicated by the arrow.

For the ionization of an s-orbital with linearly polarized light, only $l_f = 1$, $m = 0$ can result, and the emitted electron wave can be described by a pure p_0-wave, see Fig. 2.5. For all other initial states with $l \neq 0$, a superposition of different waves is created. For example, ionization of a p-orbital by linearly polarized light results in a superposition of s-, d_0-, d_{-1}-, and d_1-waves. However, *Cooper minima* can arise for ionization of orbitals with $l < n - 1$, if the contribution of one partial wave vanishes for a certain photon energy [78]. The photoelectron angular distribution arising from the single-photon ionization of an atom by linearly polarized light is a superposition of all allowed partial waves and can be described by

$$\frac{d\sigma}{d\Omega} = \frac{\sigma_{tot}}{4\pi}[1 + \beta P_2(\cos\theta)] \qquad \text{with} \qquad P_2(\cos\theta) = \frac{3}{2}\cos^2\theta - \frac{1}{2}, \tag{2.5}$$

where $d\sigma/d\Omega$ is the differential cross section, $P_2 = P_2^0$ is the Legendre polynomial for $l = 2$, β is the *asymmetry parameter*, and θ is the angle between the symmetry axis, here the light polarization, and the electron emission direction [79]. From Eq. 2.5 it follows that $-1 \leq \beta \leq 2$, as $d\sigma/d\Omega \geq 0$. Figure 2.6 shows differential cross sections with different asymmetries. $\beta = 0$ corresponds to an s-wave, $\beta = 2$ to a p-wave. For circularly polarized light, the PAD can be expressed by Eq. 2.5 as well, when replacing β by

$$\beta_{\text{circ}} = -\frac{1}{2}\beta \tag{2.6}$$

for both left and right circularly polarized light [80, 81]. θ is measured with respect to the symmetry axis which is the photon propagation direction for the case of circular light. The asymmetry parameter can be expressed explicitly as a function of the electron initial state l, of the partial ionization cross sections σ_{l+1} and σ_{l-1} and of the phase shift between the partial waves δ_{l+1} and δ_{l-1} [79]. This phase shift, and thus the asymmetry parameter for the ionization of a certain atomic orbital, is a function of the photon energy [78]. For example, for the ionization of rare gases, $\beta(E)$ converges to 1.5 for ionization of p-orbitals and to 1.0 for ionization of d-orbitals in the high-energy limit [82], but can vary strongly for lower energies.

If an atom is bound in a molecule, the photoelectron angular distribution is modified by the surrounding atoms, see the next section. However, it was shown that for single-photon ionization of a randomly oriented ensemble of molecules, the laboratory-frame PAD can be described by Eq. 2.5 [83], but the asymmetry parameter β in a molecule is different from the value for a free atom. For molecular photoionization, the angular momentum l is not a conserved quantum number, therefore the outgoing electron wave that was restricted to $l_f = l \pm 1$ in the atomic case can here contain contributions with higher angular momentum. This may also be explained by scattering of the photoelectron on other atoms within the same molecule, from which additional angular momentum can be gained [55]. The scattering changes as a function of electron energy, see also the next section, thus the asymmetry parameter $\beta(E)$ varies as a function of electron energy.

The distribution $\beta(E)$ is characteristic for a molecule, for example, close to the ionization threshold the asymmetry parameter is influenced by shape resonances. A semiempirical relationship between the position of the shape resonance and the bond lengths has been discussed [84]. Studying photoelectron angular distributions in the laboratory frame can sometimes even provide information on dynamics of molecular structure when complemented with calculations [78, 85], for example on nonradiative transitions [86, 87]. However, the information content of $\beta(E)$ alone is limited, and detailed structural information cannot be obtained.

2.3 Molecular-Frame Photoelectron Angular Distributions

When changing the perspective from the laboratory frame to the molecular frame, it becomes clear that the asymmetry in the laboratory-frame PAD can be ascribed to rotational averaging of a much more structured angular distribution that arises in the frame of the molecule. The *molecular-frame photoelectron angular distribution* (MFPAD) can be described by

$$\frac{d\sigma}{d\Omega} = \sum_{l=0}^{2l_{max}} \sum_{m} A_l^m Y_l^m, \tag{2.7}$$

where l_{max} is the largest orbital momentum component of the photoelectron amplitude [83]. In principle, $l_{max} = \infty$, but practically the expansion can often be terminated after the first few terms. In contrast to the PAD in the laboratory frame that is given by Eq. 2.5, even and odd harmonics contribute to the MFPAD. Odd terms arise from interference of photoelectron partial waves of opposite parity and occur only when the initial or the final state do not have well-defined parity [83]. No odd terms contribute to the MFPAD when the molecules are only *aligned* but not *oriented* in space, see also Fig. 2.10. For single-photon ionization of cylindri-

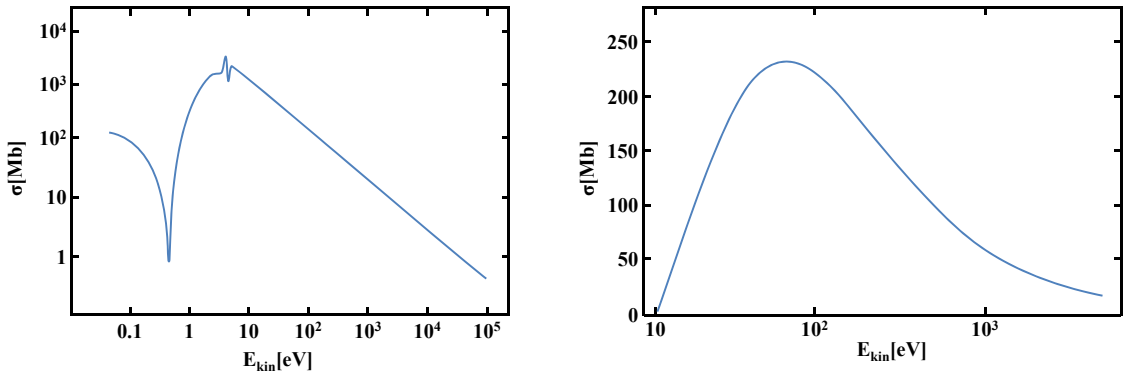

(a) elastic electron scattering on a nucleus (b) electron impact ionization of a carbon atom

Figure 2.7: Electron scattering cross sections as a function of the kinetic energy of the electron. The data in (a) are taken from reference [88], the data in (b) are taken from reference [89].

cally symmetric molecules with their axes parallel to the linear photon polarization direction, Eq. 2.7 simplifies to

$$\frac{d\sigma}{d\Omega} = \sum_{l=0}^{2l_{max}} A_l P_l(\cos\theta). \tag{2.8}$$

The laboratory-frame PAD converges to the MFPAD for molecules that are perfectly fixed in space. To establish the connection of the MFPAD to the molecular structure, the experimentally obtained photoelectron angular distributions of fixed-in-space molecules are compared to calculated MFPADs. In the following, different approaches to calculate MFPADs are introduced. First, general characteristics of MFPADs are described in a very simple model for the example of a diatomic molecule, afterwards single scattering and density functional theory calculations are presented.

2.3.1 A Simple Man's Approach

The generally complex shape of a molecular-frame photoelectron angular distribution is difficult to understand intuitively. In this section, an attempt is made to illustrate basic features of MFPADs by assuming that they arise from single scattering of the photoelectron on other atoms within the same molecule. The cross sections for elastic scattering of an electron on a nucleus, σ_{el}, and for electron-impact ionization of a carbon atom, σ_{imp}, are shown in Fig. 2.7. σ_{el} has a maximum of about 2000 Mb between 5 and 10 eV electron kinetic energy, the maximum of σ_{imp} of about 230 Mb lies between 50 and 100 eV. For high energies, the cross sections evolve as

$$\sigma_{\mathrm{el}} \sim \frac{1}{E}, \quad \sigma_{\mathrm{imp}} \sim \frac{\ln(E)}{E} \quad \Rightarrow \quad \frac{\sigma_{\mathrm{el}}}{\sigma_{\mathrm{imp}}} \sim \frac{1}{\ln(E)}. \tag{2.9}$$

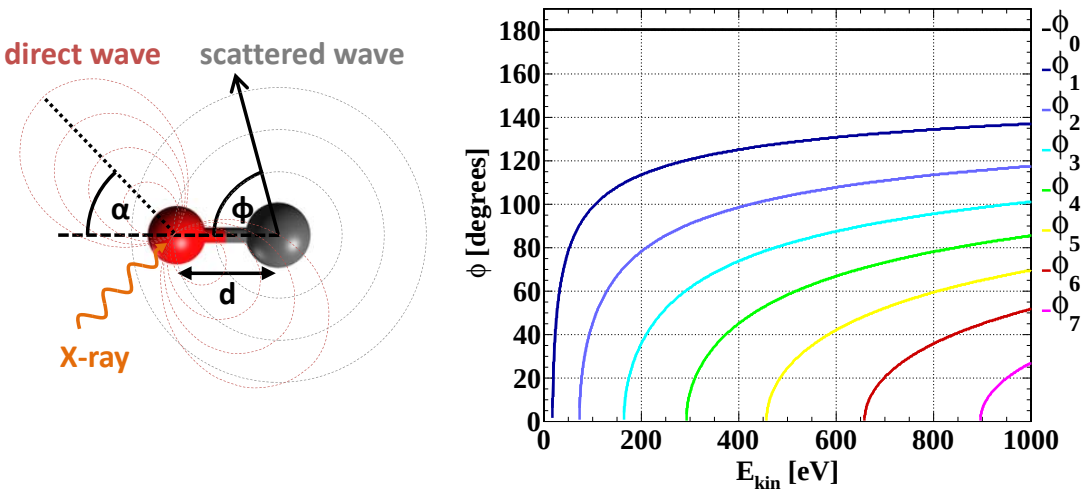

(a) (b)

Figure 2.8: (a) Principle of photoelectron diffraction for 1s ionization of an oxygen atom in a CO molecule by a linearly polarized X-ray photon. (b) Angular positions of interference maxima ϕ_n as a function of photoelectron kinetic energy calculated for CO with a bond distance of $d = 1.43$ Å. ϕ is the scattering angle as defined in (a).

Above ~ 10 eV, the ratio between elastically and inelastically scattered electrons is thus higher for lower electron energies.[1] In impact ionization, the photoelectron loses at least as much energy as is required to ionize the atom it scatters on ($E_i = 11$ eV for a carbon atom [91]). The two resulting electrons can share the available kinetic energy variably, the most probable case however is that the incident electron loses only the ionization energy and the second electron is emitted with almost no kinetic energy [92]. This implies that the direction of the incident electron is usually not altered significantly, as a large change in angle corresponds to a large momentum transfer.

For illustrative purposes, inelastic scattering is neglected in this model and elastic scattering of the electrons on point-like nuclei is assumed. No scattering phase shifts and no angle- or energy-dependent scattering cross sections are taken into account. The most simple test case is the single-photon ionization of a diatomic molecule by a linearly polarized photon, see Fig. 2.8(a). For inner-shell ionization, the location of one nucleus can be regarded as the origin of the photoelectron wave and only one scatterer exists. Part of the direct wave can be scattered on the neighboring atom, resulting in a second, spherical wave originating from this nucleus. Constructive interference between direct and scattered wave arises for scattering angles ϕ_n, for

[1] Scattering of an electron on a carbon atom: [32, 90]
$E = 50$ eV: $\sigma_{\mathrm{el}} = 469$ Mb, $\sigma_{\mathrm{imp}} = 224$ Mb
$E = 100$ eV: $\sigma_{\mathrm{el}} = 294$ Mb, $\sigma_{\mathrm{imp}} = 221$ Mb
$E = 1000$ eV: $\sigma_{\mathrm{el}} = 54$ Mb, $\sigma_{\mathrm{imp}} = 60$ Mb

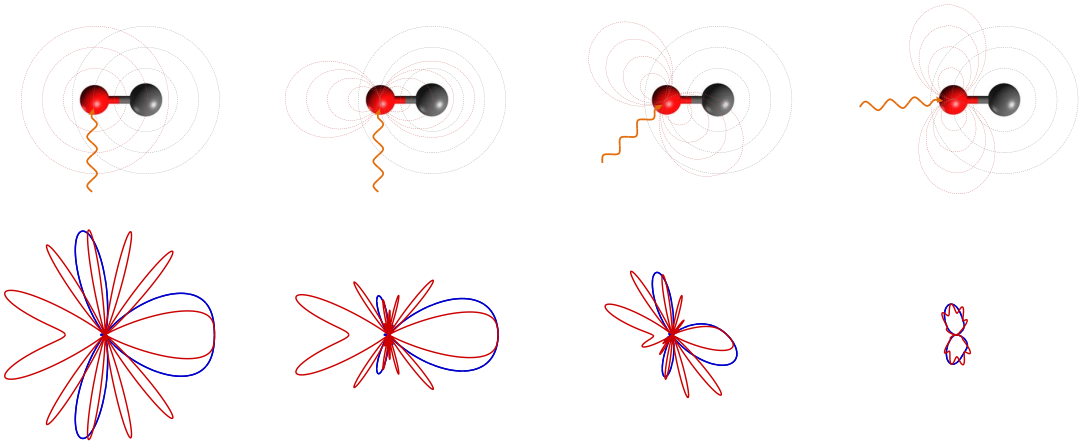

(a) s-wave (b) p-wave, $\alpha = 0°$ (c) p-wave, $\alpha = 45°$ (d) p-wave, $\alpha = 85°$

Figure 2.9: MFPADs calculated for a CO molecule for different orientations of the photon polarization with respect to the molecular axis. Blue: photoelectrons with 50 eV kinetic energy. Red: photoelectrons with 500 eV kinetic energy. The distributions are calculated for $A = B = 1$.

which the path length difference $d + d\cos\phi$ equals a multiple n of the electron wavelength λ that is given by Eq. 1.1.

$$d + d\cos\phi = n\lambda \qquad \Rightarrow \qquad \phi_n = \arccos\left(\frac{n}{d}\frac{12.26}{\sqrt{E_{kin}[\mathrm{eV}]}} - 1\right) \tag{2.10}$$

The angular positions of the interference maxima ϕ_n thus depend on the kinetic energy of the electron, as is shown in Fig. 2.8(b). The individual maxima shift to larger scattering angles for higher energies, and more interference maxima arise with every multiple of the wavelength. This means that, in general, the electron angular distribution is more structured for higher electron kinetic energies. The intensity $I(\phi)$ as a function of the scattering angle can be calculated from the interference between direct and scattered wave. If an s-wave with amplitude A is assumed as a source, the final intensity distribution is given by

$$I(\phi) = [A + B\,\cos\,\eta(\phi)]^2 \qquad \text{with} \qquad \eta(\phi) = \frac{2\pi d}{\lambda}(1 + \cos\phi), \tag{2.11}$$

where B is the amplitude of the scattered wave and $\eta(\phi)$ is the phase difference between direct and scattered wave. The resulting MFPADs for electrons of 50 and 500 eV kinetic energy are shown in Fig. 2.9(a). The positions of maximum interference as expected from Fig. 2.8(b) can be identified. For the case of 1s-ionization, a p-wave results, see section 2.2. This can be taken into account by introducing two additional factors in Eq. 2.11

$$I(\phi) = [A\,|\cos(\phi + \alpha)| + B\,\cos\,\eta(\phi)\,|\cos(\alpha)|]^2\,. \tag{2.12}$$

The term $|\cos(\phi + \alpha)|$ describes the angle-dependent amplitude of the direct p-wave, and $|\cos(\alpha)|$ decreases the amplitude of the spherical scattered wave accordingly. α is the angle between the molecular axis and the light polarization vector as indicated in Fig. 2.8(a). The resulting angular distribution for linear polarization parallel to the molecular axis is shown in Fig. 2.9(b), it is significantly altered as compared to the MFPAD in Fig. 2.9(a). The intensities of maxima close to $\phi = 90/270°$ are reduced, and additional maxima arise at positions where destructive interference completely cancels the intensity for the case of an s-wave. For a non-spherical initial wave, the MFPAD depends on the angle α between the molecular axis and the light polarization, two examples for $\alpha = 45°$ and $\alpha = 85°$ are shown in Figs. 2.9(c) and 2.9(d). When the polarization is perpendicular to the molecular axis, a pure p-wave results, as no intensity is emitted in the direction of the point-like scatterer. For a more detailed discussion refer to section 6.1.2.

2.3.2 Scattering in the First Born Approximation

The simple calculations in the previous paragraph cannot be expected to reproduce experimental results correctly, as atoms are treated as point-like particles and not as potentials. To obtain a more realistic result, the scattering model by Krasniqi *et al.* is considered [59]. The starting point is a pure p-wave of photoelectrons, resulting from ionization of an atomic s-orbital. All other atoms in the molecule are treated as Yukawa potentials $V(r)$ with an effective range $a \cong a_0/Z^{1/3}$ that is estimated based on the Thomas-Fermi model. a_0 is the Bohr radius and Z is the atomic number. The intra-molecular elastic scattering of the photoelectron is described by a sum over individual scattering amplitudes $f(\phi)$, where $|f(\phi)|^2 = d\sigma/d\Omega(E, \phi)$ is the energy- and element-dependent differential scattering cross section.

The scattering amplitudes are calculated in the first Born approximation, which holds for the case that the amplitude of the scattered wave is much smaller than the amplitude of the incident wave, corresponding to weak scattering. The criterion for the validity of the Born approximation can be expressed as $|V_0|a/\hbar v_e \ll 1$, where $|V_0|$ is the strength of the potential and v_e is the velocity of the electron [93]. The final electron spatial distribution recorded on a two-dimensional detector is given by the square of the wave function. As the scattering amplitude is the Fourier transform of the potential on which the electron scatters, the recorded image is a hologram in the sense of Gabor [66]. Fourier transform of the hologram yields real space images of the scatterers, that correspond to the positions of the nuclei.

In this model, it is assumed that the scattering potential has an effective range much smaller than the distance between the source and the scatterer. This is only valid if the electron scatters predominantly on a potential that is localized at the atomic cores and not on delocalized valence orbitals. For lower electron energies, this may however not be an appropriate description. Roughly speaking, an electron of lower energy penetrates less deep into the potential before scattering on it, and thus is

more sensitive to the shape of the potential at larger distances from the nuclei. Therefore, the actual molecular potential needs to be taken into account for the scattering at lower energies that can be very different from the sum of independent Yukawa potentials. Comparison with results of density functional theory calculations suggests that scattering within the first Born approximation may already be a valid description for electrons of a few hundred eV kinetic energy, see section 6.1.3.

2.3.3 Density Functional Theory

An alternative approach to obtain molecular-frame photoelectron angular distributions that is suitable for low electron energies is the calculation of bound-state and continuum electron wave functions within the framework of *density functional theory* (DFT). Details of the method that was used by P. Decleva and M. Stener to calculate the partial photoionization cross sections and the MFPADs that are compared to the experimental data in this work are described in references [94–96].

In principle, the exact solution of the electron wave function has to be obtained from solving the multi-particle Schrödinger equation. The movement of one electron within a multi-electron system of interacting particles can be approximated by the movement in an effective potential that results in the same electron density. In DFT, the *Kohn-Sham* approach derives the density from the solution of a single-particle hamiltonian, h_{KS}, that is itself a functional of the ground state electron density ρ.

$$h_{\mathrm{KS}}\varphi_i = E_i\varphi_i \tag{2.13}$$

$$h_{\mathrm{KS}} = -1/2\nabla^2 + V_{\mathrm{N}} + V_{\mathrm{C}}(\rho) + V_{\mathrm{XC}}(\rho) \tag{2.14}$$

Here V_{N} is the attractive potential of the nuclei, $V_{\mathrm{C}}(\rho)$ is the repulsive Coulomb potential of the electrons, and $V_{\mathrm{XC}}(\rho)$ is the exchange correlation potential. In this work, the LB-94 potential [97] has been used for V_{XC} which takes into account the correct Coulombic behavior of the potential at large distances from the molecule. Many different basis sets can be chosen for a numerical solution of these equations. The expansion of the molecular orbitals is performed in an LCAO multicenter approach that is suitable for deep core holes [95]. The radial part of the total wave function is described by B-splines [94] and the angular part is given by spherical harmonics that are adapted to the molecular symmetry. B stands for *basis* here, and a *spline* is a polynomial function that is defined piecewise and allows to draw a smooth curve through individual points. Spline basis functions are thus defined only for a limited range. Within that range, a sequence of knot points is defined through which a smooth curve is to be found.

This approach requires to confine the problem to a sphere of a given maximum radius. This sphere in general needs to be chosen much larger than the object of interest. For example, to calculate the energy of the hydrogen ($1s$) level correctly that has a radius of 0.8 Å, the cut-off radius has to be chosen larger than 16 Å in order to obtain the proper energy [94]. For the description of a photoionization process, not

only the initial bound state but also the final continuum state of the photoelectron needs to be calculated. To achieve a reasonable accuracy for these states is one of the major issues in the theoretical description of photoionization. The use of B-spline basis functions allows to implement the boundary conditions for unbound continuum states, which cannot be obeyed when conventional basis functions are employed. Although B-splines are computationally more demanding than conventional basis sets, it is possible to extend the formalism to a time-dependent description (TDDFT) that is required for the calculation of molecular dynamics.

Up to now, MFPADs have mostly been calculated for molecules with only a few atoms and for electron energies of $\leq 100\,\mathrm{eV}$. The molecules used in this work are among the largest ones that have, so far, been treated in this formalism, but it is shown that MFPADs can be calculated for electron energies up to 500 eV, facilitating a comparison with the results obtained within the first Born approximation, see section 6.1.3. Computational limits of the DFT approach could arise when MFPADs for energies high above the ionization threshold are calculated for large molecules, as for higher electron energies, more angular momenta need to be included in the continuum wave function.

Alternative approaches to describe the molecular states in the continuum include a description of the orbital as spherical, non-overlapping atomic potentials [98], as overlapping spherical potentials (CMS-Xα) [99], as muffin-tin potentials (EDAC) [100, 101] or as full non-spherical potentials [102]. CMS-Xα is usually applied to electron energies $< 30\,\mathrm{eV}$, whereas EDAC is appropriate for energies $> 50\,\mathrm{eV}$. Both methods approximate the molecular potential rather crudely. The use of non-spherical potentials is probably the best description of the real molecular potential within multiple scattering theories, but is currently only applicable to diatomic molecules.

2.4 Alignment of Molecules with Strong Laser Pulses

Recording a molecular-frame photoelectron angular distribution in the laboratory frame requires fixing the molecular frame with respect to the laboratory frame. Different categories of fixing a molecule in space can be distinguished, as is illustrated in Fig. 2.10. Naturally, an ensemble of gas-phase molecules is randomly oriented. In *one-dimensional alignment*, one axis of the molecule is fixed in space, while the molecule can still freely rotate about that axis. *Three-dimensional alignment* is achieved if in addition a second axis of the molecule is fixed. If not only the direction of the axes but also the head-tail orientation of the molecule is defined, *one-* or *three-dimensional orientation* is realized.

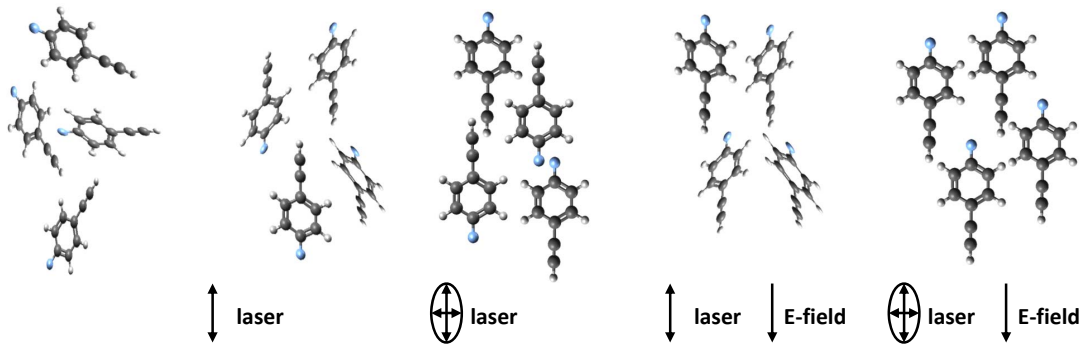

(a) random (b) 1d-alignment (c) 3d-alignment (d) 1d-orientation (e) 3d-orientation

Figure 2.10: Different types of molecular alignment, illustrated for the example of C_8H_5F molecules. Polarization directions of an alignment laser and a static electric field are indicated. The most polarizable axis of the molecule lies along the F-C bond, the second most polarizable axis is perpendicular to that, parallel to the plane of the benzene ring. See text for details.

Experimentally, one possibility to fix molecules in space is to determine the orientation of the molecule *after* the photoionization by recording the momentum vector of one or more characteristic ionic fragments in coincidence with the photoelectron [55, 56, 58, 103–105], see also section 4.1. The molecules are automatically oriented if only one possibility exists to create the recorded fragment from the molecule. Under certain conditions, a high degree of one-dimensional orientation can be achieved with this technique, see section 6.2.2. Achieving three-dimensional orientation is more complicated as two-fold ion-ion coincidences are required.

Another option to fix the molecular frame with respect to the laboratory frame is by actively aligning the molecules in space *before* the photoionization using strong laser pulses. The underlying principles of *adiabatic laser-alignment* are briefly described in the following[2], and a short introduction to nonadiabatic alignment is given. For a discussion about which method is better suited for imaging structural changes in polyatomic molecules with photoelectron diffraction, refer to section 6.2.

2.4.1 One-Dimensional Laser-Alignment

The electric field ϵ of a linearly polarized, continuous-wave laser is described by

$$\epsilon = \epsilon_0 \cos(\omega t) \tag{2.15}$$

where ϵ_0 is the amplitude and ω is the frequency. The linear polarization direction defines a fixed axis with respect to the laboratory frame. When a linear, or a symmetric top molecule is exposed to this field, two potentials $V_\mu(\theta)$ and $V_\alpha(\theta)$

[2] This part is based on [106–109].

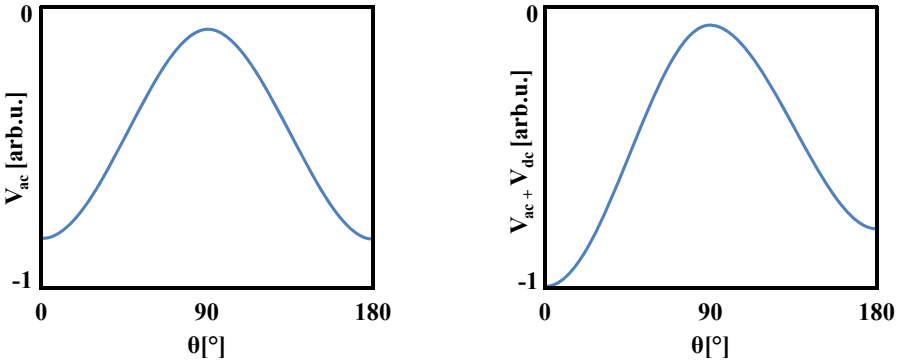

(a) one-dimensional alignment (b) one-dimensional orientation

Figure 2.11: Potentials for alignment and orientation of molecules by a strong ac laser field and a weak dc electric field.

act on the molecule that depend on the angle θ between the polarization and the molecular axis.

$$V_\mu(\theta) = -\mu\epsilon\cos\theta \tag{2.16}$$

$$V_\alpha(\theta) = -\frac{1}{2}\epsilon^2(\alpha_\parallel\cos^2\theta + \alpha_\perp\sin^2\theta) \tag{2.17}$$

Here μ is the permanent dipole moment along the molecular axis, $\alpha_\parallel$ is the polarizability of the molecule parallel to that axis and $\alpha_\perp$ is the polarizability perpendicular to that axis [106]. For a finite pulse duration T and for nonresonant frequencies $\omega \gg 1/T$, the pulse has many cycles and a temporal average over Eq. 2.16 results in $\langle\cos(\omega t)\rangle = 1/2$. This reduces Eqs. 2.16 and 2.17 to an effective potential of

$$V_{ac}(\theta) = V_\alpha = -\frac{1}{4}\epsilon_0^2\ \left[(\alpha_\parallel - \alpha_\perp)\cos^2\theta + \alpha_\perp\right] \tag{2.18}$$

that depends only on the polarizability of the molecule. Alignment in one dimension can thus be realized for all molecules that have an anisotropic polarizability. $V_{ac} \sim -\cos^2\theta$ has the shape of a double well with minima at $\theta = 0°$ and $\theta = 180°$ for $\alpha_\parallel > \alpha_\perp$, as is illustrated in Fig. 2.11(a). If the field is strong enough, $V_{ac}(\theta)$ thus confines the molecular axes along the field direction in the potential minima. Quantum-mechanically, this situation can be described by pendular states [106]. If the pulse duration is long compared to the rotational period of the molecule, the confinement happens adiabatically. The maximum alignment is achieved in the peak of the intensity, upon turn-off the molecules return to their initial random orientation.

The degree of alignment for an ensemble of molecules is given by the angular distribution of the molecular axes $\rho(\theta)$ with respect to the space-fixed axis. Experimentally, this can be evaluated by photodissociating the molecules, see also sections 3.1.5, 4.2 and 5.1. In principle, the distribution $\rho(\theta)$ needs to be described by an expansion in

even Legendre polynomials, however, in the high-field limit it can to a good degree be approximated by a Gaussian [106]. The maximum degree of alignment that can be achieved depends on the strength of the electric field and on the rotational temperature of the molecular ensemble. It increases for increasing field strengths and for lower rotational temperatures. Moreover, the ideal characteristics of the alignment pulse are different for different molecules. In general, for equal pulse energies, heavier molecules require longer pulses with lower intensity, whereas lighter molecules need shorter pulses with higher intensity [107]. Molecules with a higher polarizability need less intensity to align. The maximum intensity that can be applied to the target is limited by the onset of nonresonant ionization, see section 2.1.

2.4.2 One-Dimensional Mixed-Field Orientation

A purely alternating (ac) electric field that was described in the previous paragraph can only align molecules in space, as the potential in Fig. 2.11(a) is symmetric around 90°. A static (dc) field on the other hand defines not only an axis, but also a direction in space. If a relatively weak, static electric field $\vec{E}$ is added that has a non-zero component $E_{\parallel}$ parallel to the laser polarization direction, an additional potential acts on the molecule

$$V_{dc}(\theta) = -\mu E_{\parallel} \cos\theta \tag{2.19}$$

that is proportional to the permanent dipole moment μ. This causes a relative shift of the two potential minima of the double well that favors $\theta = 0°$ over $\theta = 180°$, see Fig. 2.11(b). As a result, the molecular ensemble becomes *oriented* with respect to the space-fixed axis as is illustrated in Fig. 2.10(d).

2.4.3 Three-Dimensional Alignment and Orientation

A linear molecule is fully fixed in space when it is one-dimensionally oriented. A non-linear molecule however, can still freely rotate about the fixed axis. Alignment in three dimensions can be realized if a second double-well potential is introduced that acts on this rotation angle. This can be achieved by using elliptically polarized laser pulses. The potential energy in this case is minimized when the second most polarizable axis is aligned along the minor axis of the light polarization, as is shown in Fig. 2.10(c) [108]. The eccentricity of the ellipse can be tailored to match the anisotropic polarizability of a specific molecule, which maximizes the degree of three-dimensional alignment. For the case of an asymmetric top molecule, the polarizabilities along all three axes, α_{xx}, α_{yy}, and α_{zz} need to be considered [107]. Three-dimensional orientation can be achieved by adding a static electric field, see Fig. 2.10(e).

2.4.4 Nonadiabatic Laser-Alignment

Adiabatic laser-alignment has the disadvantage that experiments have to be carried out under the influence of a laser field, as the alignment disappears as soon as the pulse is turned off. An alternative approach is to align the molecules with very short laser pulses with picosecond to femtosecond durations [109]. The short pulse imparts a sudden 'kick' to the molecules that can transfer large angular momentum values, upon which they align after the laser turn off. Quantum mechanically, many rotational states are coherently excited, forming a rotational wavepaket which evolves in time, such that the prompt alignment is followed by temporal alignment revivals with a certain periodicity that depends on the rotational constant of the molecule. This process is referred to as *nonadiabatic, dynamical, impulsive* or *field-free alignment*. The latter stresses the fact that experiments under field-free conditions are possible, if the probe pulse arrives at an instant of time where alignment revival occurs. Nonadiabatic alignment in three dimensions as well as orientation can be achieved, however, the degree of alignment that can be obtained is typically less than for the case of adiabatic alignment [110].

In recent years, several efforts have been made to maximize the achievable degree of alignment as well as towards methods that enable field-free experiments on aligned and oriented molecules. The possibility of combining adiabatic and non-adiabatic alignment by simultaneous use of a picosecond and a nanosecond pulse has been investigated to achieve higher degrees of alignment [111]. Similarly, an adiabatic rise combined with a rapid turn-off of the pulse has been shown to induce revivals of the alignment, thus enabling measurement under laser-field free conditions [112]. Pulse-shaping techniques may potentially be able to achieve higher degrees of alignment as compared to the adiabatic limit [113]. Moreover, it was demonstrated recently that a certain degree of molecular orientation can be achieved by using a two-color laser field in the adiabatic regime [114] as well as completely field-free with non-adiabatic techniques [115].

3 Velocity Map Imaging of Photoelectrons

This chapter describes the set-up that was used for the photoelectron diffraction experiments in this thesis. Similar layouts were employed in one synchrotron and two Free-Electron Laser experiments, modifications are indicated in the respective paragraphs. Additional experimental parameters can be found in appendix A.3. After a general overview, the individual experimental components are briefly described and in the second part, the data acquisition and data processing procedure is explained.

3.1 Experimental Set-Up

All three experiments presented in this thesis were carried out in the CFEL-ASG MultiPurpose (CAMP) endstation [116], the general set-up is depicted in Fig. 3.1. Molecules were delivered to the interaction region as a supersonic molecular beam after passing through two skimmers and an electrostatic deflector. A *neodymium-doped yttrium aluminum garnet* (YAG) laser adiabatically aligned the molecular ensemble, which was first pumped by a *titanium-sapphire* (TiSa) laser and afterwards probed by an X-ray pulse. The resulting photoelectrons and fragment ions were extracted towards two *micro-channel plate* (MCP) detectors by the inhomogeneous electric field of a double-sided *velocity map imaging* (VMI) spectrometer. *Phosphor screens* were placed behind the MCPs that were read out from outside of the vacuum chamber by collecting the light with two CCD cameras. For the synchrotron experiment, *delay-line anodes* were used instead of phosphor screens. In the following, each aspect of the experimental set-up is addressed in more detail.

3.1.1 X-ray Lightsources

The centerpiece of the photoelectron diffraction approach in this work is the creation of a photoelectron from a core-level of a specific atom by single-photon ionization, as has been explained in section 1.2.4. Core-level binding energies range from 13.6 eV in hydrogen to 115 keV in uranium [31], thus a tunable lightsource with photon energies larger than 10 eV is desirable for this kind of experiments. *Synchrotron* facilities can provide photon energies of 10 eV to about 300 keV, at repetition rates of several MHz, making them an obvious choice.

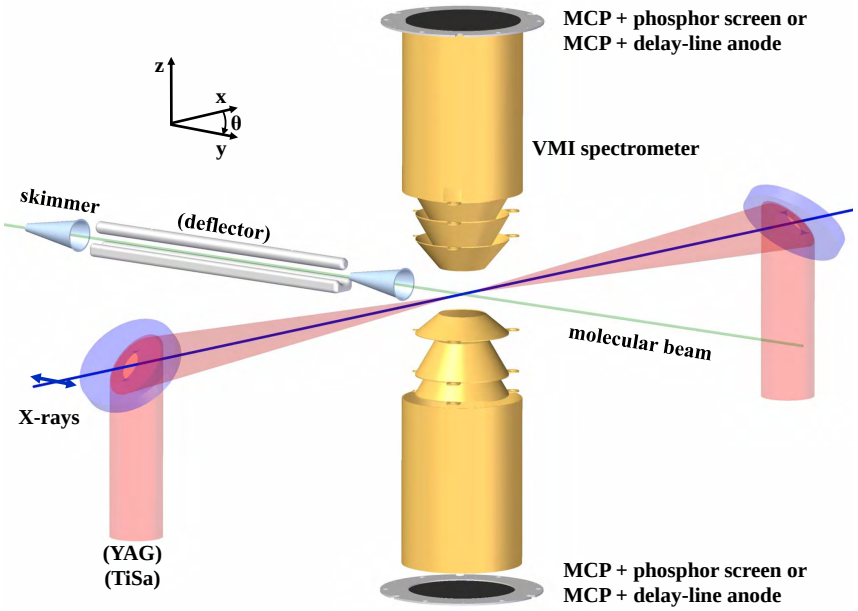

Figure 3.1: Set-up in the CAMP chamber for photoelectron diffraction experiments. Components labeled in brackets have only been used for one or two of the experiments presented in this thesis.

Static photoelectron angular distributions can be measured at a synchrotron by employing electron time-of-flight spectrometers and photoelectron-photoion coincidence techniques. Experiments that require temporal resolution in the femtosecond regime however, cannot be carried out with a standard synchrotron pulse, since it has a pulse duration on the order of 50-100 ps. Shorter pulses with durations of around 100 fs can be made available by applying slicing techniques [117]. Here, about 0.1 % of the electron bunch is shaped by a femtosecond laser pulse in a way that this part can be separated from the rest of the bunch, such that ultrashort X-ray pulses are available. However, this technique reduces the emitted number of photons per pulse drastically, which is often acceptable for solid-state experiments, but hampers significantly the amount of statistics that can be collected on a dilute gas-phase target.

Today, intense X-ray pulses with durations of only a few femtoseconds are available at *Free-Electron Lasers* (FELs). Currently, two FELs are operating in the hard X-ray regime, the *Linac Coherent Light Source* (LCLS) [120], and the *SPring-8 Ångström Compact Free-Electron Laser* (SACLA) [121]. FELs provide short, very bright pulses with $10^{12} - 10^{13}$ photons per pulse at repetition rates of up to 120 Hz. The number of photons per second at a synchrotron, distributed in $\sim 10^6$ pulses, is roughly the same as in a single FEL pulse. This dramatic difference in light intensity of about 10^6 has significant influence on the design of an experiment for the respective lightsource. An FEL is based on a linear electron accelerator in which very short, very intense electron pulses are created that leave the accelerator with an energy of a few GeV. The bunch then enters *undulators*, a periodic array of alternating dipole magnets, see Fig. 3.2(a). The magnetic field forces the relativistic electrons

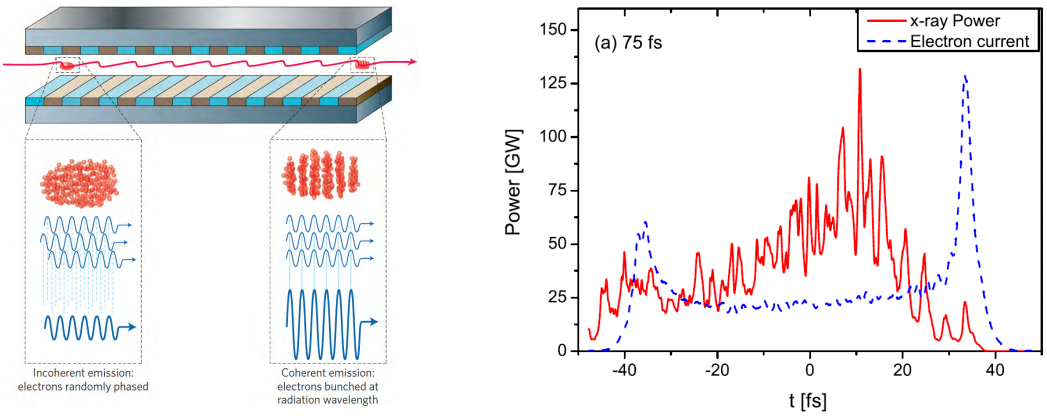

(a) (b)

Figure 3.2: (a) Electron trajectories and emitted light in an undulator of a Free-Electron Laser. The figure is taken from reference [118]. (b) Typical temporal structure of a single FEL shot. The figure is taken from reference [119].

on an oscillating trajectory that causes them to spontaneously emit synchrotron radiation in a narrow cone around their propagation direction. The radiation emitted from different electrons in the bunch adds up incoherently, thus the number of emitted photons is proportional to the number of electrons in the bunch [118]. Coherent light emission that scales quadratically with the number of electrons is achieved if electrons within one bunch are equidistantly spaced, with the distance between them being equal to the photon wavelength. This is called *microbunching*, which is the working principle of an FEL. It can be achieved by the interaction of the electron bunch with its own emitted X-ray field in very long undulator arrangements, as schematically illustrated in Fig. 3.2(a). The X-ray emission from such micro-bunches is referred to as *self-amplified spontaneous emission* (SASE).

The creation of amplified light pulses from spontaneous emission of radiation in an FEL has a significant influence on the pulse characteristics as compared to pulses that arise from stimulated emission, for example in an optical laser. In general, shot-to-shot variations of the mean photon energy, the pulse energy, and the arrival time of the FEL pulse occur, which has to be taken into account in the analysis of experimental data. Moreover, two FEL pulses are never identical, as the temporal and spectral structure of the SASE pulses is stochastic and contains many sharp spikes, as is shown for an exemplary FEL pulse in Fig. 3.2(b). The photon energy spectrum within a single pulse can be broad, and highly non-Gaussian. The average width of this spectrum is called *bandwidth* and is on the order of 0.2 - 1.0 % of the nominal photon energy for the regime of soft X-rays at the LCLS [120]. A practical drawback arises from the fact that although an FEL is a tunable lightsource, every photon energy requires electron pulses of different energy. Therefore, changing the photon energy at an FEL can take up to several hours, as compared to a synchrotron where this can be achieved within seconds, by varying the gap in the undulator.

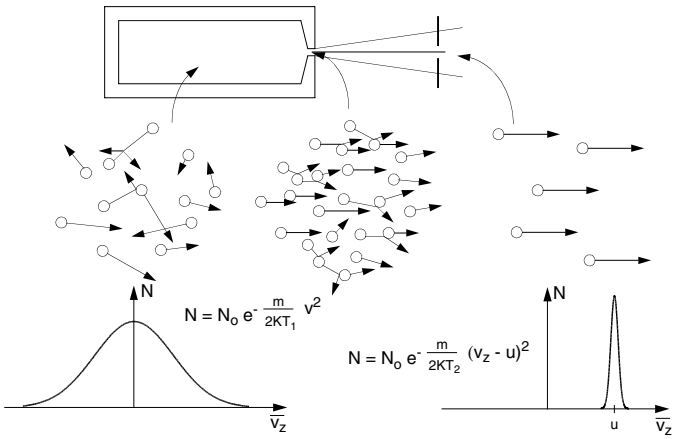

Figure 3.3: Principle of a supersonic molecular beam. Initially, N molecules of mass m have a stochastic velocity v at a temperature T_1. After supersonic expansion, behind a skimmer, a cold beam with a temperature T_2 is created and the velocity of the molecules is directed along the beam propagation direction z. The figure is taken from reference [124].

An alternative to accelerator-based lightsources is the creation of X-ray pulses from recolliding electrons in strong laser fields via high harmonic generation (HHG), as was briefly introduced in section 1.2.3 [42–44]. The resulting pulses can be very short, well below one femtosecond, but typically the number of emitted photons is low, as the yield of HHG decreases strongly for high photon energies.

The experiments shown in this thesis were performed at the *Variable Polarization XUV Beamline P04* [122] at the PETRA III synchrotron at DESY in Hamburg in December 2013 (chapter 4.1), and at the *Atomic, Molecular and Optics* (AMO) beamline [123] of the LCLS in May 2010 and June 2011. Additional measurements were carried out at the DORIS III synchrotron at DESY.

3.1.2 Supersonic Molecular Beams

A gas-phase molecular ensemble of high density and low temperature is required for the photoelectron diffraction experiment. This is created by *supersonic expansion*, as is illustrated in Fig. 3.3. A volume V_1 of an ideal gas of atoms with mass m with a pressure p_1 (here $p_1 \geq 10^2\,\mathrm{mbar}$) is connected to a volume V_2 of lower pressure p_2 (here $p_2 \leq 10^{-4}\,\mathrm{mbar}$) through a small hole, a *nozzle*. The gas expands through the nozzle, and for $p_1/p_2 > 2$ the velocity of the particles is larger than the speed of sound [125]. In this case, the expansion happens adiabatically. Conservation of energy requires that

$$U_1 + p_1V_1 + \frac{1}{2}mv^2 = U_2 + p_2V_2 + \frac{1}{2}mu^2, \tag{3.1}$$

where U_1 and U_2 are the internal energies, and v and u the collective velocities of the ensemble of atoms before and after expansion, respectively [126]. Initially, the gas

with a temperature T_1 is in thermal equilibrium, thus $v = 0$. Moreover, as $p_2 \ll p_1$, it can be assumed that $p_2 \approx 0$. This results in

$$U_1 + p_1 V_1 = U_2 + \frac{1}{2} m u^2 \tag{3.2}$$

$$\frac{3}{2} k_B T_1 + k_B T_1 = \frac{3}{2} k_B T_2 + \frac{1}{2} m u^2, \tag{3.3}$$

where k_B is the Boltzmann constant. Upon expansion, the enthalpy $H = U_1 + p_1 V_1$ of the gas is converted to a directional movement by inter-atomic collisions, resulting in a mean collective velocity u along the expansion direction. This implies that the gas cools down, thus the distribution of velocity components narrows, see Fig. 3.3. In the ideal case $T_2 = 0\,\mathrm{K}$, resulting in a velocity

$$u = \sqrt{5 k_B T_1 / m}. \tag{3.4}$$

Typical values for rare gases at room temperature are $u = 1700\,\mathrm{m/s}$ for helium, $u = 550\,\mathrm{m/s}$ for argon and $u = 300\,\mathrm{m/s}$ for xenon. However, under experimental conditions, the internal energy is not fully converted into directional movement, and $T_2 \geq 0\,\mathrm{K}$. The molecular beam can be characterized by the *speed ratio* [127] that is defined as

$$S = \sqrt{\frac{m u^2}{2 k_B T_2}}. \tag{3.5}$$

The speed ratio is a function of the product of the diameter d of the nozzle and p_1. The dependence of S on $p_1 d$ for a helium beam can for example be found in reference [127]. The beam of isolated atoms resulting from supersonic expansion is then collimated by one or multiple *skimmers*, which cut out the central, coldest part of the beam. Here, two skimmers are used that are shaped like an inverse funnel, see Fig. 3.1.

In contrast to rare gases, larger molecules are often not in the gas phase at room temperature and under normal pressure conditions. The necessary temperatures to bring them into the gas phase can be very high and the desired target densities after expansion may not be achieved simply by heating the reservoir before expansion. Also, due to cooling during expansion, dimers or clusters of molecules may form [125]. Moreover, at high temperatures, the molecules may disintegrate. Instead, of rising the temperature, the pressure can be lowered in order to bring the molecules into the gas phase. A liquid sample can be filled into a reservoir, a so-called *bubbler* and a *carrier gas* is floated either above the surface or directly through the sample. The gas flow picks up sample molecules and delivers them to the interaction region. Alternatively, a solid sample can be stored in a filter paper which is directly transmitted by the carrier gas. During expansion, the temperature of the molecules decreases, as the energy is distributed equally between molecules and carrier gas through collisions. The final temperature is typically a few Kelvin,

leaving the molecules in the electronic and vibrational ground state. To select the rotationally coldest molecules, an electrostatic deflector can be used in addition [128]. Sending a beam of polar molecules through a strong, inhomogeneous electric field spatially separates the molecules according to their rotational quantum state by exploiting the Stark effect. This can also be used to separate the molecules from the carrier gas or to separate different conformers of one molecular species [129].

For the two LCLS experiments, molecules were applied to a filter paper and then were introduced into the CAMP chamber by supersonic expansion with helium as the carrier gas. A pulsed Even-Lavie valve [130] was used in order to reduce the total gas flow, and the polar molecule 1-ethynyl-4-fluorobenzene in chapter 4 was sent through a deflector between the skimmers, see Fig. 3.1. For the synchrotron measurement, a different, continuous beam without a deflector was employed and the molecules were filled into a reservoir and heated to about 60°C.

3.1.3 Velocity Map Imaging

When an X-ray pulse crosses the molecular beam and ionizes a molecule, electrons and molecular fragments are created. In order to collect them, an electrostatic field is applied to the interaction region that accelerates electrons and ionic fragments to opposite sides, where position-sensitive detectors are placed, see section 3.1.4. In this work, an inhomogeneous electric field was applied to focus the charged particles. This is referred to as velocity map imaging and was first introduced by Eppink and Parker [131]. They used three electrodes which, for properly chosen voltages, form electrostatic lenses that project all particles with the same initial momentum to the same spot on the two-dimensional detector. The resulting radius on the detector is, in very good approximation, proportional to the square root of the kinetic energy and the proportionality factor can be obtained from calibration, see section 3.2.6. Collection efficiency for the full 4π solid angle can be achieved for electrons with moderately low field strengths when using such inhomogeneous fields.

Moreover, in velocity mapping, the position at which the charged particle hits the detector is relatively insensitive to the exact location of the origin of the charged particle, which is an important property for experiments using extended, gas-phase targets. A molecular beam from supersonic expansion typically has a diameter on the order of a few mm in the interaction region, given by the distance to the last skimmer and the divergence of the molecular beam, defined by the skimmer diameters and the distance between them. Single-photon ionization, as used for photoelectron diffraction, can arise anywhere along the path of the light beam through the molecular ensemble, thus creating an extended interaction region of a few mm.[1] The resulting uncertainty in the origin of the created electron or ionic fragments directly

[1] At the *P*04 beamline at PETRA, the X-ray beam was unfocused in the direction along the molecular beam at the time of the experiment, thus an interaction region of about 3×3 mm was created in this case.

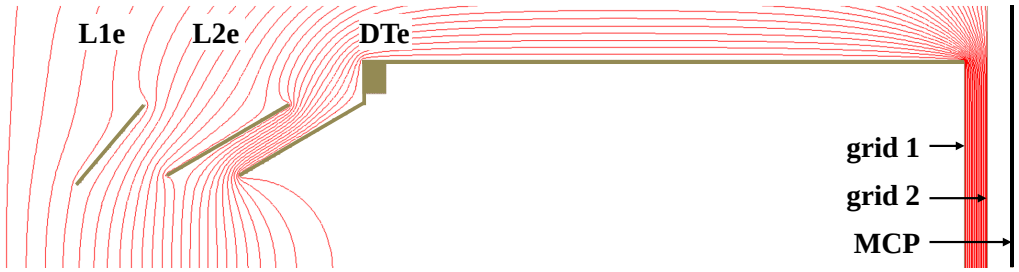

(a) Electrostatic potential on the electron side

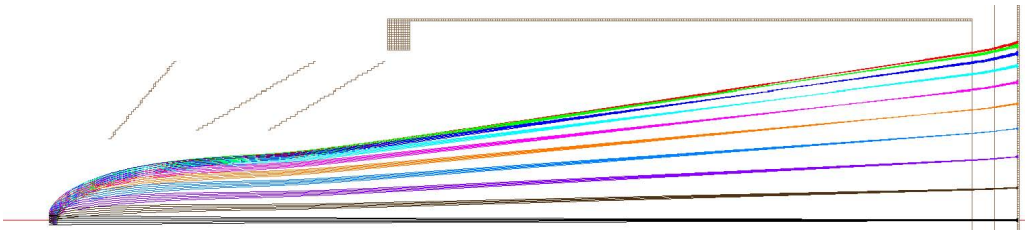

(b) 100 eV electrons

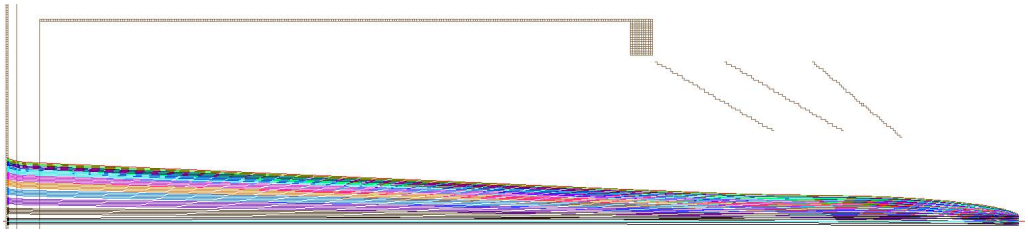

(c) 10 eV F^+ ions

Figure 3.4: (a) Electrostatic potential on the electron side of the spectrometer for operation voltages of L1e: 1 kV, L2e: 3 kV, DTe: 7 kV and voltages of opposite polarity on the ion side. The third conical electrode is connected to the drift tube. (b) and (c) Trajectories of electrons and ions on opposite sides of the VMI spectrometer. Colors correspond to different ejection angles with respect to the spectrometer axis from 0 to 90° with 10° spacing. The five different particles of the same color have different origins between -2 and +2 mm offset from the spectrometer axis.

translates into a blurring of the recorded hit position, if homogeneous electric fields are used. This blurring can be avoided to a large extent when using appropriate focusing fields as usually applied in velocity map imaging.

In the original design by Eppink and Parker, either positive or negative particles can be detected, a coincidence measurement, however, requires recording electrons and fragment ions at the same time. Experiments on laser-aligned molecules also profit from simultaneous imaging of ions and electrons, therefore a double-sided VMI spectrometer was used in this work that is shown in Figs. 3.1 and 3.4. Details of the design have been described in reference [132]. On both sides, three electrodes create electrostatic lenses, see Fig. 3.4(a), followed by a field free drift region inside a cylindric tube that is terminated by a copper grid with about 78% transmission. Electrons and ions are detected on micro-channel plate detectors, see section 3.1.4,

in front of which a second grid is placed. The unusual shape of the electrodes was designed for measurements where an additional pnCCD photon detector was located outside of the spectrometer to collect diffracted photons and fluorescence [116]. In order to minimize shadows on the detector, the shape of the electrodes was chosen conical, with different angles, each pointing at the interaction point.

Figures 3.4(b) and 3.4(c) show the focusing properties of the VMI spectrometer on the electron and ion side, respectively, as simulated with the program SIMION [133]. The voltages can be chosen such that photoelectrons and fragment ions with kinetic energies of up to 100 eV are collected in the full 4π solid angle. Shortening of the field-free drift region on the right hand side of Fig. 3.4(b) from 127 mm to 50 mm allowed for detection of electrons with kinetic energies of up to 250 eV in the PETRA experiment. All charged particles with the same initial momentum are imaged to the same radius, almost independent of their exact origin. The position of the focal point along the spectrometer axis is however slightly radius dependent, as is best seen in the electron trajectories. This arises from the particular design of the spectrometer and could probably be avoided by using ring electrodes [134]. In the existing spectrometer, the focusing voltages should be chosen such that best focusing is achieved for the radius region of interest, usually at large radii for recording photoelectrons. The choice of voltages also depends on the experimental conditions, for example on the exact position of the X-ray beam with respect to the spectrometer, and thus have to be tuned for each experiment until optimal imaging is achieved. For the LCLS experiment on 1-ethynyl-4-fluorobenzene molecules, a cylindrical μ-metal shield was placed around the spectrometer (not shown), with the idea to shield the electrons from external magnetic fields. A μ-metal shields a volume from magnetical field lines due to its high magnetic permeability. However, it was not tested whether this had a significant impact on the electron images as the μ-metal was not removed during the experiment.

3.1.4 Electron and Ion Detection

The spectrometer extracts ions and electrons in opposite directions and focuses them onto two micro-channel plates. These two-dimensional electron multipliers, are penetrated by many isolated channels with a diameter of 25 μm that are tilted with respect to the detector surface. To increase the sensitivity and the charge multiplication, two plates are stacked such that the tilted channels form a V-shape. Impinging particles or photons that enter such a channel create electrons that are then accelerated by a positive high voltage that is applied between the front and the back side of the plate. The signal is thus multiplied within the channel, such that a cloud of electrons can be detected at the exit. The corresponding drop in the MCP voltage together with an absolute trigger provides the *time of flight* of the particle to the detector. As the electron cloud is created locally in one channel in the first plate, and then spreads out into only few channels in the second plate, information on the

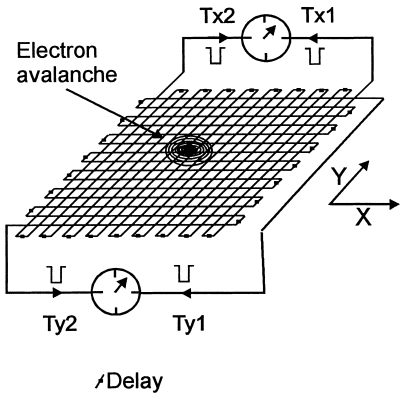

Figure 3.5: Principle of a delay-line-anode. The figure is taken from reference [135].

spatial position of the particle hit can be obtained when the charges are detected by a two-dimensional, position-sensitive detector placed directly behind the MCP.

Different read-out techniques can be used, depending on the experimental requirements. Often it is desired to image only a single ionization event in every readout cycle in a photoelectron-photoion coincidence mode [19]. For this purpose, a *delay-line-anode* [135] can be used, its working principle is illustrated in Fig. 3.5. Two pairs of wires are wound such that they form a square grid that acts as an anode, the spacing between the windings is 0.5 mm. A voltage of about 50 V is applied to both ends of each wire, usually one wire is put on a positive voltage, and the other one is negative, two wires for each dimension form a *Lecher line*. The electron cloud that is created by the MCP induces a current pulse in both wires that propagates to both ends of each wire pair. The difference in arrival times $T_{x1}-T_{x2}$ and $T_{y1}-T_{y2}$ between the two ends of one wire pair encodes the information on the position: For a hit in the center of the detector, both delay times are equal, whereas an event on the edge of the detector produces one long and one short delay. In a hexagonal version of the detector, three pairs of wires are used instead of two to improve the multi-hit capacity by recording redundant information. The signals are amplified, digitized by a constant fraction discriminator, and then saved as a list of arrival times that can be translated into time-of-flight and position information, and, thus, momentum of each individual particle. For the experimental settings used here, three-dimensional momenta can only be retrieved for ions. For electrons, the total time of flight is very short, such that the resolution in z-direction is low and only the two components p_x, p_y of the momentum parallel to the detector plane are measured.

Delay-line anodes are very well suited if only a few particles are created per readout cycle, with high repetition rates. These detectors are thus often used in synchrotron experiments. For an experiment at a Free-Electron Laser, however, where $\sim 10^{12}$ photons are contained in a single shot, at repetition rates of $\leq$120 Hz, it is often desired to record hundreds of particles per readout cycle. For example, in the experimental data presented in chapter 5, up to 700 electron hits were created from a single pulse. For such conditions, a *phosphor screen* can be placed behind the MCP.

Each impinging electron cloud causes luminescence on the screen that persists for 4 ms (P20 phosphor), and all light spots created for one X-ray pulse are imaged by a CCD camera from outside of the vacuum chamber through a window flange. The number of detectable and distinguishable detector hits per shot is in this case only limited by the overall size and the density of the individual spots. When using a phosphor screen, usually the information about the time of flight of the particle at a certain position is lost, as the camera records the integrated image for each FEL shot. In order to image only the spatial distribution of ionic fragments with a certain mass-to-charge ratio, the ion detector is gated by fast switching of the high voltage on the MCP. To record a time-of-flight spectrum, see section 3.2.1, the temporal gate has to be removed. The electron detector is gated also, to suppress stray electrons and high-frequency feedback from the gating of the ion detector. For this work, P20 phosphor screens with CCD cameras were used at the LCLS, whereas two delay-line anodes were used in the PETRA experiment.

It has been shown recently that a new event-triggered monolithic pixel detector, the *Pixel Imaging Mass Spectrometry* (PImMS) camera [136], in combination with a P47 phosphor screen that decays within 100 ns, can record time-of-flight spectra with a temporal resolution of 12.5 ns, while at the same time retaining the spatial position information of all ionic fragments [137]. This is a very interesting alternative for future experiments of this kind, if delay-line anodes cannot be used due to too high count rates per readout cycle.

3.1.5 Laser Set-Up

For the photoelectron diffraction experiment, it is necessary to fix the molecular frame with respect to the laboratory frame. In the LCLS experiments, where multiple molecules are ionized in every X-ray pulse, this was achieved by adiabatic laser-alignment of the molecules, see section 2.4. Here, a 1064 nm (1.17 eV) neodymium-doped yttrium aluminum garnet laser with a pulse duration of 10 ns and an intensity of about $5 \times 10^{11}\,\mathrm{W/cm^2}$ was used. The intensity is chosen low enough such that strong-field ionization of the molecules by the alignment laser alone is prevented.

In order to assure that all molecules that are ionized are well aligned, the focus size of the YAG was chosen about a factor of 4 larger than the FEL focus. The FEL and YAG pulses were synchronized in time, such that the X-ray pulse hit the molecules in the peak of the alignment. The relative timing was found based on optimum alignment as determined from the ion-fragment distribution. The YAG laser operated at a repetition rate of 30 Hz, and the LCLS at 120 Hz (60 Hz in 2010). As the molecular beam was operated at a repetition rate of 60 Hz, aligned and randomly oriented molecules were measured alternately, and, in addition, background data were recorded simultaneously. Linearly or elliptically polarized pulses were used that induce one- and three-dimensional alignment respectively.

For the pump-probe data in chapter 5, additionally an 800 nm (1.55 eV) titanium-sapphire laser was used that induced fragmentation of the molecules. The pulse duration was 70 fs and the intensity was set to about $5 \times 10^{14}\,\mathrm{W/cm^2}$ in order to create predominantly singly-charged fragments. The focus size of the TiSa was chosen about a factor of 3 larger than the FEL focus size and about a factor of 2 smaller than the YAG focus size. The temporal overlap between FEL and TiSa was found by first monitoring the arrival times of both light pulses with a fast photodiode that can achieve a precision of about 20 ps, and afterwards tuning on a delay-dependent signal in the electron image, see section 5.2.4.

3.2 Data Processing

This section describes basic techniques that were employed to analyze the electron diffraction and the corresponding ion data. Data in the PETRA experiment were acquired and pre-analyzed with the software package COBOLD [138], data from the LCLS with the CFEL-ASG Software Suite (CASS) [139]. Final analysis of all data was performed with ROOT [140].

Unless otherwise noted, all data presented in this thesis follow the convention in Fig. 3.1. The light-propagation direction lies along the x-axis, the molecular beam propagates along y, and the z-axis is the time-of-flight axis. Detector images show the particle momentum components p_x in horizontal direction and p_y in vertical direction; $p_x = p_y = 0$ lies in the center of the image. All detector images for one experiment show the same (x, y) range, and all images in one figure are plotted with the same color scale. Electron angular distributions in the (x, y) plane are plotted as polar plots and the angle ϕ lies in the detector plane with $\phi = 0$ corresponding to the light propagation direction. For ions, the symbol θ_{2D} is used instead of ϕ, in accordance with common nomenclature in molecular alignment literature.

3.2.1 Ion Time-of-Flight Spectra

The starting point of a photoionization experiment is often to characterize the ionic fragments that are created by recording a *time-of-flight spectrum*. The time T it takes a particle to pass a length L in a constant electric field E is proportional to its mass-to-charge ratio m/q

$$qE = \frac{mv^2}{2} = \frac{mL^2}{2T^2} \qquad \Rightarrow \qquad T = \sqrt{\frac{L^2}{2E}\frac{m}{q}}, \tag{3.6}$$

under the assumption that the initial kinetic energy is small compared to the energy that the particle gains from the electric field. Thus, the amount of charge that is deposited on an MCP as a function of time characterizes the relative abundance of ionic fragments that are created.

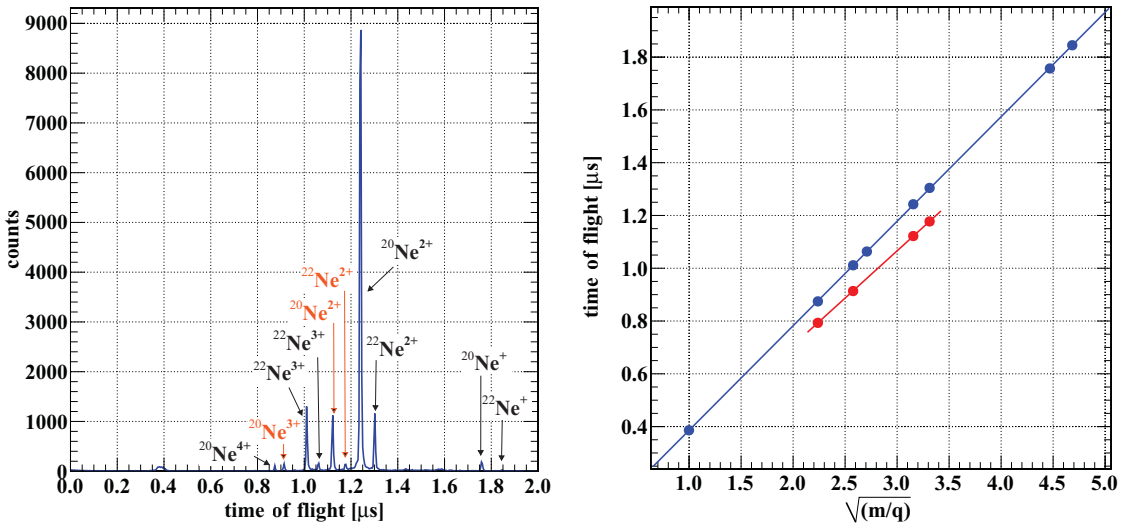

(a) (b)

Figure 3.6: (a) Example of a time-of-flight spectrum for neon, recorded with velocity map imaging voltages at a photon energy of 893 eV at DORIS. Peaks marked in red are copies of real peaks that are shifted to shorter flight times (see text). (b) The time of flight is plotted as a function of $\sqrt{m/q}$ to verify the calibration. Real peaks are shown in blue, copies of real peaks in red. A linear fit through the points is also plotted.

The measured spectrum can be calibrated by "educated guessing", in the sense that two peaks are assumed to correspond to certain ratios m/q. Often the peak with the shortest time of flight stems from protons and the peak with the longest time of flight stems from the singly charged atom, or the intact molecule that is referred to as the *parent ion*. The resulting calibration is cross-checked with other flight times in the spectrum, to ensure that all of the peaks can be assigned to an m/q ratio. An exemplary time-of-flight spectrum of neon atoms recorded at a photon energy of 893 eV is shown in Fig. 3.6(a). Predominantly the Ne($1s$) level is ionized, which leads to an Auger decay in almost all cases, see also section 2.1, thus the most probable ion to be created is Ne^{++}. The calibration is done by plotting T over $\sqrt{m/q}$, as shown in Fig. 3.6(b). The flight times can also be calibrated by recording the spectrum for a rare gas and comparing it to literature results or by simulating the ion trajectories for the given spectrometer voltages, for example in SIMION [133].

With the VMI spectrometer used in this work, time-of-flight spectra can either be recorded by applying constant voltages on all electrodes, for example +1 kV on the electron side and −1 kV on the ion side, or with the typical velocity map imaging voltages. However, in the VMI mode additional peaks arise in the time-of-flight spectrum, marked in red in Fig. 3.6(a). This can be explained by the following scenario: An ionic fragment is accelerated to a kinetic energy of several keV by the extraction field of the spectrometer. Typically, a negative voltage of ≥ 3 kV is applied to the drift tube on the ion side, and to the attached grid, see Fig. 3.4(a).

Behind the drift tube, the electric field changes its direction, as about -2.6 kV are applied to the second grid in front of the MCP, such that the ions are decelerated before hitting the detector. The grid at the end of the drift tube has a transmission of only about 78 %, therefore the ion can impinge on the grid instead of passing through it, thereby creating electrons. These electrons are then accelerated towards the ion detector, and are thus detected with a time of flight that is somewhat shorter than the time of flight of the corresponding ion, due to the smaller mass of the electron. This means that for time-of-flight spectra recorded under velocity-map-imaging conditions, each ion peak is accompanied by an additional, smaller peak that is shifted to shorter flight times and that does not correspond to the flight time of an ionic fragment. The height of each 'copy' peak is scaled down with respect to the corresponding ion peak, such that the 'copy' peaks are particularly visible for strong ion peaks. The time-of-flight difference between the real peak and the 'copy' peak is not constant, but it scales with the mass of the ion, as heavier fragments need more time to traverse the region between the grid at the end of the drift tube and the MCP detector, while the created electrons travel at the same speed.

The flight times of two or more ions that are recorded in coincidence are often plotted in a two-dimensional representation, a *photoion-photoion coincidence* (PIPICO) map. Here, the flight time of the first detected ion is plotted on the x-axis and the flight time of the second ion on the y-axis. The resulting lines contain detailed information on the molecular fragmentation. For example, channels corresponding to the break-up into two charged fragments generally produce sharp diagonal lines as a result of momentum conservation, whereas when three or more charged fragments are created that each carry a significant amount of momentum, the corresponding line is washed out [141]. A PIPICO map is shown in section 4.1.

3.2.2 Data Sorting and Filtering

The analysis of photoelectron diffraction data requires integration of events over a rather long period of time, typically more than one hour. For a quantitative analysis, it is thus important that the experimental parameters are kept constant for all events that are analyzed together. However, as FEL pulses are generated from the stochastic SASE process, see section 3.1.1, nominal values such as the photon energy can fluctuate significantly. At the LCLS, beam parameters are monitored on a shot-to-shot basis, for example the electron-beam energy, the electron peak-current, and the integrated electron-beam charge. In order to remove outliers, for example electron pulses that did not produce SASE, from the data, broad filters are defined on these three parameters before proceeding with the data analysis. The photon energy cannot be monitored directly, but can be calculated from the measured electron energy and undulator parameters as

$$\lambda = \frac{\lambda_u}{2\gamma^2}\left(1 + \frac{K^2}{2}\right) \qquad \text{with} \quad \gamma = \frac{E}{m_e c^2} \qquad \text{and} \quad K = \frac{eB_u\lambda_u}{2\pi m_e c}, \tag{3.7}$$

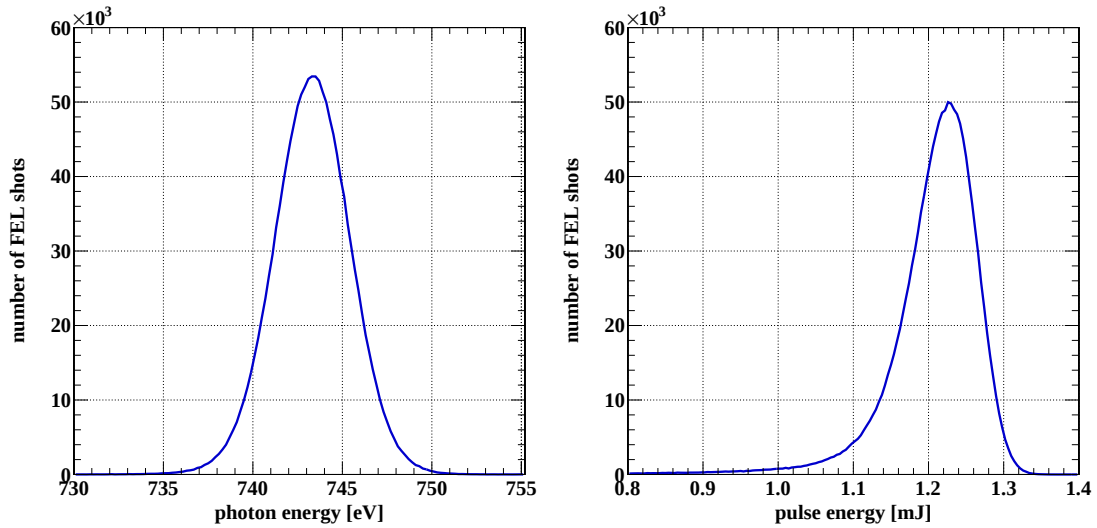

Figure 3.7: LCLS beam parameters for one set of data. (a) Distribution of the mean photon energy. (b) Distribution of the mean pulse energy.

where λ_u is the undulator period, E is the electron energy, and B_u is the peak magnetic field in the undulator [142]. Figure 3.7(a) shows a typical distribution of the X-ray energy. It fluctuates with a full width at half maximum (FWHM) of 5 eV around the center at 743 eV, corresponding to a variation of 0.7 %. The photon energy directly determines the kinetic energy of the photoelectrons, thus it is important to restrict it as good as possible to obtain sharp photolines. This can be achieved by filtering the data, for example such that only events with a photon energy in a window of $\pm$ 2 eV around the maximum of the distribution are analyzed. This corresponds to a variation of 0.27 %, which is of the same order as the lower limit of the bandwidth of each pulse of 0.2 % [120], such that it is not reasonable to narrow it down further.

It turned out during the experiment that constant monitoring of all parameters is not only necessary for a quantitative data analysis, but also important to check for systematic, artificial changes in beam parameters. In the 2011 LCLS experiment, the photon energy sometimes experienced a systematic shift with a 30 Hz frequency, and as the YAG laser operates at the same frequency, this meant that photoelectrons of different kinetic energies were created for aligned and randomly oriented molecules. This shift could not be corrected by filtering, thus these data could not be analyzed. For later measurements, the shift was corrected by optimizing machine parameters.

In addition to the filtering based on beam parameters, the data need to be sorted according to different experimental settings: The LCLS operated at 120 Hz (60 Hz in 2010), the YAG alignment laser at 30 Hz and the molecular beam was chosen to run at 60 Hz. This results in three data sets for the 2011 experiment: a quarter of the events corresponds to aligned molecules, another quarter to randomly oriented

molecules and half of the shots are background shots. In 2010, no background could be recorded. A photodiode monitored the YAG laser signal, and all shots in which the laser pulse was detected are regarded as 'YAG-on' shots. All events are classified in the pre-analysis step using CASS, and the number of events in each category is tracked, such that the resulting images can be normalized accordingly.

3.2.3 Hit Finding

The CCD cameras on the ion and on the electron side are read out for every FEL shot, and the image is saved with a resolution of 1024×1024 pixels. Part of a typical single-shot image on the electron detector is shown in Fig. 3.8(a). The electron clouds that are created by the MCP show up as bright spots on the phosphor screen. The overall size of the spot and the signal height depend on the statistical electron multiplication in the MCP, and on how many channels of the second MCP are hit by the electron cloud created in the first MCP. Moreover, the total energy of the post-accelerated particle, and the local MCP, phosphor, and CCD sensitivities influence the signal. The signal height cannot be exploited in the analysis. Thus it is preferable to reduce each hit to a single position information, to remove artificial sensitivity variations and to improve the spatial resolution.

First, a threshold value has to be defined that reliably separates signal from noise. This can best be done by plotting the distribution of signal heights per pixel in the image for the complete set of data, see Fig. 3.8(d). The distribution consists of two different contributions: the vast majority of signals per pixel (2×10^{10}) lie between 0 and 40 in arbitrary detector units, which correspond to noise. It can be removed from the image by defining a threshold of 40 arb. u., resulting in the image in Fig. 3.8(b). Most of the data, however, were recorded with a lower voltage applied to the MCP detector that gives rise to the signal-height distribution in Fig. 3.8(e). The reduced amplification results in two different contributions that both correspond to particle hits, but in different regions of the detector. The central part of the MCP is less sensitive than the outer part, because it had previously suffered from damage effects due to intense signal, resulting in lower signal heights. The noise distribution in this case is not completely separated from the signal of pixels that contain a real signal, such that it is unavoidable to lose some of the weaker hits in the center.

After applying the threshold, the images are processed with the hit-finding algorithm of CASS [139]. The original method was developed to identify photon hits on the CAMP pnCCD detector, on which one hit covers at most 4 pixels. For every pixel in the image, the signal height is compared to the signal in the 8 nearest neighbor pixels. If this signal is higher than in all surrounding pixels, the pixel is recognized as a hit. However, electron and ion hits on the phosphor screen spread out over many more pixels (>20 for most hits). Thus it can happen that wrong double hits are produced when a local maximum is mistaken for a global maximum. The algorithm has therefore been modified such that also the next 16 surrounding pixels

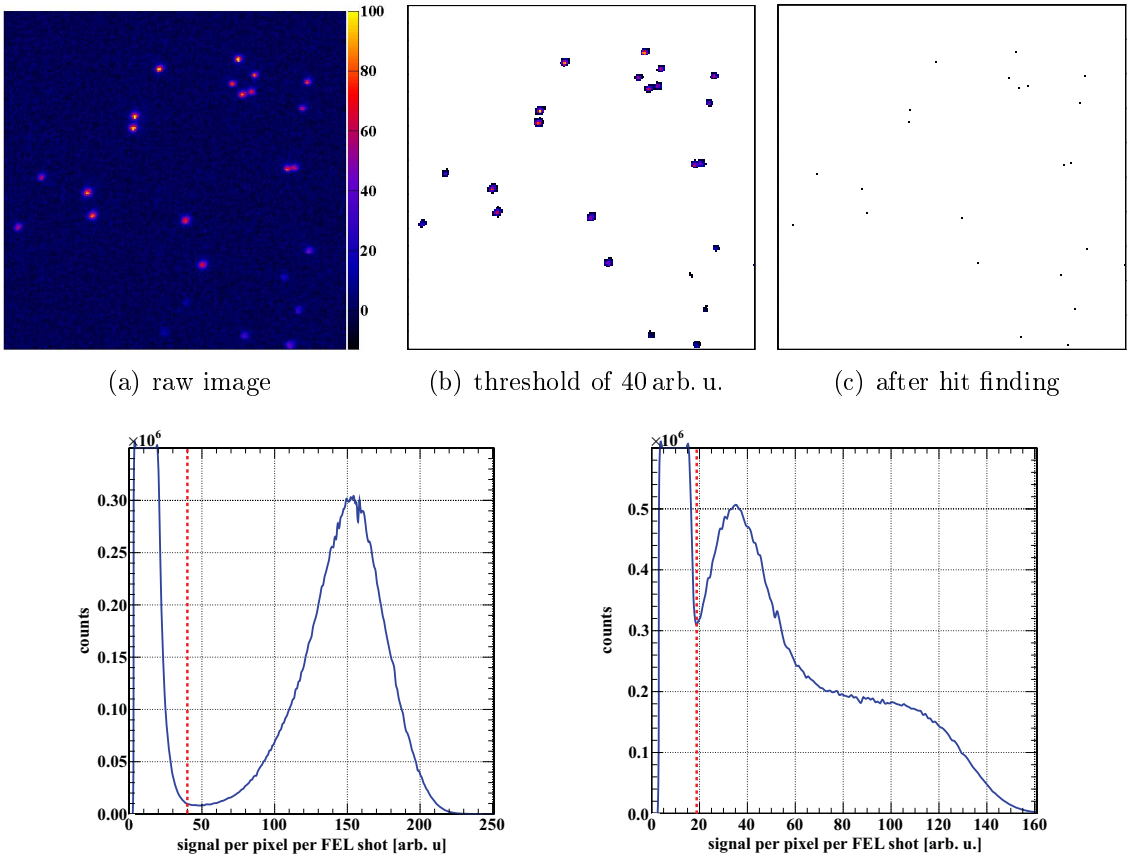

(a) raw image (b) threshold of 40 arb. u. (c) after hit finding

(d) 2.4 kV applied to MCP (e) 2.2 kV applied to MCP

Figure 3.8: Top: single shot electron detector image, zoomed in to 200×200 pixels in the center of the image. Bottom: distribution of signal heights per pixel on the electron detector for two different voltages applied on the back side of the MCP. Thresholds to separate signal from noise are indicated by the red dashed lines.

are taken into account in the comparison. It has been found that this successfully avoids artificial hits in almost all cases. The result of the hit-finding algorithm on Fig. 3.8(b) is shown in Fig. 3.8(c). Another problem arises if two adjacent pixels have the exact same signal height, which starts to become a problem for low absolute signal height values, for example in Fig. 3.8(e). The original algorithm counts two hits in this situation, whereas the modified code counts zero; one of these occurrences can be found in the upper right corner of the image in Fig. 3.8. Both cases are obviously not ideal, thus the implementation of a center-of-mass calculation would probably be beneficial. This would also further improve the spatial resolution, as the pixel with the maximum signal height does not necessarily correspond to the exact center of the position.

For the following analysis, all hits that were identified in the single shot images are summed up for a sub-set of data with identical experimental parameters. An example of such an integrated electron image is shown in Fig. 3.9(a). It looks noisy

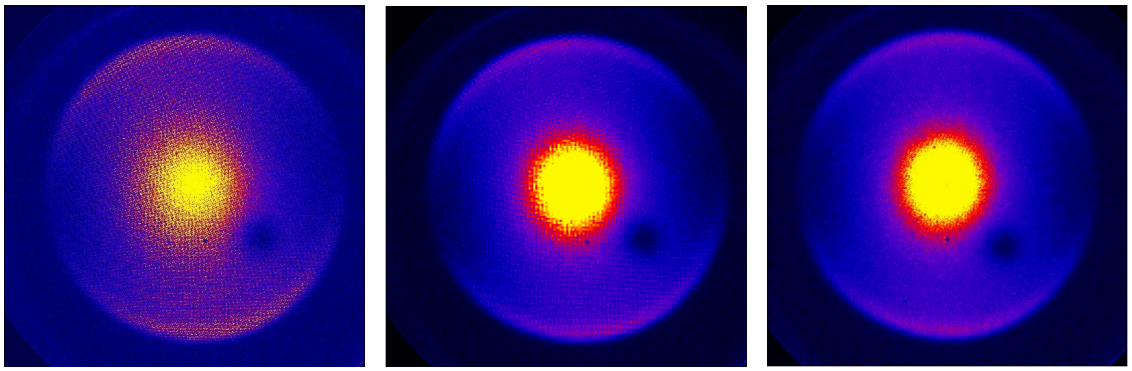

(a) result of hit finding (b) rebinning 4×4 pixels (c) smoothing over 5×5 pixels

Figure 3.9: Comparison of rebinning and smoothing of a typical integrated electron detector image. (c) is rotated by 10° with respect to (a) and (b), correcting for a slight rotation of the camera with respect to the detector. The 'hole' in the lower right quadrant corresponds to an insensitive area on the phosphor screen that had previously been damaged by too intense signal.

at this maximum resolution, and a fine, artificial structure can be identified that is most probably caused by the two grids that were placed in front of the MCP. In order to average over these effects, the number of pixels can be reduced by *rebinning*, in this case adjacent pixels are merged to one bigger pixel and the signals are added up. Rebinning the image in Fig. 3.9(a) by a factor of 4 results in Fig. 3.9(b). Another possibility is to employ a two-dimensional *smoothing* algorithm that is implemented in ROOT, and which interpolates between the signals of neighboring pixels instead of only summing them up, while preserving the original image resolution. When comparing the resulting Fig. 3.9(c) with Fig. 3.9(b), it is found that the smoothing removes the artificial structure more efficiently, which is probably because it has a periodicity of several pixels. Therefore, the two-dimensional images have been smoothed after converting them to polar coordinates.

3.2.4 Image Conversion and Correction

In order to extract photoelectron angular distributions from the two-dimensional detector image, it is converted from cartesian (x, y) to polar coordinates (r, ϕ). This allows to obtain angular distributions by projecting a certain radial range, and to easily correct for an experimental offset angle by shifting the (r, ϕ) histogram along the ϕ axis. For the coordinate transformation, the correct center of the photoelectron distribution has to be determined. In velocity map imaging, the point on the detector to which particles with zero initial kinetic energy are projected does not necessarily define the center of the photoelectron distribution at larger radii. Thus, the question arises how to find the correct center to evaluate the photoelectron angular distribution. In first approximation, this can be done by simple geometric considerations, but it is difficult to achieve a precision of better than a few pixels.

To improve the result, two methods have been used. One possibility is to define a center and then to compare the radial distribution of electrons that are obtained for the four different quadrants of the image. If the rim of the projected photoline is found at the same radius for all four quadrants, the center is correctly chosen. A second method is to cut out a ring from the image that contains the rim of the projected photoline. This ring is then mirrored on one axis and the signals of both resulting rings are multiplied pixel-by-pixel and added up. If the center is chosen correctly, the integrated signal obtained in this way is maximized.

The conversion of the image to polar coordinates is achieved by defining an equidistant lattice with points (r_i, ϕ_j), whose origin is located at the center of the photoelectrons. The spacing between the grid points needs to be chosen small enough, such that even for the largest radius each cartesian pixel contains at least one point of the polar lattice. For the CCD images that contain 1024×1024 pixels, a polar lattice with 512 radial points and 1800 angular points has been used. The photoelectron count rate $N(r_i, \phi_j)$ in each bin of the polar lattice is given by

$$N(r_i, \phi_j) = r_i N(x, y) \tag{3.8}$$

with $x = r_i \cos\phi_i$, $y = r_i \sin\phi_i$. Here, $N(x, y)$ is a two-dimensional interpolation of the counts in the four surrounding cartesian pixels (x_1, y_1), (x_1, y_2), (x_2, y_1) and (x_2, y_2)

$$\begin{aligned} N(x, y) =& N(x_1, y_1)(x_2 - x)(y_2 - y) + N(x_2, y_1)(x - x_1)(y_2 - y) \\ &+ N(x_1, y_2)(x_2 - x)(y - y_1) + N(x_2, y_2)(x - x_1)(y - y_1). \end{aligned} \tag{3.9}$$

After the detector image is converted to polar coordinates, angular distributions are easily obtained by projecting the two-dimensional (r, ϕ) plots to the ϕ-axis for a certain radial region of interest $(r_{\min}, r_{\max})$. In the same way, radial distributions can be obtained from projections of a certain range of angles. Note however that this introduces an additional factor of r due to the conversion $dx\,dy = r\,dr\,d\phi$ that enforces $N(r = 0) = 0$. All radial distributions from non-inverted detector images shown in this thesis therefore are *not* electron energy spectra. In the projected image, the information on the third momentum component is missing. To obtain an energy spectrum from a VMI image, it has to be inverted, see section 3.2.5, which results in a cut through the three-dimensional distribution for $p_z = 0$. The radius on the detector can then be directly translated to the electron kinetic energy E_{kin} as

$$E_{kin} = \frac{\sqrt{p_x^2 + p_y^2}}{2m_e} = ar^2 \tag{3.10}$$

where p_x, p_y are the momentum components and m_e is the electron mass. The conversion factor a has to be determined from detector calibration, for example from an ATI spectrum, see section 3.2.6.

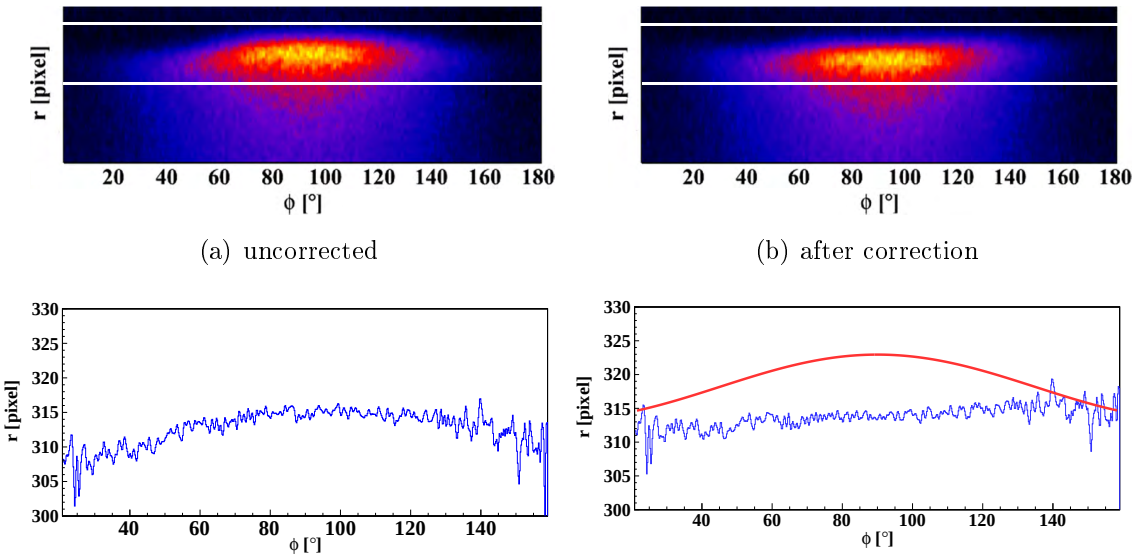

(a) uncorrected (b) after correction

(c) radial positions of maximum signal in (a) (d) radial positions of maximum signal in (b)

Figure 3.10: The rim of a projected photoelectron distribution on the detector in polar coordinates. The radial region of interest for evaluating the photoelectron angular distribution is marked by the white lines. The bottom row shows the radial positions of maximum photoelectron signal in blue and the function that is used for correcting the image in red (see text).

After converting the image to polar coordinates, it is found that the photoelectrons are not projected to a perfect circle, see Fig. 3.10(a). The radial positions of maximum intensity can be found by taking cuts of the image at each angle, and determining the radius of maximum signal by fitting the sum of a Gaussian and a constant function to the distribution. The mean of the Gaussian is taken as the radial position of maximum intensity, which is shown in Fig. 3.10(c). The resulting distribution is not flat, but at 90° the electrons are projected to larger radii as compared to smaller and larger angles. This can occur due to imperfect focusing properties of the VMI spectrometer, causing the radius to which a particle is projected to slightly depend on the angle. This interferes with the analysis of the photoelectron angular distribution in a radial region of interest, marked by the lines in Fig. 3.10(a). Less counts are taken into account for angles further away from the maximum, thus the angular distribution appears to have a narrower maximum. Moreover, inversion algorithms as described in section 3.2.5 assume perfect symmetry, thus an elliptically distorted photoline can potentially cause wrong reconstructions. Therefore, an algorithm has been implemented in order to correct for this distortion.

The distribution of radial positions in Fig. 3.10(c) is fitted by the sum of a $\cos^2$ and a constant function. This fit is used to correct the radial position of each pixel in the image. The maximum of the photoline at 45 degrees is defined as the nominal radius, and all pixels with $\phi \leq 45°$ are shifted to larger radii, whereas all pixels with $\phi > 45°$ are shifted to smaller radii. The absolute value of the shift is assumed to scale linearly with the radius, such that the pixel in the center is not moved and

pixels at larger radii are moved more strongly. The process is repeated, until the $\cos^2$ function has an amplitude of only one pixel. The resulting image is shown in Fig. 3.10(b), and the corresponding distribution of radial maxima is plotted in Fig. 3.10(d). The corrected distribution is not completely flat, but exhibits a slight slope. Reasons for this can be distortions from external magnetic fields, or small non-dipole effects in the photoionization process. Moreover, low-energy electrons can have a different center on the detector, introducing further asymmetries. VMI images are often mirrored around the symmetry axis, or only part of the image is processed for the analysis. Here, it has been investigated whether separate analysis of the four quadrants of the image produces qualitatively different results, and it has been found that the results are not identical, for example the values of the asymmetry parameter β deviate by up to 0.1. As it is not obvious why any one of the quadrants should be the "best" choice, it has been decided to use the full data set of all four quadrants for the final analysis in order to average over these effects.

3.2.5 Inversion of VMI Images

VMI images represent two-dimensional projections of three-dimensional distributions. The projection of electrons with a given kinetic energy has a sharp cut-off at $r_{max} \sim E_{kin}$, but electrons with a non-zero momentum p_z along the spectrometer axis are projected to smaller radii. The radius on the detector is thus only proportional to the p_x, p_y components of the particle momentum parallel to the detector surface, the third component is undefined. If the process that is studied has cylindrical symmetry, and the symmetry axis lies parallel to the detector surface, it is however possible to obtain a cut trough the three-dimensional distribution from the projected image analytically, provided that all electrons are captured (4π acceptance).

Different algorithms exist to perform the inversion of the image. Here the *pBasex* algorithm has been used [143], which takes advantage of the fact that the three-dimensional distribution can be described by an expansion in Legendre polynomials, see Eq. 2.8. After inverting the image, the electron energy spectrum can be obtained which is not possible from the projection. Moreover, the inversion is beneficial if electrons of different kinetic energy are present, for example from ionization of two different orbitals. In this case, the electrons from both channels overlap at smaller radii and the angular distribution of a single channel cannot be obtained.

For the molecules used in this work, only one significant photoline is observed. Additional high-energy Auger electrons and low-energy electrons from secondary processes occur, but these contribute to the image only for rather small radii. Under these conditions, an inversion provides not much additional information about the photoelectron angular distribution and bears the risk of introducing artifacts, for example from assuming a perfectly symmetric image. However, the inversion is needed for obtaining the electron spectrum and as inverted images are commonly shown for VMI data, the inverted results are also given in chapter 4 for comparison.

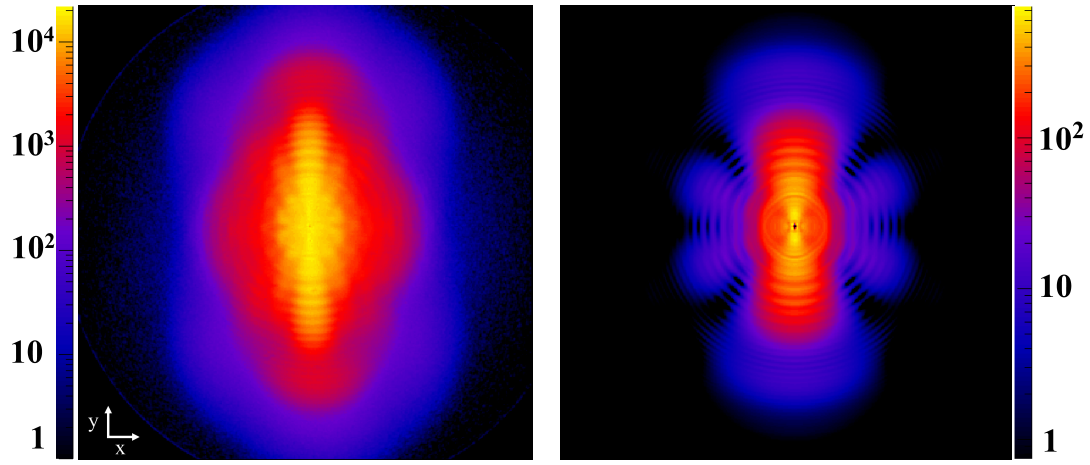

(a) raw image (b) inverted image

Figure 3.11: Raw and inverted electron detector image obtained from above-threshold ionization of argon by an 800 nm laser.

3.2.6 Energy Calibration with ATI

To obtain an electron energy spectrum from the inverted image, it is necessary to retrieve the calibration factor a in Eq. 3.10. This can be achieved by simulating the energy-dependent electron trajectories in the spectrometer, for example with SIMION, or by calibrating the detector with electrons of known kinetic energy. The latter can be done by using above-threshold ionization of a rare gas target by the TiSa laser, see also section 2.1. Here, argon was introduced into the vacuum chamber through a needle valve. The ionization energy of argon is 15.76 eV [91], and the photon energy of the TiSa laser is 1.55 eV. Thus, if one atom absorbs more than ten photons, an electron is emitted. The resulting detector image is shown in Fig. 3.11(a). A distinct ring structure can be seen and each subsequent ring corresponds to absorption of an additional photon with 1.55 eV energy. Inversion of the image, as described in the previous section, results in the electron distribution in Fig. 3.11(b) that is used for the energy calibration.

The radial projection for a narrow angular region around the intensity maximum at 90° in Fig. 3.11(b) is shown in Fig. 3.12(a). The individual peaks can be clearly identified. The calibration of radius to kinetic energy according to Eq. 3.10 can be achieved by assuming that two subsequent peaks have an energy difference of 1.55 eV. Radial positions of intensity maxima used for the calibration are marked by the red triangles. When plotting E as a function of r^2, see Fig. 3.12(b), the identified peaks lie on a straight line and fitting yields the factor $a = 2.98 \times 10^{-4}$. The first peak cannot be easily identified. Thus the absolute number of photons that have been absorbed for each of the peaks is still unknown, but with the additional input $E(r = 0) = 0$, the calibration curve in Fig. 3.12(c) can be obtained for this set of voltages. The resulting photoelectron energy spectrum for the entire image

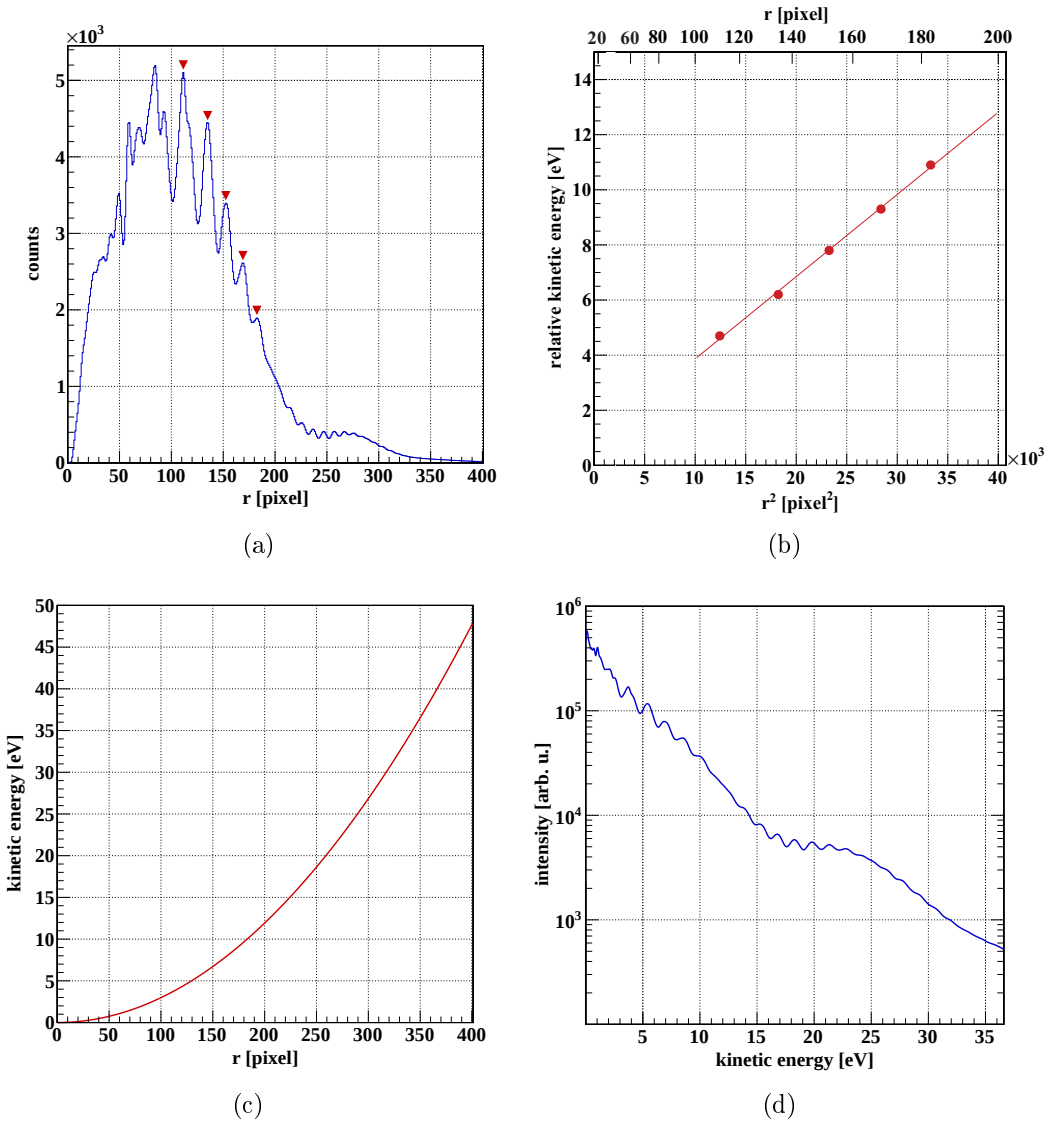

Figure 3.12: (a) Radial distribution of the photoelectrons for $80 \leq \phi \leq 100$. Identified peaks are marked by the red triangles. (b) Linear fit for determination of the factor a. (c) Calibration of the radius to kinetic energy. (d) Energy spectrum obtained from the inverted image for $0 \leq \phi \leq 360$.

is shown in Fig. 3.12(d). The number of electrons decreases strongly for higher kinetic energies, as the probability to absorb n photons is larger than to absorb $n+1$ photons. However, at kinetic energies between $\sim$17 and 25 eV, a plateau can be seen that is caused by rescattering of the electron by the ionic core [144]. The energy spacing between a peak in this region and a peak at low electron energies does not necessarily correspond to an integer number of photons, thus these peaks have been omitted for the calibration.

4 Photoelectron Angular Distributions of Fixed-in-Space Molecules

This chapter describes photoelectron angular distributions obtained from F($1s$) ionization of 1-ethynyl-4-fluorobenzene molecules (pFAB, C_8H_5F), see Fig. 4.1. In section 4.1, data are shown that were obtained from a coincidence measurement at the PETRA III synchrotron at DESY in December 2013, the remaining part of the chapter presents results of an experiment on laser-aligned molecules at the LCLS Free-Electron Laser in June 2011. Parts of the results are shown in reference [145] and [146]. Details of the image processing and conventions for detector images and polar plots of angular distributions are given in section 3.2.

4.1 Electron-Ion Coincidence Experiments

In order to test whether photoelectron angular distributions of fixed-in-space pFAB molecules can be recorded with photoelectron-photoion coincidences, an experiment was carried out at the *Variable Polarization XUV Beamline P04* [122] at PETRA III. At the time of the experiment, only circularly polarized X-rays were available at this beamline.

4.1.1 Ion-Ion Coincidences

In a coincidence experiment, the orientation of the molecule with respect to the laboratory frame can be established by recording the momentum of characteristic ionic fragments and relating it to the molecular frame, see also section 2.4. Therefore, first the fragmentation channels of the molecule following the inner-shell photoionization

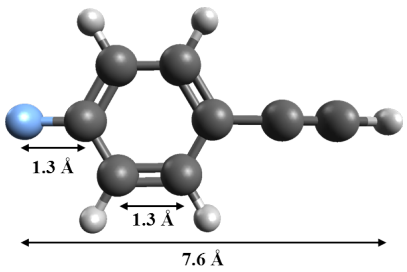

Figure 4.1: Equilibrium geometry of the 1-ethynyl-4-fluorobenzene molecule (pFAB, C_8H_5F).

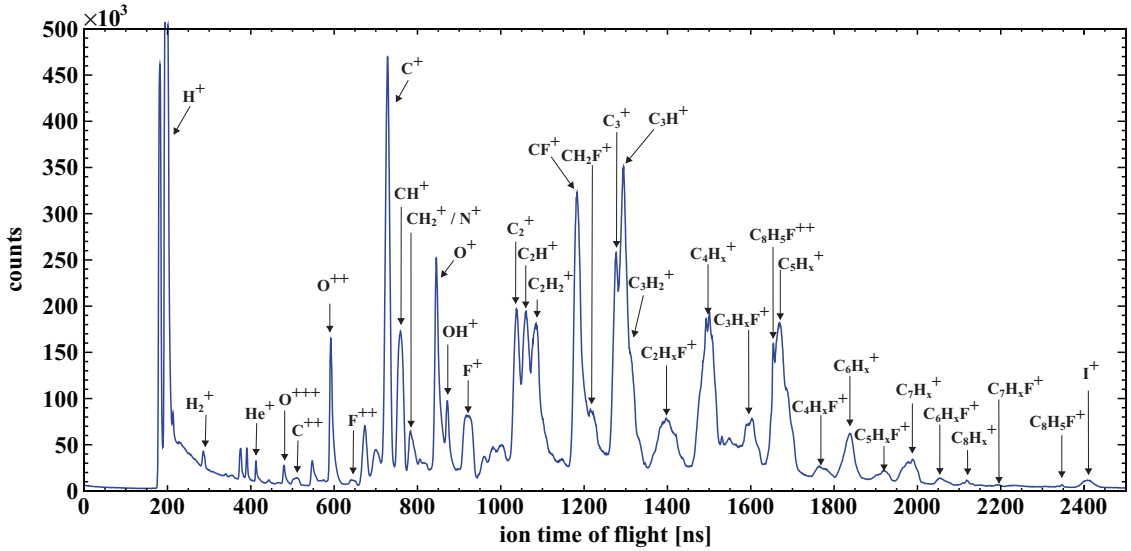

Figure 4.2: Time-of-flight spectrum of pFAB recorded under velocity map imaging conditions at PETRA with circularly polarized X-rays at a photon energy of 765 eV. For heavy fragments, the individual peaks with a mass difference of 1 amu cannot be fully resolved, thus these contributions are labeled with H_x. Contributions containing oxygen arise from ionization of residual water in the chamber and the iodine peak stems from residual CH_3I molecules in the injection system. The H^+ peak with a maximum of 3.4×10^6 has been cut for better visibility. Peaks that are not labeled correspond to electrons that are created on the grid at the end of the spectrometer drift tube on the ion side, see section 3.2.1.

are studied by recording a time-of-flight spectrum, which provides information on the resulting ionic fragments and their relative abundance. The time-of-flight spectrum of pFAB shown in Fig. 4.2 was recorded at a photon energy of 765 eV. The F($1s$) binding energy in pFAB is assumed to be identical to the binding energy in fluorobenzene, which is 692 eV [147], thus the chosen photon energy lies 73 eV above this threshold. Relevant photoionization cross sections at this photon energy are 350 kb for fluorine, 90 kb for carbon, 0.03 kb for hydrogen, and 0.9 kb for the helium carrier gas [68]. Thus, statistically, one out of three absorbed photons is absorbed by the fluorine, and the remaining two are absorbed by one of the eight carbon atoms.

Overall, the spectrum shows many different fragments, and the peak corresponding to the parent ion $C_8H_5F^+$ is very small. This is expected for inner-shell ionization, as the vacancy typically decays very fast via Auger processes, which create at least one additional charge that usually results in the fragmentation of the molecule. The F^+ and the F^{++} peaks are also comparably small, leading to the conclusion that often the fluorine remains bound to at least one carbon atom, which is supported by several $C_xH_xF^+$ peaks in the spectrum. Another possibility is that the fluorine is emitted as a neutral fragment.

A more detailed picture about the fragmentation of pFAB molecules can be obtained when considering the photoion-photoion coincidence (PIPICO) map in Fig. 4.3. The molecules often do not fragment into only two parts, as can be seen from the

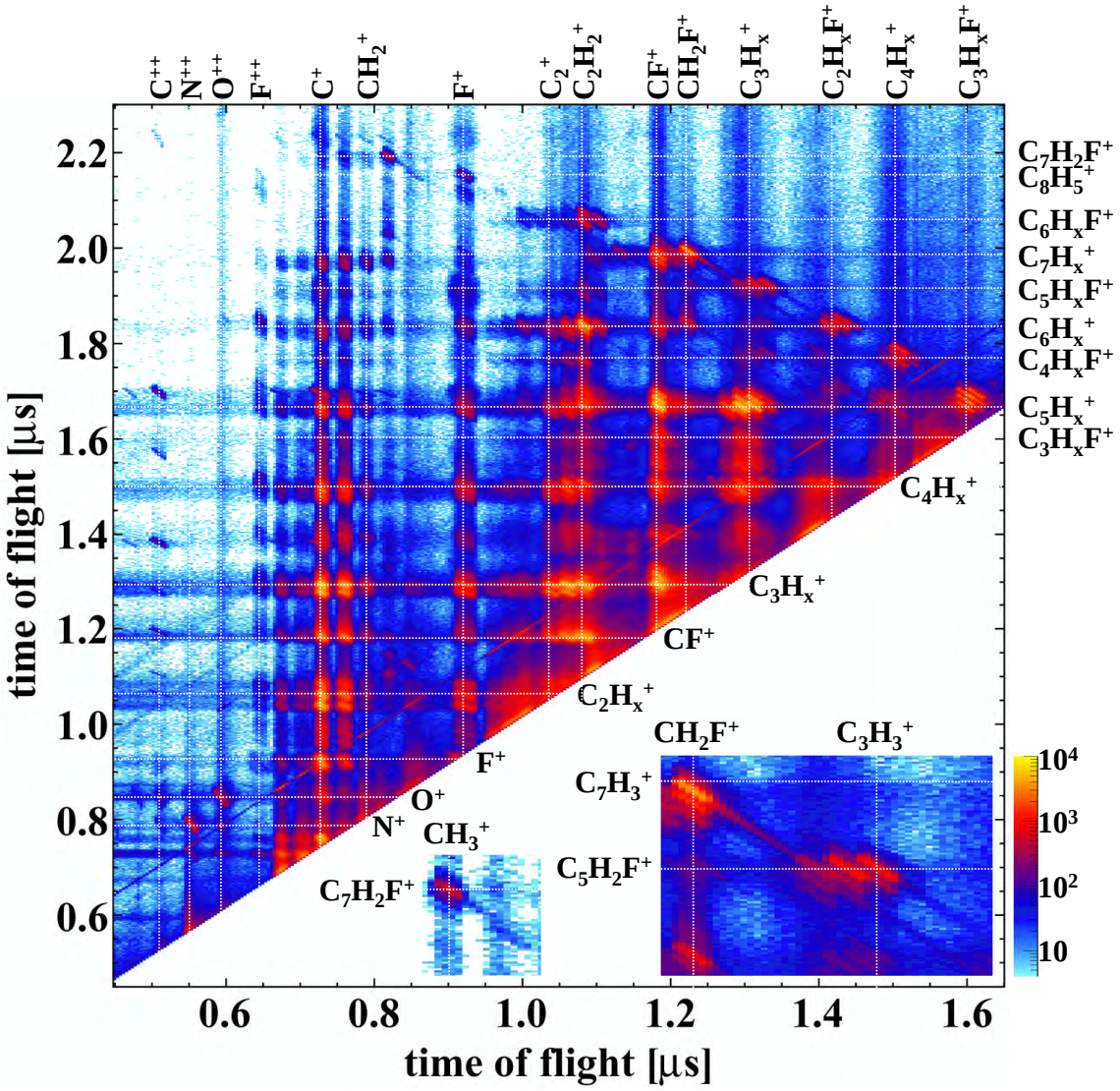

Figure 4.3: Photoion-photoion coincidence map of $C_8H_5F^+$, recorded at a photon energy of 765 eV. As the spectrometer was operated under velocity map imaging conditions, two smaller copies of each structure can be found upon close inspection. The structures are shifted to shorter flight times of both, the first and the second ion.

relatively weak population of two-body break-up channels. Even for cases where one or more hydrogens are missing to the strict two-body break-up, the lines are rather sharp, indicating that the momentum of the hydrogen does not influence the rather heavy fragments much. The most probable fragments to be detected in coincidence are $C_3H_x^+$ and $C_5H_x^+$, as well as CF^+ and $C_5H_x^+$. Coincidences between the smaller fragments $C_2H_x^+$ and $C_3H_x^+$ are also frequent, but more than two of these fragments can be created from a single molecule. In general, coincidences between fragments of roughly the same mass are more abundant than break-ups into one heavy and one light fragment.

Two particularly interesting features of the coincidence map are highlighted in the insets in Fig. 4.3. The first line corresponds to the coincidence between CH_3^+ and $C_7H_2F^+$ fragments, which is the strongest coincidence channel of the $C_7H_2F^+$ fragment. The second inset shows the coincidence between CH_2F^+ and $C_7H_3^+$ fragments. When recalling the geometry of the molecule in Fig. 4.1, it becomes clear that neither the CH_3^+ nor the CH_2F^+ fragments can be created by simple bond-breaking. In order for these fragments to occur, two hydrogens have to migrate to the CF^+ and the CH^+ fragment, respectively. Such isomerization reactions have been briefly introduced in section 1.2 for the example of acetylene. The $C_7H_3^+ + CH_2F^+$ line exhibits a pronounced tail towards longer flight times of the lighter fragment and shorter flight times of the heavier fragment that can be traced for more than 150 ns. Such a feature can occur if metastable ionic fragments are created that are accelerated by the electric field of the spectrometer before they decay into the products [148]. In this case, initially probably a doubly charged parent ion is formed. A hint of such a line can also be seen for the $C_3H_3^+ + C_5H_2F^+$ and the $CH_3^+ + C_7H_2F^+$ coincidence channels.

In order to retrieve photoelectron angular distributions of fixed-in-space molecules, the molecular frame needs to be fixed with respect to the laboratory frame. In particular, the angle between the light polarization direction and the molecular axis has to be known. In a coincidence experiment, this is achieved by assuming that the emission direction of a characteristic ionic fragment monitors the orientation of the molecule. For a diatomic molecule, this is fulfilled if the molecule dissociates fast, such that no rotation occurs before the ion has left the molecule. This is referred to as *axial recoil approximation* [149, 150]. For the case of pFAB, the straightforward fragment to choose for aligning the molecular axis is F^+. The time-of-flight spectrum in Fig. 4.2 shows however that this fragment is not detected frequently, and in the PIPICO map in Fig. 4.3 it becomes obvious that the molecule almost never breaks up into $F^+ + C_8H_5^+$. F^+ is mostly detected in coincidence with smaller fragments such as $C_2H_x^+$ and $C_3H_x^+$, and all channels involving F^+ (except for the very weak two-body break-up) exhibit rather washed-out lines, suggesting that at least three charged fragments were created. The lines of the $C_3H_x^+ + C_5H_x^+$ channel on the other hand are rather sharp, indicating that the missing fluorine atom carried no charge. Overall, only about 2% of all electrons are detected in coincidence with an F^+ ion, which considerably reduces the number of events that can be used for the determination of the photoelectron angular distribution. For a more detailed discussion on the advantages and disadvantages of coincidence measurements for recording photoelectron angular distributions see also section 6.2.2.

The PIPICO map shown here elucidates only part of the complex fragmentation pattern of the molecule, as only two charged fragments are taken into account. More information could be obtained from analyzing coincidences between three or more fragments. However, this reduces the statistics drastically and still does often not provide the complete information, as fragments that remain neutral cannot be detected.

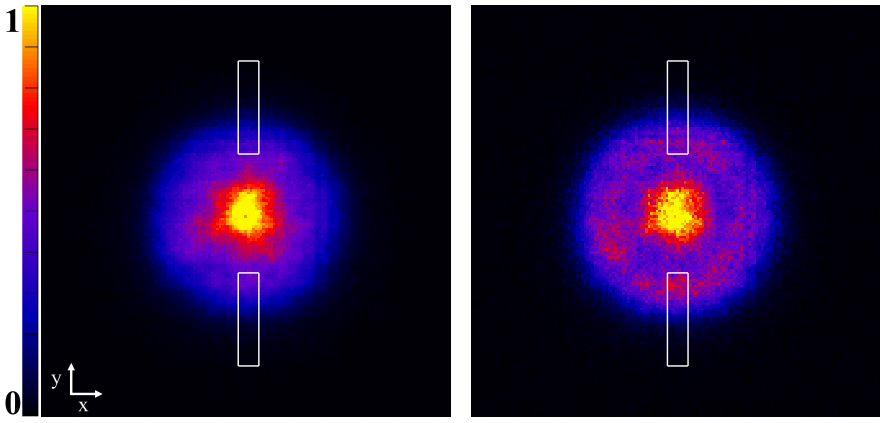

(a) 38 ns window (b) 6 ns window

Figure 4.4: Spatial distribution of ions on the detector for two different time-of-flight windows around the center of the F^+ peak. Regions of interest for the analysis of photoelectron angular distributions are marked by the white rectangles. (b) is scaled by a factor of 5 with respect to (a).

The use of delay-line-anodes allows to examine the spatial distribution of ionic fragments on the detector for any desired time-of-flight window. The spatial distribution of ions that are detected in a 38 ns window around the time-of-flight of F^+ is plotted in Fig. 4.4(a). When narrowing the window to 6 ns around the central maximum of the time-of-flight peak, only those F^+ ions that initially had (almost) zero momentum along the spectrometer axis remain, see Fig. 4.4(b). Two different contributions of ions with different kinetic energies can be identified, a ring at larger radii and a contribution in the center of the detector. These plots can be exploited to analyze only those events for which the F^+ is emitted parallel to the X-ray polarization direction, along the y-axis, by defining an additional condition in the (x, y) coordinates that is illustrated by the white rectangles in Fig. 4.4. Ideally, only those events for which an F^+ ion is detected in coincidence with a $C_8H_5^+$ ion would be used, but this reduces the statistics for the electron analysis too drastically. The non-linear pFAB molecule is still free to rotate about the F-C axis as long as only one fragment is used to define the molecular frame, corresponding to the case of one-dimensional orientation as defined in section 2.4.

4.1.2 Photoelectron Angular Distributions

In coincidence with the ionic fragments, electrons are recorded on the opposite side of the VMI spectrometer. The three-dimensional electron momentum cannot be retrieved in this case, as the total flight time of an electron in the spectrometer is only a few nanoseconds. However, a window is defined around one peak in the electron time-of-flight spectrum that corresponds to photoelectrons created by the X-ray pulse, thus reducing background signals in the image.

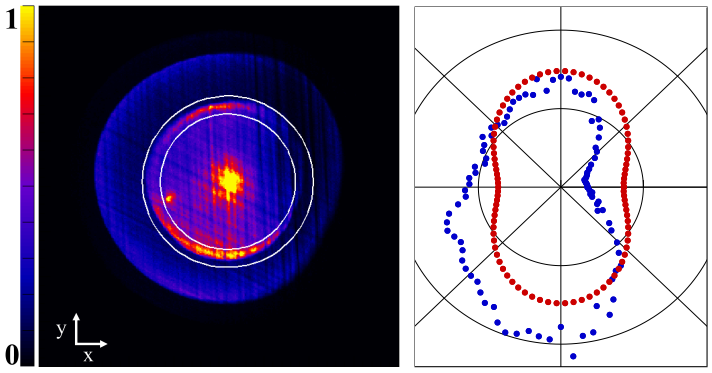

(a) (b)

Figure 4.5: (a) Image on the electron detector for ionization of argon at a photon energy of 321 eV, resulting in photoelectrons of 73 eV and Auger electrons of 235 eV kinetic energy. Only electrons detected in coincidence with Ar^{++} are selected. The rim of the projected photoline is marked by the white circles. (b) Calibration of the photoelectron angular distribution obtained from (a). Blue: raw data, red: corrected data. Each ring corresponds to 25×10^3 counts. Statistical errors are smaller than the data points.

To remove detector inhomogeneities before analyzing the photoelectron angular distribution, a calibration is needed. This can be achieved with the help of argon photoelectrons, whose angular distribution is well-known. An electron detector image for ionization of argon at a photon energy of 321 eV is shown in Fig. 4.5(a). Here, only electrons that are detected in coincidence with an Ar^{++} ion are selected. At this energy, predominantly the $Ar(2p_{3/2})$ level is ionized, resulting in photoelectrons of 73 eV kinetic energy. The rim of this projected photoline is marked by the white circles; the region of interest defines an azimuthal opening angle of 37°. The second electron line that is visible at larger radii corresponds to the argon Auger electrons with a kinetic energy of about 235 eV. The detector image contains artificial lines that are caused by individual windings of the delay-line anode. Moreover, very inhomogeneous detection efficiencies and a distortion of the circular shape of the photoline are visible[1]. The low efficiency on the right hand side is probably caused by improper settings of the constant fraction discriminator. The photoelectron angular distribution can be obtained from the radial region of interest in Fig. 4.5(a) as described in section 3.2, the result is plotted in Fig. 4.5(b) as blue dots. At a kinetic energy of 73 eV, the asymmetry parameter of argon is $\beta_{\mathrm{circ}} = -\frac{1}{2}\,\beta = 0.48$ [151]. A calibration curve can be defined which scales the value of each angular bin such that the correct angular distribution results that is shown as red dots. The same calibration function can be applied to all photoelectron angular distributions measured at the same kinetic energy and for the same spectrometer voltages.

The electron detector image for ionization of pFAB molecules at a photon energy of 765 eV is shown in Fig. 4.6(a). Only electrons that are measured in coincidence with

[1] Due to a short circuit in one of the wires of the hexagonal delay-line anode, only two of the three layers on the electron side could be used.

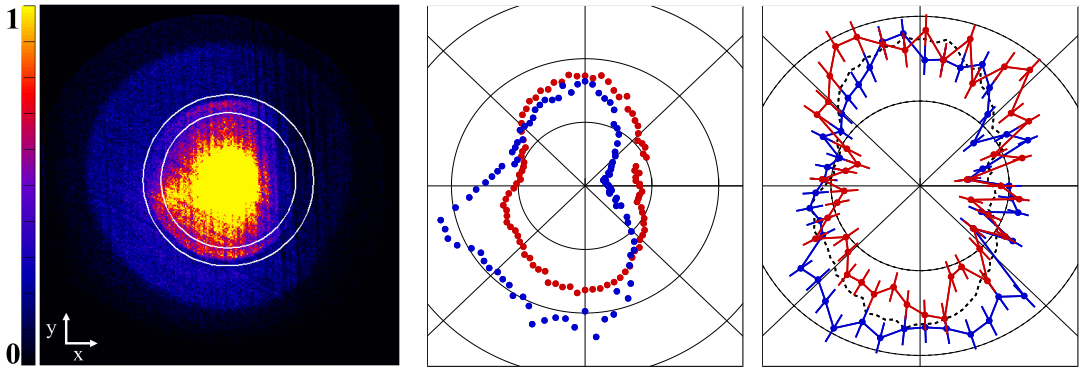

(a) (b) (c)

Figure 4.6: (a) Image on the electron detector for ionization of pFAB at a photon energy of 765 eV, resulting in photoelectrons of 73 eV and C($1s$) Auger electrons of ∼280 eV kinetic energy. Only electrons detected in coincidence with F^+ are selected. The rim of the projected photoline is marked by the white circles. The region of interest defines an azimuthal opening angle of 37°. (b) Raw electron angular distribution (blue) as obtained from (a) and the corrected curve (red). Each ring corresponds to 10^3 counts. Statistical errors are small as compared to the systematic errors. (c) Angular distributions of electrons recorded in coincidence with F^+ ions that are detected in the upper rectangle (blue) and the lower rectangle (red) in Fig. 4.4(a). Each ring corresponds to 50 counts. The distribution for randomly oriented molecules from (b) is shown as a dashed black line, scaled by a factor of 0.05.

an F^+ are selected. The F($1s$) photoelectrons have a kinetic energy of 73 eV. The second signal at larger radii corresponds to the C($1s$) Auger electrons with a kinetic energy of ∼ 280 eV. The systematic artifacts in the electron angular distribution resulting from inhomogeneous detector efficiencies can be removed from the raw angular distribution by applying the bin-by-bin scaling obtained from the argon calibration. The raw as well as the corrected angular distribution are shown in Fig. 4.6(b). The correction works reliably, except for the fact that the artificial intensity maximum in the lower left quadrant was not completely removed.

In order to obtain the angular distribution of fixed-in-space molecules, only those events are selected for which an F^+ ion is detected in one of the two rectangles in Fig. 4.4(a).[2] These define a polar opening angle of ±5° in the (x, y) plane, and an azimuthal opening angle of ±36° for the emission direction of the F^+ ion. About 2.5% of the electrons in Fig. 4.6(a) are recorded in coincidence with one of these F^+ ions, and as only 2% of the electrons are detected in coincidence with a F^+, only 0.05% of all ionization events can be used for this purpose. A possibility to exploit all events is to expand the photoelectron angular distribution in the molecular frame in *F-functions* [152–154]. However, this requires knowledge of all three momentum components of the photoelectron which cannot be determined well in the current VMI set-up.

[2] The additional narrow time-of-flight window as shown in Fig. 4.4(b) reduces the statistics significantly and did not improve the results. It is thus omitted.

The resulting angular distribution of photoelectrons recorded in coincidence with F^+ ions in the two opposite rectangles are plotted in Fig. 4.6(c). The distribution for randomly oriented molecules is shown for comparison. The angular distribution becomes slightly more pointed in one direction and broader in the other direction, thus a certain relation of to the emission direction of the F^+ ion exists, but the structures are rather broad. One reason for this might be that the fluorine atom is not emitted strictly along the F-C bond direction, as was indicated by the broad coincidence lines involving F^+ in the PIPICO map. For a more detailed discussion, refer to section 6.2.

4.2 Laser-Aligned Molecules

An alternative approach to fix the molecular frame with respect to the laboratory frame is to actively align a whole ensemble of molecules by using a strong laser pulse. This is advantageous for an experiment at the short-pulsed LCLS Free-Electron Laser that has a repetition rate of only 120 Hz, as in this way many molecules can be ionized in every X-ray pulse.

The time-of-flight spectrum of pFAB, obtained at a photon energy of 743 eV at the LCLS is plotted in Fig. 4.7.[3] The spectrum that was recorded at a photon energy of 765 eV at PETRA is also shown for comparison. Several ten eV above all ionization thresholds, the fragmentation is assumed to be rather insensitive to the exact photon energy. Overall, the two spectra are rather similar, demonstrating that multi-photon processes are only minor contributions to the overall fragmentation. The most noticeable difference is the large He^+ peak in the LCLS spectrum (the maximum of 4.8×10^6 has been cut for better visibility), that is nearly absent in the PETRA spectrum. This is due to the fact that at PETRA helium carrier gas at a relatively low pressure of a few hundred millibars was used for the continuous molecular beam, whereas at the LCLS the pulsed beam was operated with 50 bar of helium, see also section 3.1.2. A second difference is observed in the large parent ion peak that is present in the LCLS spectrum, but is very small in the PETRA spectrum. The fact that this peak is rather broad indicates that the parent ions are produced with substantial kinetic energy. In molecular fragmentation, kinetic energy stems from Coulomb repulsion between two (or more) charged fragments, thus the broad $C_8H_5F^+$ peak suggests that clusters of pFAB molecules were produced in the molecular beam. This is confirmed by the peak corresponding to the singly charged pFAB dimer that is shown in the inset. This peak is also not narrow, showing that the dimers are probably created from the break-up of larger clusters. The presence of molecular clusters in the beam is of particular importance for the analysis of photoelectron distributions of aligned molecules, since the molecules that are bound

[3] The high number of ions detected per shot at the LCLS did not allow to use a software constant fraction discriminator on the MCP trace to identify individual ion hits, thus the averaged MCP signal is shown which exhibits a slightly rising baseline towards longer flight times.

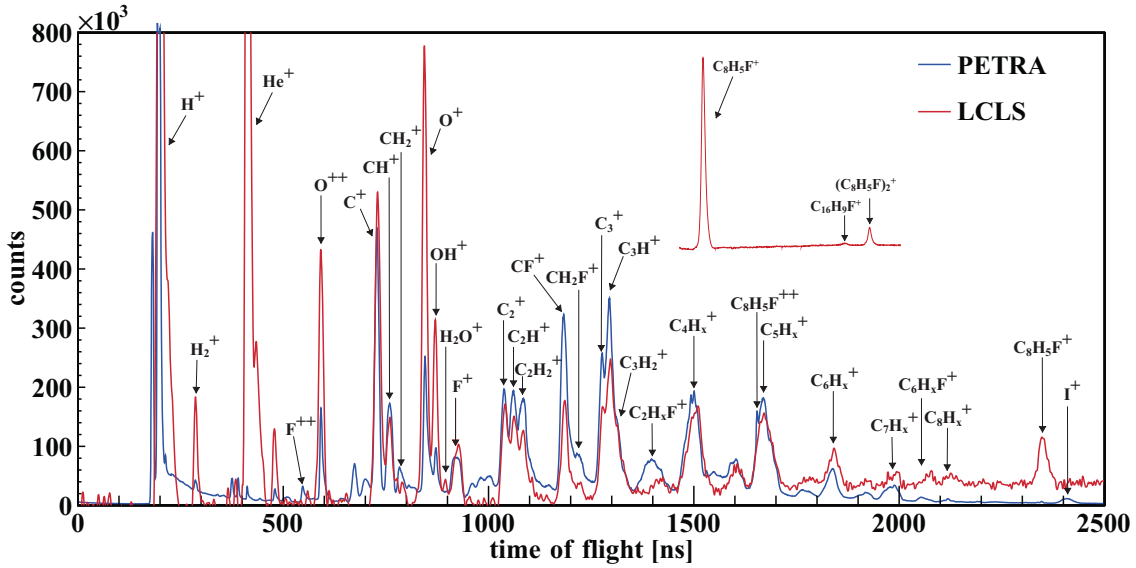

Figure 4.7: Time-of-flight spectrum of pFAB recorded at a photon energy of 743 eV at the LCLS (without alignment laser). The spectrum from Fig. 4.2 recorded at PETRA is also shown for comparison. The LCLS spectrum has been scaled and shifted such as to provide direct comparability with the PETRA data.

in clusters are, most likely, not aligned by the YAG alignment laser. Consequently, they can produce a background of unaligned molecules. The recorded ion data does not provide an unambiguous way of determining how many clusters were created, but as this is of importance for the electron analysis, it has been attempted to estimate a lower limit based on hints in the available data, see appendix A.1 for details.

After recording the time-of-flight spectrum, the MCP was gated to record only ions that arrive in a time window of 168 ns around the F^+ peak. For the spectrometer voltages that were used in velocity map imaging, the F^+ peak (19 amu) could not be fully separated from the H_2O^+ peak (18 amu), as can be seen in the time-of-flight spectrum in Fig. 4.17, thus ionized water molecules are also visible. Figure 4.8(a) shows the ion detector image that is recorded when the molecular beam is turned off. The line that is visible corresponds to ionization of residual water along the X-ray beam. In principle, all ions should be focused to the center in VMI, but the focusing does not work properly for ions that are created very far away from the spectrometer center. When the molecular beam is turned on, the distribution in Fig. 4.8(b) results; F^+ ions with an isotropic spatial distribution can be seen. They have a small offset along y with respect to the ionized residual water, caused by the momentum of the supersonic molecular beam that propagates along y. The signal from residual water dominates the image, however, as the background was continuously recorded at a repetition rate of 60 Hz, it can be subtracted well, resulting in the image in Fig. 4.8(c). The remaining sharp dot in the center of Fig. 4.8(c) stems from water molecules in the molecular beam.

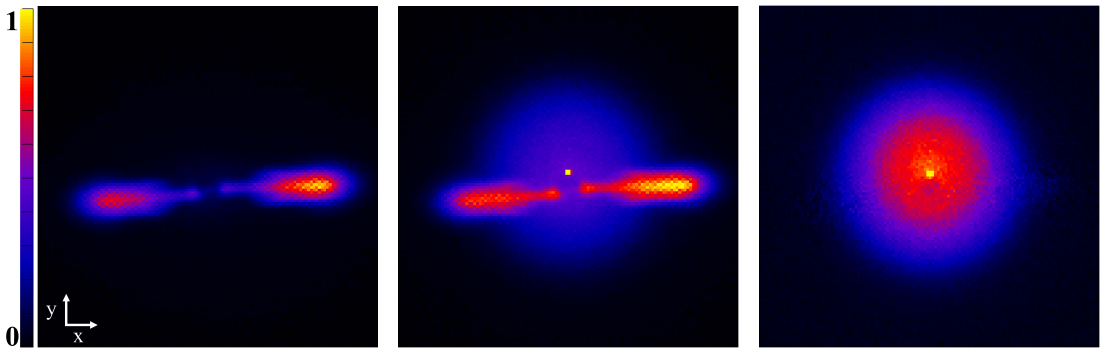

(a) FEL, no target (b) FEL, pFAB (c) 4.8(b) minus 4.8(a)

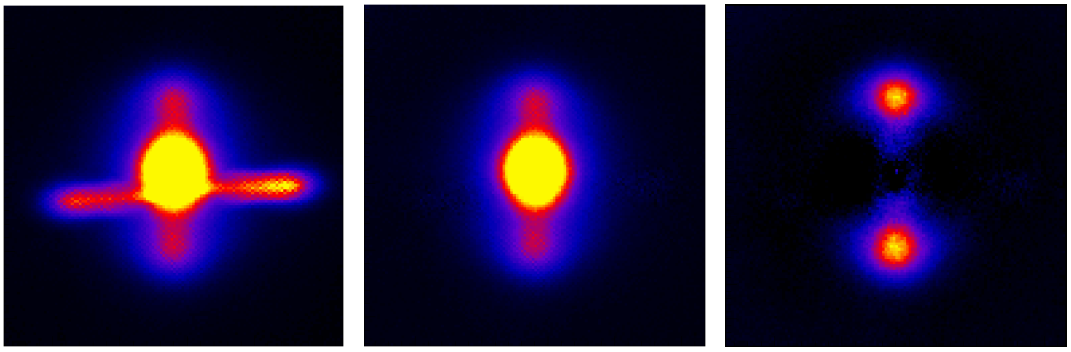

(d) FEL, YAG, pFAB (e) 4.8(d) minus 4.8(a) (f) 4.8(e) minus fit (see text)

Figure 4.8: Images on the ion detector for a gate around the time-of-flight peak of F^+; the X-ray energy is 723 eV. Ionization of residual gas creates a background (a) that needs to be subtracted from the images recorded for ionization of pFAB molecules without (b) and with (d) the YAG alignment laser. The subtracted images are shown in (c) and (e), the contribution of isotropically distributed F^+ ions in (e) is subtracted by fitting a two-dimensional Lorentz function resulting in (f). The polarization directions of the FEL and the YAG laser lie along y. (d) and (f) are scaled by a factor of 2 with respect to (e).

When the YAG alignment laser is added, the distribution in Fig. 4.8(d) arises, the image after background subtraction is shown in Fig. 4.8(e). Partly, the fluorine ions are emitted along the polarization direction of the YAG alignment laser, but an additional strong ion signal arises in the center of Fig. 4.8(e) that is isotropically distributed and has a smaller radius. This feature is ascribed to F^+ ions created from pFAB clusters or cluster fragments that can be ionized or dissociated by the YAG pulse after inner-shell ionization from the X-ray pulse. For a more detailed explanation refer to Fig. A.1 in appendix A.1 and section 4.4. This isotropic signal overlaps with the F^+ ions emitted from aligned pFAB molecules, making it unfeasible to determine the degree of molecular alignment from this image. The distribution in the center was thus fitted by a two-dimensional Lorentz distribution and then subtracted from the image. The resulting distribution of F^+ ions from aligned molecules is shown in Fig. 4.8(f).

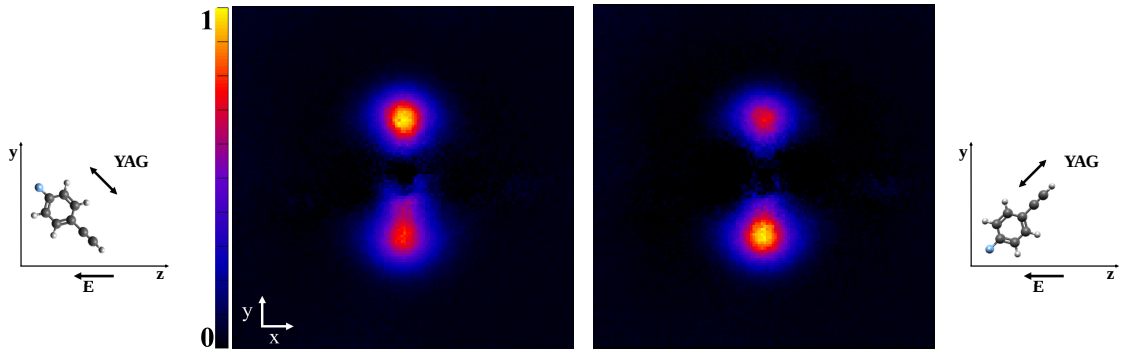

(a) YAG rotated by +45° (b) YAG rotated by -45°

Figure 4.9: Detector images obtained from ionization of pFAB molecules of two different orientations by X-rays with a photon energy of 743 eV. The YAG polarization is rotated out of the (x, y) plane. Isotropic background has been subtracted by a two-dimensional Lorentz fit (see text).

When comparing Figs. 4.8(c) and 4.8(f), it can be concluded that the linearly polarized YAG laser pulse aligns the F-C axis of pFAB along its polarization direction, and that the F^+ ions can be used to monitor the alignment of the F-C axis. The achieved degree of molecular alignment can be quantified by the ensemble-averaged expectation value of $\cos^2\theta_{2D}$, where θ_{2D} is the angle between the projection of the F^+ ion momentum vector on the detector plane and the YAG laser polarization direction. It can be calculated from the image in Fig. 4.8(f) as

$$\langle\cos^2\theta_{2D}\rangle = \frac{\sum_{i,j} I(R_i, \theta_{2D,j})\ \cos^2\theta_{2D,j}}{\sum_{i,j} I(R_i, \theta_{2D,j})}, \tag{4.1}$$

where I are the counts at the radius R_i, measured from the center of the distribution, and at the angle $\theta_{2D,j}$. This results in $\langle\cos^2\theta_{2D}\rangle = 0.89$; as discussed in section 6.2 this is one of the limiting factors for the recorded photoelectron angular distributions.

In order to explore, whether orientation of pFAB molecules can be achieved by the combined static electric extraction field $\vec{E}$ of the spectrometer and the laser-alignment field, the latter has to have a component along $\vec{E}$, as was described in section 2.4. Rotation of the polarization by ±45° yields such a component and, at the same time, allows to observe the result in the (x, y) detector plane. Since the dipole moment of pFAB is directed along the F-C axis, pointing from the fluorine to the benzene, the fluorine atom preferentially points away from the ion detector. Figures 4.9(a) and 4.9(b) show the resulting F^+ ion distributions when the polarization direction of the YAG laser is turned by +45° or -45° with respect to the (x, y) plane. The F^+ ion images show a clear asymmetry. The molecular orientation can be quantified by the ratio

$$\Delta N = \frac{N(F^+_{up})}{N(F^+)}, \tag{4.2}$$

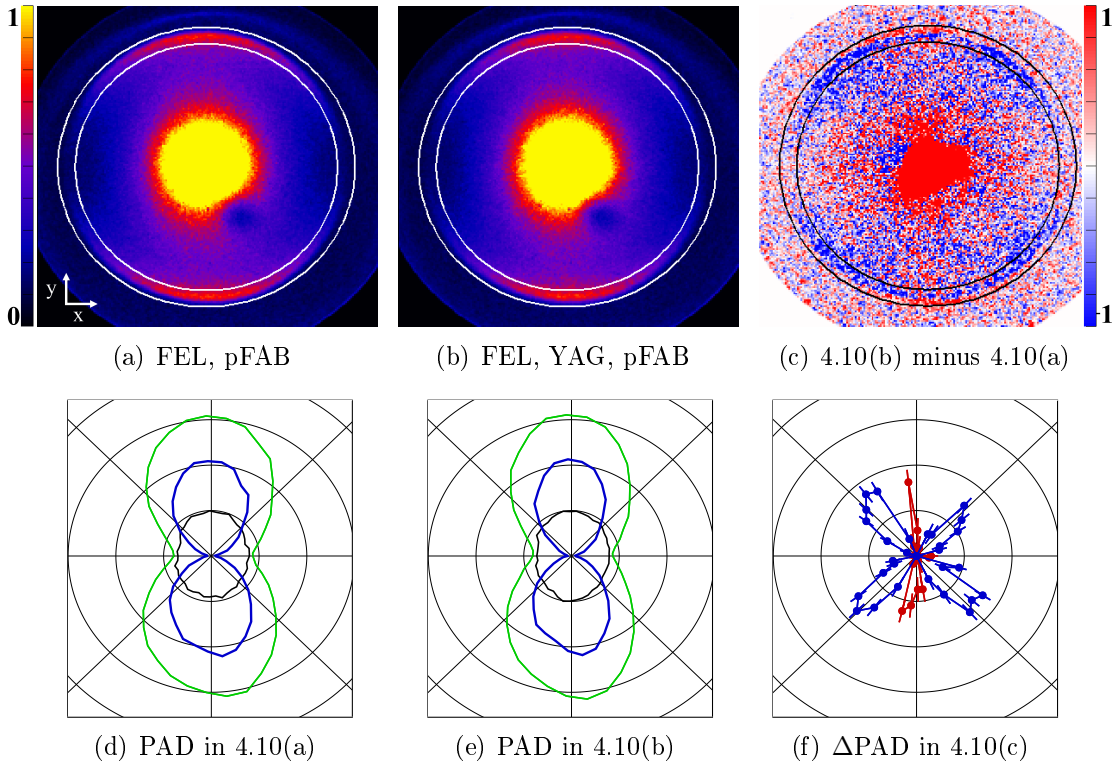

(a) FEL, pFAB (b) FEL, YAG, pFAB (c) 4.10(b) minus 4.10(a)

(d) PAD in 4.10(a) (e) PAD in 4.10(b) (f) ΔPAD in 4.10(c)

Figure 4.10: Electron detector image recorded for ionization of pFAB molecules by the LCLS at a photon energy of 743 eV, without (a) and with (b) the YAG alignment laser. The photon energy has been filtered to ±2 eV and the background from ionization of residual gas has been subtracted. The polarization directions of FEL and YAG lie along y. The rim of the projected F(1s) photoline with a kinetic energy of 51 eV is marked by the white circles. The difference image in (c) is scaled with respect to (a) and (b) by a factor of 17, no background has been subtracted. The photoelectron angular distributions in (a) and (b) are shown in (d) and (e). Green: as obtained from the indicated region of interest. Black: background at larger radii. Blue: PAD with subtracted background. Each ring corresponds to 10^4 counts. The difference angular distribution obtained from (c) is plotted in (f) Blue: negative difference. Red: positive difference. Each ring corresponds to 2% difference.

where $N(F^+)$ is the integral of the whole detector image and $N(F^+_{up})$ is the integral in the upper half [155]. This results in $\Delta N = 0.61$ and $\Delta N = 0.39$ for Figs. 4.9(a) and 4.9(b), respectively.

4.3 Photoelectron Angular Distributions

Simultaneously to the ions, electrons are imaged on the opposite side of the velocity map imaging spectrometer. Figure 4.10(a) shows the electron detector image recorded for ionization of pFAB molecules by the LCLS at a photon energy of 743 eV. The rim of the projected F(1s) photoline with a kinetic energy of 51 eV is marked by the white circles. It shows a pronounced angular anisotropy that is expected for

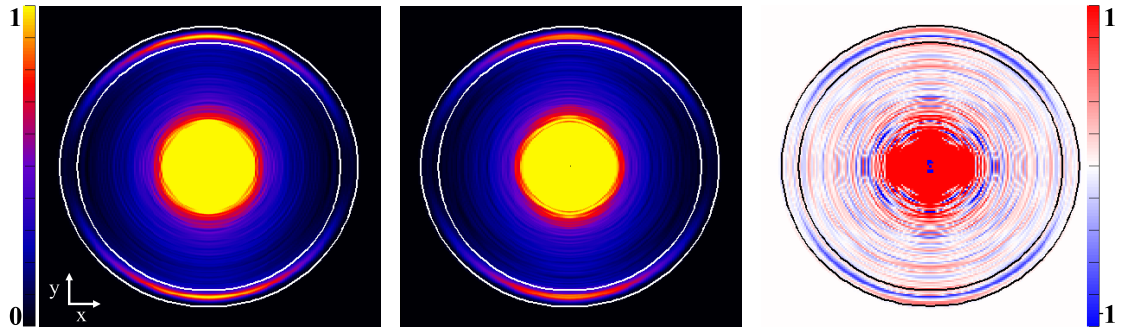

(a) inversion of 4.10(a) (b) inversion of 4.10(b) (c) 4.11(b) minus 4.11(a)

Figure 4.11: Inversion of the electron detector images in Fig. 4.10, obtained by applying the *pBasex* algorithm [143]. (c) is scaled with respect to (a) and (b) by a factor of 17.

single-photon ionization of an *s*-orbital. A second, strong electron signal is observed in the center of the image, corresponding to electrons with lower kinetic energies. These electrons are most likely created by multi-electron processes such as Auger cascades, shake-up or shake-off, see section 2.1, or by inelastic scattering of photoelectrons or Auger electrons inside the molecule. The low energy electrons are however to a good degree separated from the rim of the photoline, such that they should not significantly influence the angular distribution in the region of interest. The 'hole' in the lower right quadrant corresponds to an insensitive area on the phosphor screen that had previously been damaged by too intense signal. High-energy electrons created from C(1*s*) and valence ionization, as well as fluorine and carbon KLL-Auger electrons have kinetic energies of $> 240\,\mathrm{eV}$, and are thus collected only in a small solid angle around the emission direction towards or away from the detector for the chosen spectrometer voltages, contributing a small, almost flat background. The electron detector image that is recorded when the YAG alignment laser is added is plotted in Fig. 4.10(b). At first sight, very little structure can be seen and the difference to the image recorded without the YAG laser is not obvious.

The corresponding photoelectron angular distributions (PADs) in the radial regions of interest are shown in green in the bottom row of Fig. 4.10. In order to account for the background of high-energy electrons, a narrow radial region of interest directly outside of the photoline is evaluated and then subtracted from the raw PAD. The resulting photoelectron angular distributions are shown in blue. Upon close inspection it can be seen that the PAD that is recorded with the YAG laser is a little narrower than the one obtained without the alignment laser. To visualize the difference between data recorded with and without the YAG laser, the alternately recorded images are normalized according to the respective number of events and subtracted. The resulting difference image is shown in Fig. 4.10(c), the corresponding difference photoelectron angular distribution (ΔPAD) is plotted in Fig. 4.10(f). Here, the angular rearrangement of photoelectrons can be clearly seen. An increase of photoelectron intensity along the YAG polarization direction and a decrease at

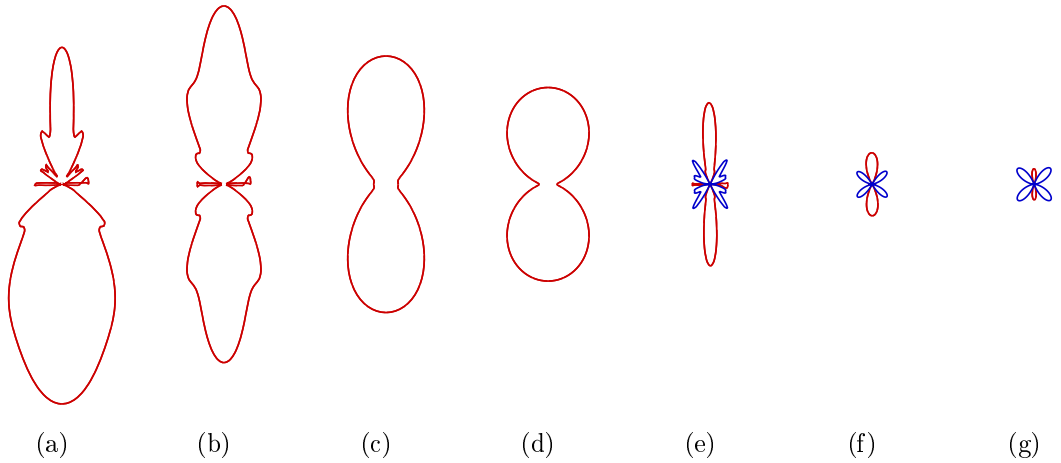

Figure 4.12: Photoelectron angular distributions of pFAB at an electron energy of 50 eV, calculated from density functional theory. (a) perfect one-dimensional orientation. (b) perfect one-dimensional alignment. (c) folding (b) with the experimental degree of alignment ($\sigma = 20°$). (d) random orientation ($\beta = 1.55$). (e) perfect alignment minus random orientation. Blue contributions denote negative signal. (f) experimentally achieved alignment minus random orientation. (g) as (f) but including molecular clusters as well as experimentally determined ionization probabilities, see text. (g) is scaled by a factor of 10 with respect to (f), all other distributions are plotted on the same absolute scale. The integral of (a) to (d) is identical, the integral in (e) to (g) is zero.

larger angles is detected, corresponding to a narrower photoelectron angular distribution for the data recorded with the YAG laser. Moreover, a large difference signal is found in the center of Fig. 4.10(c) that can be attributed to additional low-energy electrons that are created by the YAG. This aspect is discussed in section 4.4.

Inversions of the electron detector images in Fig. 4.10 are shown in Fig 4.11, obtained with the pBasex algorithm [143]. A cut through the three-dimensional distribution can be retrieved if cylindrical symmetry is given, which is the case for one-dimensionally aligned molecules with the axis of alignment parallel to the detector plane. Artifacts due to the fitting of radial basis functions arise in the form of sharp ring structures, but apart from this the resulting two-dimensional cuts look similar to the raw detector images.

The magnitude of the effect that is visible in the difference photoelectron angular distribution in Fig. 4.10(f) corresponds to maximum ±4% of the intensity in the photoelectron angular distribution in Fig. 4.10(e). One reason for this could be the imperfect experimental molecular alignment, which averages out possible interference structure of the photoelectron angular distribution in the molecular frame. The degree of alignment can be well characterized from the ion image in Fig 4.8(f), and results in $\langle \cos^2\theta_{2D} \rangle = 0.89$, averaging over the molecular axes distribution with a width of $\sigma = 20°$. To illustrate the influence of the degree of alignment on the photoelectron angular distribution, Fig. 4.12 shows distributions for different molecular alignment, calculated with density functional theory (DFT). The angular distribution that is expected for a perfectly, one-dimensionally oriented pFAB molecule is

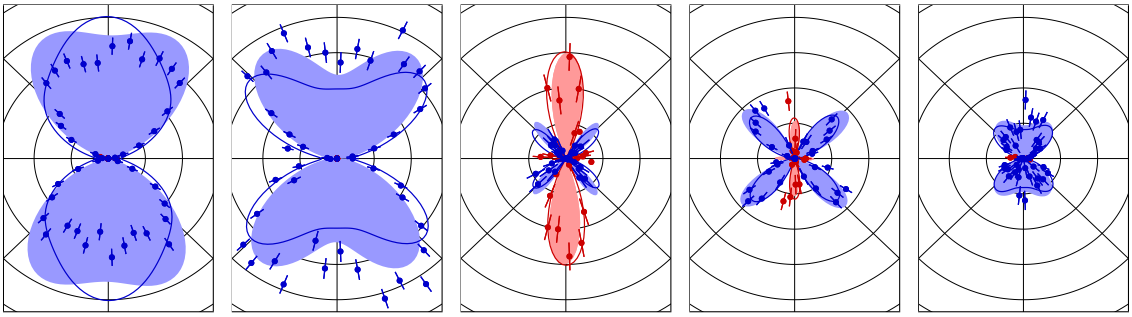

(a) 31 eV (b) 36 eV (c) 46 eV (d) 51 eV (e) 62 eV

Figure 4.13: Photoelectron angular distribution differences of pFAB for different photoelectron kinetic energies. Raw data are shown as dots, inverted data as shaded areas and calculated ΔPADs, shifted by +10 eV (see text), as lines. Blue: negative difference. Red: positive difference. All distributions are plotted on the same radial axis, each ring corresponds to 2% difference.

plotted in Fig. 4.12(a), the up-down symmetrized distribution that results for perfect one-dimensional alignment is shown in Fig. 4.12(b). The experimentally achieved degree of molecular alignment can be accounted for in the calculations by averaging over a two-dimensional Gaussian, resulting in the PAD in Fig. 4.12(c). The angular structure is completely washed out. However, when comparing the distributions in Fig. 4.12(c) and the calculated distribution for randomly oriented molecules in Fig. 4.12(d) to the experimentally obtained PADs in Figs. 4.10(d) and 4.10(e), it becomes clear that the difference in the experiment is much smaller than expected, even when accounting for the experimental degree of molecular alignment.

A second reason for the small observed difference in the experiment can be the significant amount of signal from clusters in the molecular beam, which are most likely not aligned by the YAG laser. They contribute photoelectrons originating from ionization of an unknown amount of randomly aligned pFAB molecules to the data that is recorded with the alignment laser, which can significantly decrease the magnitude of the effect in the difference angular distribution. Moreover, the ionization probabilities of aligned and randomly oriented molecules are different, as discussed below. Therefore, even the shape of the difference photoelectron angular distribution can change when randomly oriented molecules are assumed to contribute to the image recorded with the YAG laser. A more detailed description and calculated distributions for a variable amount of molecular clusters is given in Fig. A.3 and appendix A.1. Figure 4.12(g) shows the modeled ΔPAD that results when assuming that 90% of the ionized molecules in the data recorded with the YAG laser were actually randomly oriented, and when the difference in ionization cross sections is taken into account. The distribution is scaled by a factor of 10 with respect to Figure 4.12(f). The shape of the experimental ΔPAD in Fig. 4.10(f) is reproduced.

The dependence of the difference angular distribution on the photoelectron kinetic energy has been investigated by varying the photon energy. The corresponding results obtained from raw, and inverted detector images for five different electron

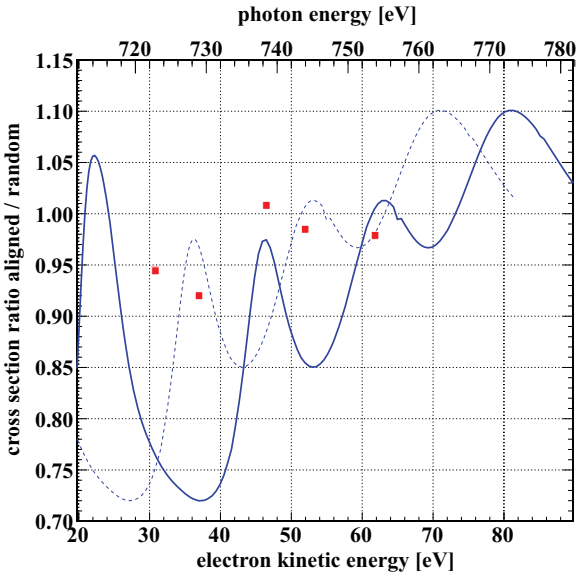

Figure 4.14: Cross section ratio between aligned and randomly oriented molecules as a function of energy. Blue: calculated from DFT. Full line: as calculated. Dashed line: shifted by +10 eV to account for the energy offset between calculations and experimental data. Red: experimental data points as obtained from Eq. 4.3. Statistical errors are smaller than the data points.

energies between 31 eV and 62 eV are shown in Fig. 4.13. Except for the case of 31 eV kinetic energy[4], the distributions of the raw (dots) and the inverted (shaded areas) data agree well within the statistical uncertainties, confirming that, in general, for these experimental conditions the PAD obtained from a narrow radial region of interest in the raw, projected detector image is a good approximation. Pronounced angular structures are visible which vary strongly as a function of electron energy.

A prominent change is found in the integrated difference, which is positive for 46 eV but negative for all other photoelectron energies. A non-zero integral could be explained by a difference in the partial photoionization cross sections for molecules aligned parallel to the X-ray polarization direction as compared to randomly oriented molecules. Figure 4.14 shows the calculated ratio between the partial ionization cross section for molecules that are perfectly aligned with the molecular axis parallel to the X-ray polarization direction, and the total ionization cross section. For the individual cross sections, see Fig. A.2. The ratio varies from 0.7 to 1.1 within an energy range of only 50 eV, which stands in contrast with the fact that the photoionization cross section is often assumed to be rather independent of the angle between the molecular axis and the light polarization for inner-shell ionization far above the threshold. Also shown are the experimental ratios

$$\varrho = \frac{I_{\text{YAG on}}}{I_{\text{YAG off}}}, \tag{4.3}$$

[4] For this lowest energy, the photoelectrons are least separated from the contribution of low-energy electrons, which may introduce artifacts in the inversion.

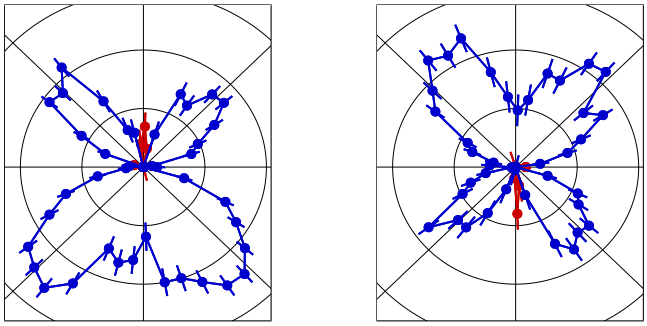

(a) YAG rotated by +45°

(b) YAG rotated by -45°

Figure 4.15: ΔPADs for oriented pFAB molecules recorded at an electron energy of 51 eV. Blue: negative difference. Red: positive difference. Each ring corresponds to 2% difference. The YAG polarization is rotated out of the (x, y) plane by $\pm 45°$. The data sets are the same as for the ion images in Fig. 4.9.

where I denotes the integrated number of counts in the radial region of interest that is considered for the photoelectron distribution. In the experiment, the molecules are not perfectly aligned, and molecules in clusters are randomly oriented. Thus, the ratio varies less strongly as compared to the calculation, but the trend as a function of photoelectron energy is reproduced, except for the data point at 62 eV. Based on this comparison, the calculated energies have been shifted to higher energies by 10 eV, see Fig. 4.14. This is motivated by the fact that the LB94 exchange correlation potential that was used in the DFT calculations is known to be too attractive, causing a shift of the calculated cross sections to lower binding energies [97, 156].

The second contribution to the change in the ΔPADs arises from the energy-dependent interference structure in the photoelectron angular distribution. Much of the structure is washed out due to the rotational averaging, as was seen in Fig. 4.12, but a small effect remains. Overall, the dominant feature that is visible for all energies in Fig. 4.13 is a stronger confinement of the electron emission towards the direction of the nearest-neighbor atom, which is situated along the aligned molecular axis. This is commonly referred to as the 'forward scattering peak' in photoelectron diffraction [53, 54, 157].

To establish the connection between the shape of the ΔPADs and the molecular structure beyond these qualitative arguments, ΔPADs obtained from density functional theory calculations are also shown as lines in Fig. 4.13. They are calculated by subtracting the photoelectron angular distributions for aligned and randomly oriented molecules after normalizing them to the respective integrated number of counts in the experimental data. The calculated 'YAG-on' distribution is assumed to be a sum of the calculated PAD for the experimentally achieved degree of alignment and a variable contribution of the PAD for randomly oriented molecules, for details see appendix A.1. The resulting calculated distributions agree well with the data within the statistical error bars, for all energies except 31 eV.

The link of the ΔPAD to the molecular geometry can be seen even more clearly when the molecules are oriented in space instead of only being aligned. When the molecules are oriented such that the fluorine atom points either in positive or in negative y-direction, see Fig. 4.9, the corresponding difference photoelectron angular distribution is clearly mirrored, as is shown in Fig. 4.15. An inversion of the VMI image for the case of oriented molecules cannot be performed, as the cylindrical symmetry is broken when the molecular axis is no longer parallel to the detector surface.

4.4 Effects of the Alignment Laser

For the previous analysis of the electron data, it has been implicitly assumed that the alignment laser has no effect besides fixing the molecular axes in space. It has been verified experimentally that the YAG laser pulse alone does not ionize the molecules, however, in adiabatic alignment the laser pulse is present during and after the X-ray ionization, and, therefore, two-color effects can occur.

The influence of the alignment laser on the fragmentation of pFAB molecules after inner-shell ionization was investigated by recording time-of-flight spectra with and without the alignment laser, as shown in Fig. 4.16. All large ionic fragments, including the broad parent ion peak, disappear when the YAG laser is present, the heaviest fragment that is found in the presence of the YAG laser pulses at full intensity is $C_4H_x^+$. A possible explanation for this observation could be that the heavy fragments are produced in excited electronic states in the inner-shell photoionization, or as intermediates in the following Auger decay. The YAG laser pulse may in this case be able to dissociate or ionize the excited states, with a single or a few photons, thereby producing smaller fragments. This is supported by the fact that the yield of the C_3H^+, CF^+, C_2^+, and especially C^+ ions increases when the YAG laser is present. Similar effects have been observed in pump-probe experiments on small molecules [158, 159] and on xenon atoms [160]. The fragments with the largest masses, especially $C_8H_5F^+$, are however produced by X-ray ionization of pFAB clusters, thus this effect may occur less strongly, or not at all for single molecules.

To investigate the dependence of the fragmentation on the intensity of the alignment laser, time-of-flight spectra have been recorded for different laser intensities that are shown in Fig. 4.17. They were recorded under velocity map imaging conditions, which for the experimental conditions at the LCLS decreased the mass resolution. Already at the lowest measured intensity, the parent ion peak starts to decrease, while the lighter fragments CF^+, $C_2H_x^+$, and CH_x^+ are largely unaltered. When the intensity is increased, these peaks start to grow, while the parent ion has already completely disappeared. This suggests that the latter process requires more YAG photons than the former.

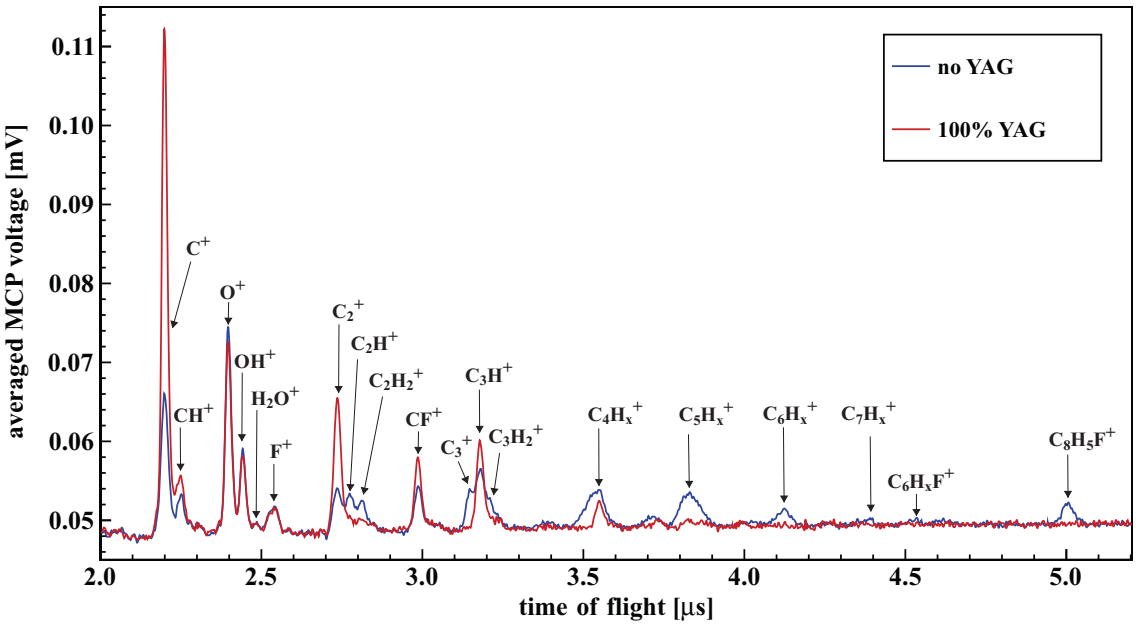

Figure 4.16: Time-of-flight spectra of pFAB recorded at the LCLS at a photon energy of 743 eV, with constant voltages on all spectrometer electrodes, with (red) and without (blue) the YAG alignment laser that has an intensity of $\sim 5 \times 10^{11}$ W/cm^2. The peaks for $m/q < 12$ are identical.

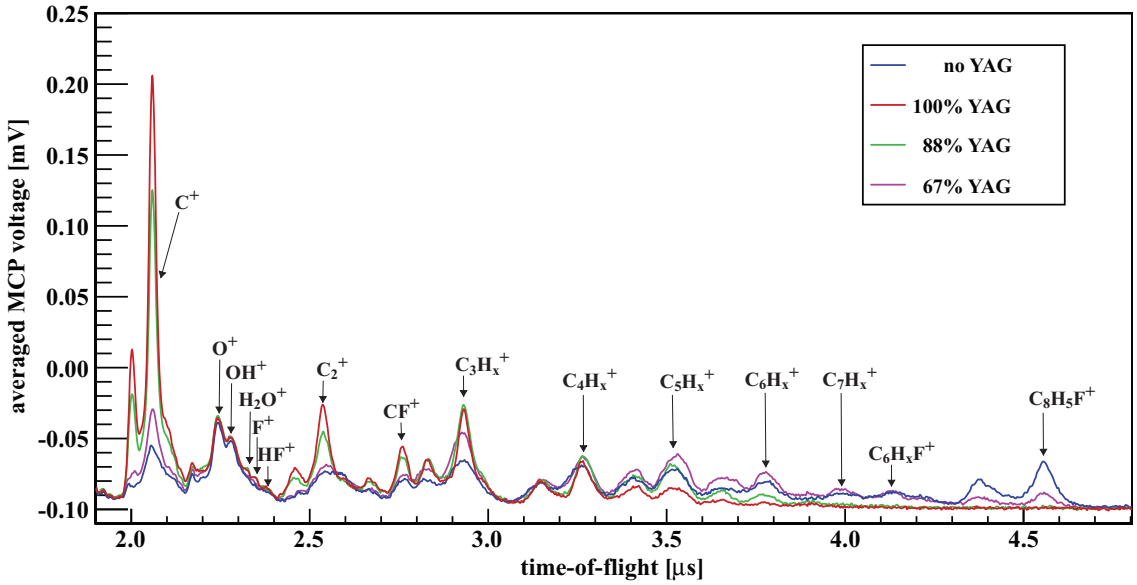

Figure 4.17: Time-of-flight spectra of pFAB recorded at the LCLS at a photon energy of 727 eV under velocity map imaging conditions for different YAG laser intensities. 100% corresponds to $\sim 5 \times 10^{11}$ W/cm^2. Unlabeled peaks are copies of their right-hand neighbor, caused by electrons that are created on the grid at the end of the drift tube, see also section 3.2.1. The peaks for $m/q < 12$ are identical.

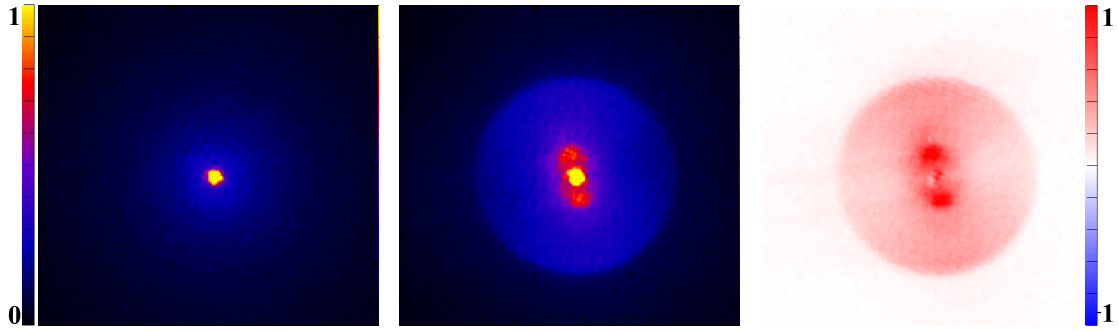

(a) without YAG (b) with YAG (c) 4.18(b) minus 4.18(a)

Figure 4.18: Zoom-in to the central part of the electron detector images in Fig. 4.10. The electron energies of the two features that are visible in (b) and (c) correspond to ∼0.11 and ∼1.12 eV. (c) is scaled by a factor of 2 with respect to (b).

Overall, the changes in the time-of-flight spectrum indicate that the YAG laser induces further fragmentation of the larger ionic fragments. Ionization of excited fragments by the alignment laser should result in the creation of additional electrons. When looking at the zoom-in to the central part of the electron detector images in Fig. 4.18, it becomes clear that two additional contributions of low-energy electrons emerge when the YAG laser is present. This is confirmed by the corresponding energy spectra in Fig. 4.19, obtained from inversion of the detector images[5] with the pBasex algorithm. The two features correspond to energies of approximately 0.11 and 1.12 eV, as calibrated with above-threshold ionization in argon, see section 3.2.6. The energy difference between the two contributions is close to the YAG photon energy of 1.17 eV, which may suggests that the two channels result from ionization by n and $n+1$ YAG photons. However, if these electrons were created from ionization of electronically excited molecules, molecular clusters, or fragments, one would expect a broad distribution of electron energies originating from different close-lying Rydberg states. The observed spectrum indicates that, instead, one or two states with a well-defined potential energy are ionized. Moreover, similar features of two low-energy electron contributions are also observed for dibromobenzene molecules, and when only residual gas is ionized by either the FEL or the TiSa laser, see Figs. 5.4 and 5.6. This may suggest that these electrons are not created from ionization of molecular fragments but from residual gas, although the changes in the fragmentation pattern of pFAB indicate that additional electrons should be created from the target molecules.

The photoelectron line at around 51 eV in the electron spectrum in Fig. 4.19 is rather broad, due to the LCLS bandwidth that is on the order of 1.5 - 7.5 eV at a photon energy of 743 eV [120], see also section 3.1.1. This uncertainty is not removed by

[5] Some electron hits in the center of the detector are lost due to reduced detection efficiency at the applied MCP voltage of 2.2 kV, see section 3.2.3. The absolute height of the low-energy electron peak may thus be slightly underestimated.

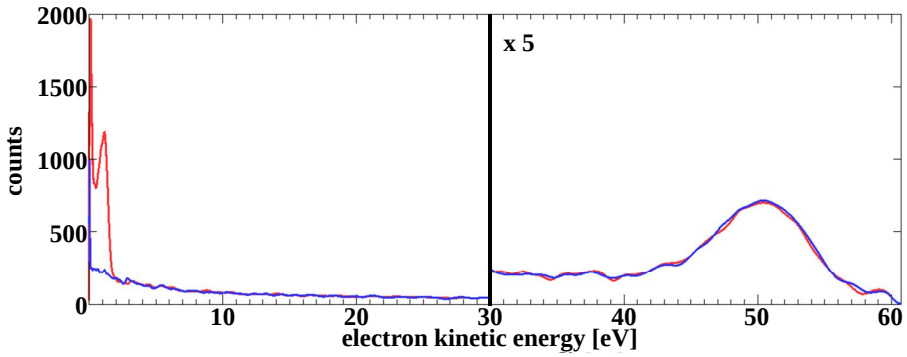

Figure 4.19: Electron spectrum of pFAB recorded at the LCLS at a photon energy of 743 eV with (red) and without (blue) the YAG alignment laser.

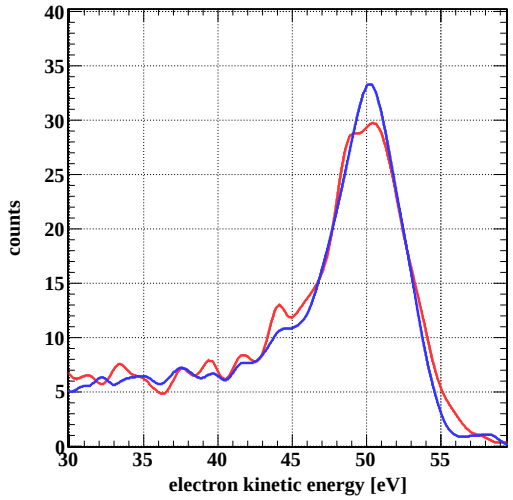

Figure 4.20: Photoelectron energy spectra recorded with (red) and without (blue) YAG alignment laser in a cone of 10° around the laser polarization direction. The data are the same as in Fig. 4.19.

selecting only those events for which the mean photon energy was in a ±2 eV window centered around the maximum, as it has been done for Fig. 4.19. A possible influence of the YAG on the photoelectrons is the formation of *sidebands* [161–163]. When the X-ray and the infrared laser pulses are present at the same time, the photoelectron can absorb or emit one or multiple YAG photons in addition to the X-ray photon in a process referred to as *two-color above-threshold ionization*. Each YAG photon can increase or decrease the nominal electron kinetic energy E_{kin} by 1.165 eV, resulting in a splitting of the photoline into multiple sub-lines, which is strongest for electron emission parallel to the YAG polarization direction. Due to the X-ray bandwidth, individual sidebands cannot be resolved in this case, but nevertheless, a slight broadening of the photoline is observed when the energy spectrum is analyzed within 10° around the laser polarization direction, see Fig. 4.20. This broadening and its angular dependence can also be seen in the detector difference image in Figs. 4.10(c)

and 4.11(c). For IR and XUV pulses with durations on the order of 10 fs, the overall width ΔE for which sidebands can be observed for photoelectrons of a given kinetic energy E_{kin} can be described by

$$\Delta E = 2E_0/\omega\sqrt{2E_{kin}}cos\chi, \tag{4.4}$$

where E_0 is the maximum electric field of the IR laser, ω is its frequency, and χ is the angle between the electron emission direction and the (parallel) linear polarization directions or the light [164].[6] The occurrence of sidebands is thus strongest for electron emission along the polarization direction. For the present experiment, the intensity of the 10 ns IR pulse was about 5×10^{11} W/cm^2 and the wavelength 1064 nm, which would result in a width of $\Delta E = 8.7$ eV for $\chi = 0$ and $E_{kin} = 51$ eV. This is consistent with the observed width and is of the same order as the LCLS bandwidth, although it has to be noted that Eq. 4.4 is not explicitly specified for IR pulses of ns duration. Still, sidebands have been observed experimentally also for long IR pulses [163]. For the analysis of the photoelectron angular distributions in section 4.3 it has been assumed that the creation of sidebands does not significantly affect the photoelectron angular distribution as long as the photoelectron intensity is radially integrated over all sidebands.

[6] Eq. 4.4 is given in atomic units.

5 Pump-Probe Experiments on Laser-Aligned Molecules

In this chapter, the results of a first proof-of-principle study at the LCLS in May 2010 are discussed that aimed at investigating the feasibility of time-resolved photoelectron diffraction experiments on laser-aligned molecules at a Free-Electron Laser. 1,4-dibromobenzene (DBB, $C_6H_4Br_2$) molecules, see Fig. 5.1, were adiabatically laser-aligned, and dissociated by a femtosecond titanium-sapphire (TiSa) laser pulse, before ionizing the Br($2p$) level with the LCLS X-ray pulse. Static photoelectron angular distributions at electron kinetic energies of 20 and 35 eV have been recorded, and pump-probe measurements have been carried out with 20 eV photoelectrons. This chapter concentrates on the pump-probe aspect of the experiment. Results of the static measurements are described in reference [165].

The experimental set-up was identical to the pFAB experiment, except for small modifications. The TiSa laser was propagated through the chamber collinearly to the YAG alignment laser. A phosphor screen was mounted on the electron side of the VMI spectrometer, whereas on the ion side a slit with a width of 1 mm was inserted on the first electrode, to select only ionic fragments with $p_x \approx 0$ that were created in the laser focus. This allowed to record ion time-of-flight spectra simultaneous to the electron measurement, using a delay-line anode. In order to probe the molecular alignment, the polarity of the applied voltages had to be switched such that Br^+ fragments were imaged on the phosphor screen on the opposite side. Details of the image processing and conventions for detector images and polar plots of angular distributions are given in section 3.2.

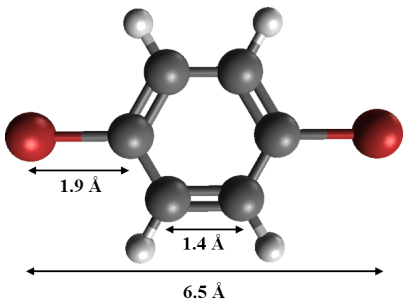

Figure 5.1: Equilibrium geometry of the 1,4-dibromobenzene molecule (DBB, $C_6H_4Br_2$).

5.1 Ionic Fragments

In the previous chapter it was shown that the YAG alignment laser can influence the molecular fragmentation after inner-shell photoionization. In a pump-probe experiment on adiabatically laser-aligned molecules, the combination of three different light pulses gives rise to a variety of effects. To characterize the fragmentation of dibromobenzene, time-of-flight spectra are recorded on the ion side of the VMI spectrometer simultaneously to the photoelectron measurement. The slit inserted in the spectrometer introduces a limited acceptance for ions with non-zero kinetic energy, which changes as a function of the ion momentum. Therefore, the spectra allow for qualitative investigation of the fragmentation, but the yield of fragments with higher kinetic energies may be significantly underestimated.

The time-of-flight spectra for all possible combinations of light pulses are shown in Fig. 5.2 for two different polarization directions of the TiSa laser. The X-ray energy of 1570 eV lies 20 eV above the Br($2p_{3/2}$) level but below the Br($2p_{1/2}$) level. The photoabsorption cross sections at this photon energy are 527 kb for bromine, 12 kb for carbon, and 0.003 kb for hydrogen [166], thus 98% of the absorbed photons are absorbed at the bromine. The FEL alone creates mostly Br^+ ions and a few Br^{++} ions, as well as some smaller $C_xH_x^+$ fragments. A very small, narrow parent ion peak is also detected, which probably results from fluorescent decay of the core-hole or from valence ionization. This is different from what has been found in the pFAB data, where a large, broad parent ion peak has been observed that was attributed to molecular clusters. The TiSa laser pulse creates significantly more parent ions; the peak in the time-of-flight spectrum shows a triple structure due to the two different bromine isotopes of 79 and 81 amu with almost equal natural abundance. Accordingly, fragments that contain one bromine show a double peak structure. A small amount of doubly charged DBB is found also, but mostly the molecules decay further into smaller fragments, most prominently Br^+. When the TiSa laser pulse arrives after the FEL pulse, the resulting spectrum looks very similar to the spectrum that is recorded with only the TiSa laser. This can be explained by the fact that the focus of the TiSa laser was chosen larger than the FEL focus, to ensure that all molecules probed by the X-rays were also in the focus of the pump laser. The spectrum is thus dominated by molecules that have only been ionized by the TiSa laser.

When the X-rays ionize molecules that are adiabatically aligned by the YAG laser instead of randomly oriented, the spectrum changes slightly. The Br^+ and the C^+ peaks become more pointed in the center when the YAG laser pulse is present, and a little more Br^{++} ions are created. The very small peaks corresponding to $C_6H_4Br_2^+$ and $C_6H_4Br_2^{++}$ disappear. In the pFAB data in the previous chapter, several large fragments were created by the FEL pulse alone that disappeared when the YAG laser pulse was added. The reason for this qualitative difference may be that no molecular DBB clusters are created, indicating that the effect of the YAG on the pFAB fragmentation may be dominated by ionization or dissociation of molecular

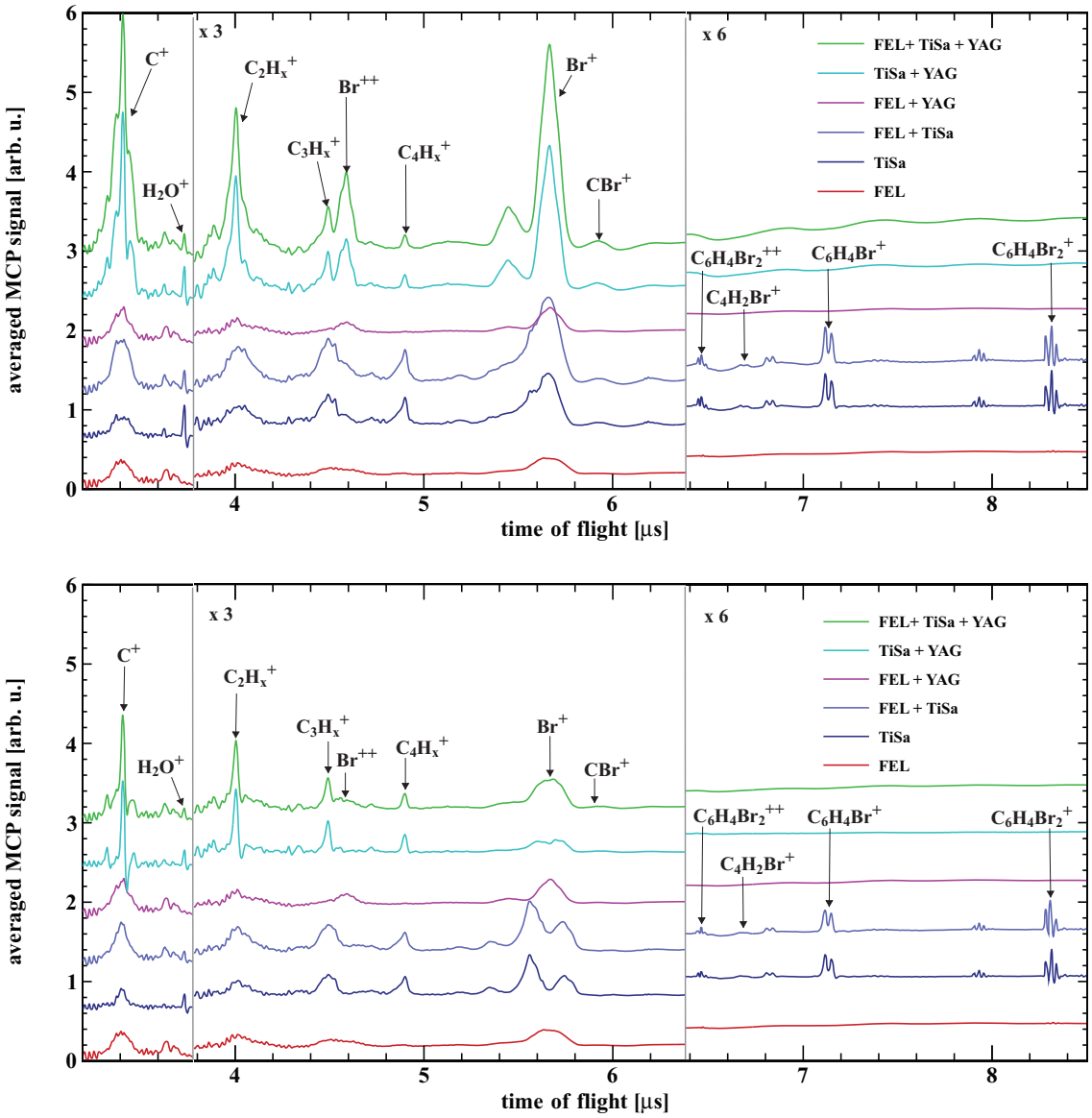

Figure 5.2: Time-of-flight spectra of dibromobenzene recorded at the LCLS at a photon energy of 1570 eV for different combinations of light pulses, normalized to the number of events. Top: FEL, YAG and TiSa laser polarization lie along y. The TiSa pulse arrives 0.5 ps after the FEL pulse. Bottom: FEL and YAG laser polarization lie along y, the TiSa laser polarization lies along z. The TiSa laser pulse arrives 1 ps before the FEL pulse. The YAG pulse alone is non-ionizing. The first 3 μs of the spectrum are heavily disturbed by high-frequency pickup from the high-voltage switching of the electron detector on the opposite side, thus only fragments with m/q >12 are shown. Unlabeled peaks are copies of their right-hand neighbor that arise from the velocity map imaging conditions, see section 3.2.1. The traces beyond 3.8 μs are scaled up by a factor of 3, and the traces beyond 6.4 μs are scaled up by a factor of 6 for better visibility.

clusters. When the strong-field ionization of the TiSa laser is combined with adiabatic alignment, the changes in the spectrum are significant. If the TiSa polarization lies parallel to the direction of the molecular alignment, as shown in the top spectrum in Fig. 5.2, the Br^+, Br^{++}, $C_2H_x^+$ and the C^+ peaks are strongly enhanced as compared to ionization of randomly oriented molecules. This demonstrates that molecules that are aligned with their major axis along the TiSa polarization direction are ionized more efficiently. When the TiSa polarization is rotated such that it is perpendicular to the YAG polarization, see the bottom spectrum in Fig. 5.2, the peak of Br^+ is smaller as compared to ionization of randomly oriented molecules, confirming that molecules aligned perpendicular to the TiSa laser polarization direction are less efficiently ionized. The $C_2H_x^+$ and the C^+ peaks rise, but the increase is smaller than for the parallel polarization. Br^{++} is absent in this spectrum.

Moreover, when the TiSa and the YAG laser interact with the molecular ensemble, all ions heavier than Br^+ disappear, independent of the TiSa laser polarization direction. This may be explained by the fact that, in general, electronic transitions happen on a timescale much faster than the nuclear motion, and usually the internuclear distances in a valence ionized molecule are larger than in the molecular ground state. Therefore, a vertical *Frank-Condon* transition can result in a superposition of highly vibrationally excited states, such that the molecule may have a dissociation or ionization energy that is low enough to be overcome by a single or a few YAG photons. Molecular dynamics initiated by a femtosecond pump laser pulse may thus be significantly influenced by an additional nanosecond YAG laser pulse. When the X-ray pulse is added to the TiSa and the YAG laser pulses, the spectrum is not altered significantly due to the larger focus of the TiSa laser beam.

To characterize the molecular alignment, the polarity of all voltages was changed and the phosphor detector was gated for 400 ns to image Br^+ ions. The alignment can be probed either by the FEL or the TiSa laser pulse. As the ionization probability in strong-field ionization is in general enhanced along the laser polarization direction, the TiSa polarization direction was rotated such that it was perpendicular to the detector plane, along the z-axis, to remove the effect of so-called *geometric alignment*. For inner-shell ionization by the FEL far above the ionization threshold, the absorption cross section is usually nearly independent of the angle between light polarization and the molecular axis, making X-rays a less biased probe for molecular alignment [167]. When randomly oriented molecules are ionized, by either the FEL or the TiSa laser pulse, the resulting Br^+ fragments are isotropically distributed on the detector, see Figs. 5.3(a) and 5.3(b). When the FEL ionizes DBB molecules, a ring of Br^+ is found, demonstrating that the Br^+ ions are emitted with significant kinetic energy. A second, weak contribution can be identified in the center of the image, which probably corresponds to triply charged DBB ions that have nearly the same time of flight as singly charged bromine ions. When DBB is ionized by the TiSa laser, most Br^+ fragments are emitted along the polarization direction, resulting in a maximum in the center of the image and additional contributions with higher kinetic energy at larger radii.

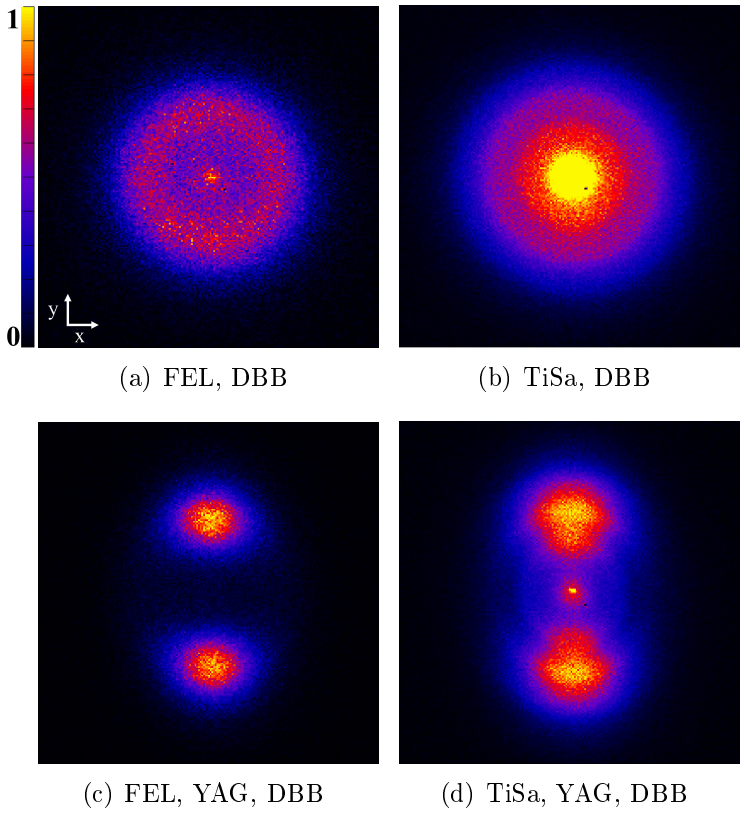

(a) FEL, DBB (b) TiSa, DBB

(c) FEL, YAG, DBB (d) TiSa, YAG, DBB

Figure 5.3: Detector images for Br^+ fragments, resulting from ionization of dibromobenzene molecules (DBB). Top row: ionization of randomly oriented molecules by the FEL and the TiSa laser. Bottom row: ionization of aligned molecules by the FEL and the TiSa laser. The TiSa laser polarization direction is along z, perpendicular to the detector plane. The FEL polarization lies along y. The YAG laser is elliptically polarized with a ratio of 1:7, the major polarization axis lies along y and the minor axis along z. (a) is scaled by a factor of 2 with respect to (c).

When an elliptically polarized YAG laser pulse is added, the Br^+ distributions are confined along the major axis of the YAG laser polarization direction, see Figs. 5.3(c) and 5.3(d). Three different fragmentation channels resulting from ionization by the TiSa can be distinguished in Fig. 5.3(d). They correspond to fragmentation of parent ions with increasing total charge, leading to Br^+ ions with increasing kinetic energies. For inner-shell ionization with FEL pulses, different fragmentation channels often strongly overlap in energy [16, 168], thus they cannot be as clearly distinguished in Fig. 5.3(c). The contribution of triply charged DBB ions with very little kinetic energy has disappeared, confirming that the YAG laser pulse leads to fragmentation of intact DBB ions. The contribution in the center of Fig. 5.3(d) on the other hand probably corresponds to Br^+ ions that have a neutral fragmentation partner. When comparing the Br^+ distributions in this experiment with the F^+ distributions from pFAB, see Fig. 4.8, it can be noted that no background from ionization of residual gas is present, and no additional contribution from molecular clusters arises, thus no background subtraction is necessary. The degree of molecular alignment of

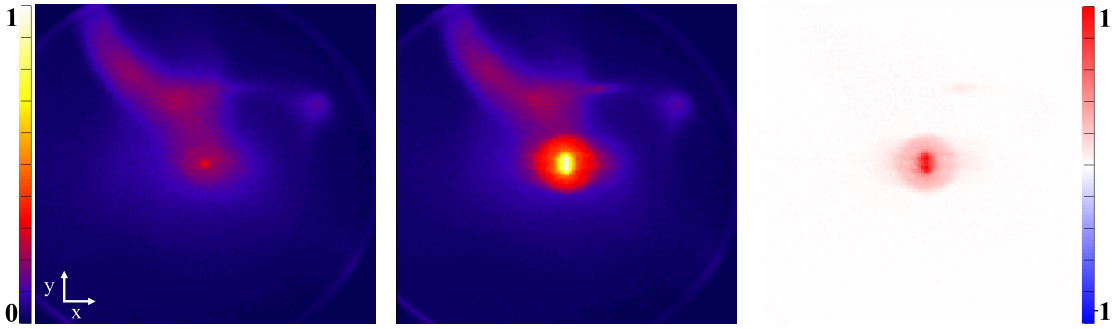

(a) FEL, no target (b) FEL, YAG, no target (c) 5.4(b) minus 5.4(a)

Figure 5.4: Electron detector images for ionization of residual gas by the FEL at a photon energy of 1570 eV. The FEL polarization direction lies along y. In (b), an elliptically polarized YAG pulse with a ratio of 1:7 is added, the major axis of the polarization direction lies along y and the minor axis along z.

the Br-Br axis can be obtained from Figs. 5.3(c) and 5.3(d) by employing Eq. 4.1, resulting in $\langle\cos^2\theta_{2D}\rangle = 0.78$ and $\langle\cos^2\theta_{2D}\rangle = 0.75$, respectively. For the elliptically polarized YAG laser pulse, the plane of the benzene ring should in principle have been fixed in the (y, z) plane, which could have been probed by additional monitoring of hydrogen or carbon ions [169] but has not been done in this experiment.

5.2 Photoelectron Distributions

In a laser-pump, FEL-probe experiment on adiabatically laser-aligned molecules, three light pulses are present at the same time. In order to extract delay-dependent photoelectron angular distributions, the respective photoelectrons have to be isolated from other electrons that are created by any one of the three light pulses. As will be seen in the following, this can be difficult to achieve. This section will first describe the results obtained for ionization of laser-aligned molecules by only the FEL and only the TiSa laser pulse, afterwards the combination of all three light pulses is shown and possible time-dependent multi-color effects are discussed.

5.2.1 X-ray Photoionization

In 2010, the LCLS, the TiSa laser and the data acquisition system operated at 60 Hz, and the YAG laser has a repetition rate of 30 Hz, thus simultaneous recording of background while measuring aligned and randomly oriented molecules was not possible. Therefore, separate data sets without the molecular beam and for different combinations of light pulses were recorded. Figure 5.4(a) displays the signal from ionization of residual gas by only the FEL at a photon energy of 1570 eV. As ionization events occur not only in the center of the VMI spectrometer but anywhere

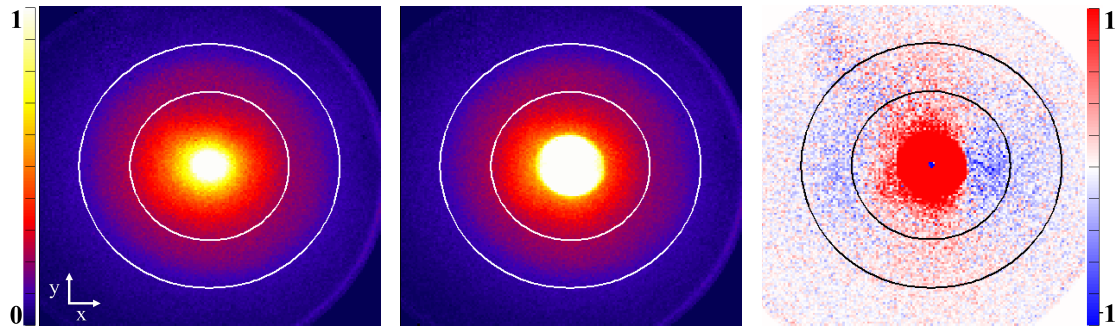

(a) FEL, DBB (b) FEL, YAG (y), DBB (c) 5.5(b) minus 5.5(a)

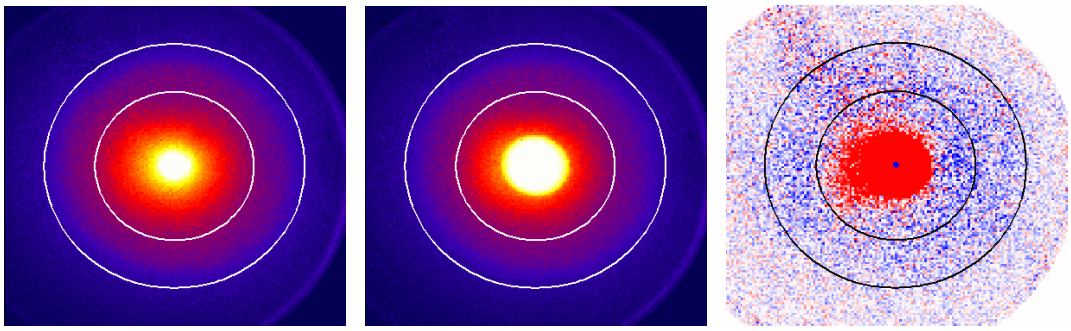

(d) FEL, DBB (e) FEL, YAG (z), DBB (f) 5.5(e) minus 5.5(d)

Figure 5.5: Electron detector images for ionization of DBB by the FEL at a photon energy of 1570 eV that has been filtered to ± 1 eV. The background from residual gas has been subtracted. Different polarization directions of the elliptically polarized alignment laser with a ratio of 1:7 are shown. Top row: the major axis of the YAG polarization lies along y. Bottom row: the major axis of the YAG polarization lies along z. The rim of the projected photoline is marked by the circles. Image differences are taken without background subtraction and without photon energy filter.

along the FEL beam path, the electrons are not well focused, resulting in the artificial, asymmetric projection. When the YAG laser pulse is present in addition to the FEL, two additional, contributions of low-energy electrons can be identified in the image in Fig. 5.4(b) and in the difference image in Fig. 5.4(c) that have energies of less than ~ 1.5 eV. These images provide the background for all measurements of dibromobenzene molecules that are aligned along the y-axis. For measurements with alignment along z, a second set of background images was recorded.

Figure 5.5 shows electron detector images for ionization of dibromobenzene molecules by FEL pulses with a photon energy of 1570 eV, which is 20 eV above the Br($2p_{3/2}$) level at 1550 eV [31] but below the Br($2p_{1/2}$) level at 1596 eV, thus only one photoline is expected. The resulting photoelectrons with an almost isotropic angular distribution can be seen best in the region marked by the circles. They are, however, not well separated from low-energy electrons that are most likely created by multi-electron processes or by inelastic electron scattering. Moreover, significant electron intensity is found at radii outside of the photoline. The initial vacancy in the Br($2p_{3/2}$) level decays predominantly via LMM- and MNN-Auger decays (similar as in kryp-

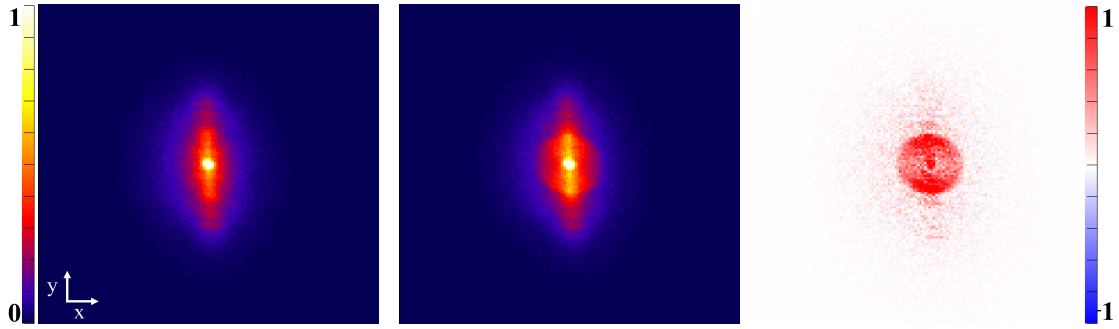

(a) TiSa, no target (b) TiSa, YAG, no target (c) 5.6(b) minus 5.6(a)

Figure 5.6: Electron detector images for ionization of residual gas by the TiSa laser. The TiSa and the YAG polarization lie along y. (c) is scaled by a factor of 7.5 with respect to (a) and (b).

ton [170]), resulting in electrons with kinetic energies of $> 1200\,\mathrm{eV}$ and $< 100\,\mathrm{eV}$, respectively [31]. The latter contribute a significant number of electrons everywhere on the detector, also outside of the photoline. Compared to the electron detector images for pFAB in Fig. 4.10, here the photoelectrons are less separated from the low-energy electrons due to the lower photoelectron kinetic energy. Moreover, for ionization of a $2p$ level, the emitted photoelectron wave is generally less asymmetric than for ionization of a $1s$ orbital. This implies that more photoelectrons are projected to the center of the image, see section 6.1.

The electron detector image for X-ray ionization of adiabatically aligned DBB molecules is shown in Fig. 5.5(b). No significant difference can be seen in the photoelectron distribution, but again additional low-energy electrons are created. As the background image in Fig. 5.4(b) has been subtracted, these electrons either originate from a different process involving DBB molecules, or from residual gas that is present in the molecular beam. When subtracting the distribution of randomly oriented molecules, the difference image in Fig. 5.5(c) results. In this image it can be clearly seen that the photoelectron angular distribution is more pointed along the Br-Br axis when the molecules are spatially aligned, resulting in a positive difference along the y-axis and a negative difference along th x-axis.

The bottom row of Fig. 5.5 shows the same images for molecular alignment perpendicular to the detector plane. As expected, no angular dependence is found in the photoelectron distribution, but for aligned molecules less photoelectrons are created. This suggests that the Br($2p$) photoionization probability may slightly decrease when the molecules are aligned with the Br-Br axis perpendicular to the FEL polarization direction. This is qualitatively consistent with an observed decrease of the total electron count rate of about 10% for this geometry. However, since the overall electron count rate includes not only the photoelectrons, this number cannot be interpreted straightforwardly as a quantitative measure of the molecular axis dependence of the photoionization cross section.

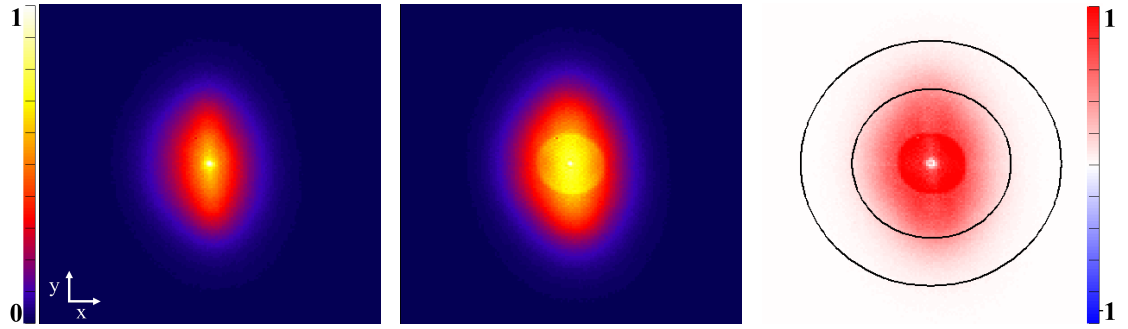

(a) TiSa (y), DBB (b) TiSa (y), YAG, DBB (c) 5.7(b) minus 5.7(a)

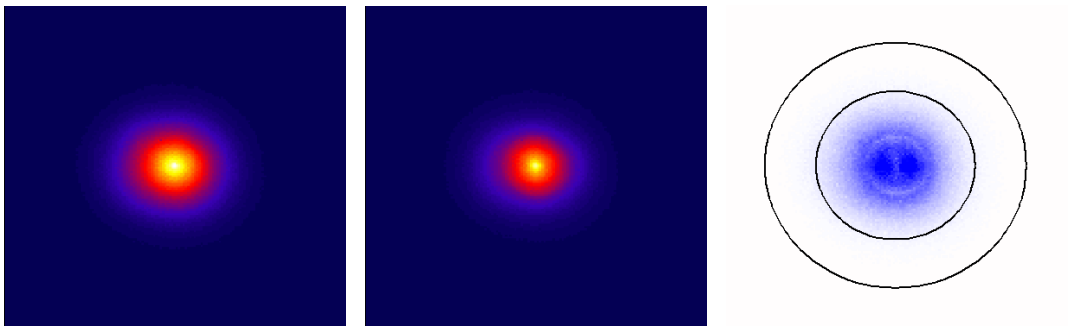

(d) TiSa (z), DBB (e) TiSa (z), YAG, DBB (f) 5.7(e) minus 5.7(d)

Figure 5.7: Electron detector images for ionization of DBB by the TiSa laser with a photon energy of 1.55 eV. The polarization direction of the linearly polarized YAG laser lies along y. Top row: the TiSa laser polarization direction lies along y. Bottom row: the TiSa laser polarization direction lies along z. The region of interest for the rim of the 22 eV photoline is marked by the circles. (c) is scaled by a factor of 4 with respect to (a) and (b). (f) is scaled by a factor of 7.5 with respect to (d) and (e).

5.2.2 Infrared Photoionization

The infrared TiSa laser with a photon energy of 1.55 eV cannot ionize dibromobenzene or residual gas in the chamber directly by single-photon ionization, as ionization energies are 8.9 eV for DBB and 15.6 and 12.6 eV for nitrogen and water, respectively [171]. In order to dissociate DBB, the TiSa intensity was set to $2 \times 10^{14}\,\mathrm{W/cm^2}$, such that multi-photon ionization occurs. Figure 5.6 shows a background measurement at this intensity without the molecular beam for horizontal TiSa polarization. Rings from above-threshold ionization are visible which probably stem from water. When the YAG laser is added, also in this case additional low-energy electrons are created. However, in Fig. 5.6(c) the outer feature is enhanced as compared to the case of ionization of residual gas by the FEL in Fig. 5.4(c) and the angular distribution is slightly different.

If the molecular beam is turned on, the detector image in Fig. 5.7(a) arises when the TiSa laser polarization is parallel to the detector plane, along the y-axis. An elongated distribution of electrons created by strong-field ionization is visible, how-

ever, in contrast to the background measurement for dibromobenzene no individual rings can be distinguished. Dibromobenzene has a lower ionization energy than the residual gas, thus probably at the given intensity the tunneling regime of strong-field ionization is already reached for DBB, whereas for the residual molecules the ATI structure can still be resolved. When the molecules are not randomly oriented, but aligned parallel to the TiSa laser polarization direction, more electrons are created, see Fig. 5.7(b). This can be explained by the fact that strong-field ionization is more likely to occur for molecules that are aligned parallel to the laser polarization direction. Additional low-energy electrons are created by the YAG laser that are visible in the center of the image. When normalizing both images to the same number of events and subtracting them, the image in Fig. 5.7(c) emerges. It reveals that the non-isotropic difference in electron intensity reaches out to the radial region of interest for the Br($2p$) photoline created by the X-rays, indicated by the circles. Therefore, it is necessary to remove this electron contribution from images that investigate changes in the photoelectron angular distributions.

When the TiSa laser polarization is rotated such that it is perpendicular to the detector plane, the created electrons are preferentially emitted along the spectrometer axis and are thus projected to the center of the image, see Fig. 5.7(d) and 5.7(e). The YAG laser polarization remains parallel to the detector surface. Thus, here less electrons are created for molecules aligned perpendicular to the TiSa laser polarization as compared to randomly oriented molecules. This results in a negative difference, see Fig. 5.7(f), which in this case is almost isotropic in the detector plane and is more confined to the center of the image.

5.2.3 Two- and Three-Color Effects

The idea of the infrared-pump, X-ray-probe experiment is to first dissociate aligned dibromobenzene molecules with the TiSa laser pulse, and then to probe them with the FEL pulse that arrives with a certain time delay. One of the major difficulties in any pump-probe experiment is to establish an efficient pumping process and to extract a delay-dependent signal from the mixture of pumped and un-pumped molecules. As was demonstrated in the last section, strong-field ionization is enhanced when the major molecular axis coincides with the laser polarization direction. Therefore, to achieve efficient pumping of the aligned molecules, it is straightforward to chose the polarization directions of the YAG and the TiSa laser parallel. However, the alignment-dependent contribution of electrons that are created by the TiSa laser, see Figs. 5.8(a) and 5.8(b), needs to be removed from the images for randomly oriented and aligned molecules separately before their difference is calculated. Otherwise the structure in Fig. 5.7(c) overlaps with the difference photoelectron angular distribution.

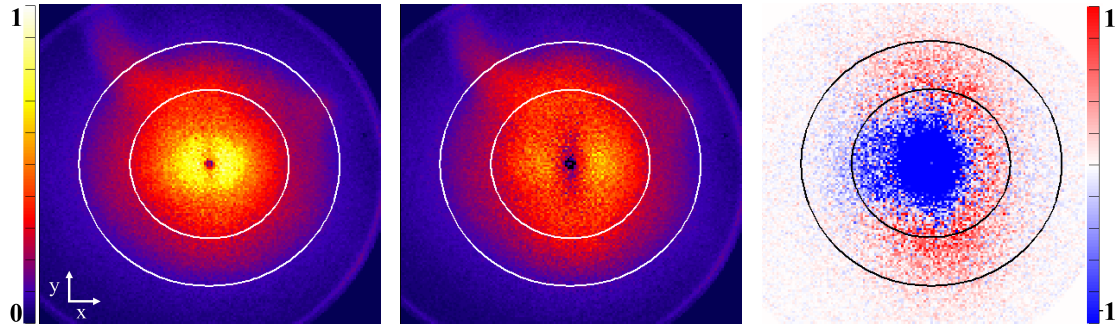

(a) FEL, TiSa (y), DBB minus 5.7(a)

(b) FEL, TiSa (y), YAG, DBB minus 5.7(b)

(c) 5.8(b) minus 5.8(a)

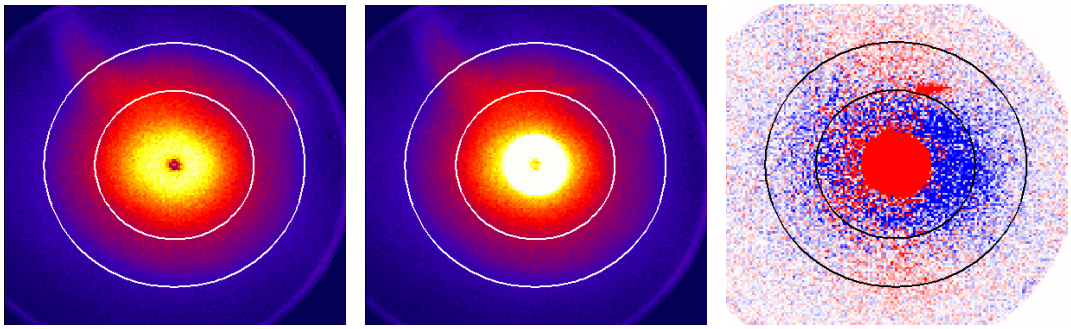

(d) FEL, TiSa (z), DBB minus 5.7(d)

(e) FEL, TiSa (z), YAG, DBB minus 5.7(e)

(f) 5.8(e) minus 5.8(d)

Figure 5.8: Electron detector images for ionization of DBB by the TiSa laser and the FEL at a photon energy of 1570 eV. The polarization direction of the linearly polarized YAG laser lies along y. Top row: the TiSa laser polarization direction is along y, and the TiSa pulse arrives 2.5 ps after the FEL. Bottom row: the TiSa laser polarization is along z, and the TiSa pulse arrives roughly at the same time as the FEL. The background from ionization of DBB by only the TiSa laser has been subtracted. The rim of the projected photoline is marked by the circles. (c) is scaled by a factor of 12 with respect to (a) and (b). (f) is scaled by a factor of 50 with respect to (d) and (e).

Figures 5.8(a) and 5.8(b) show the resulting distributions for randomly oriented and one-dimensionally aligned DBB molecules, respectively, after subtracting the signal obtained without the FEL. Although the images are normalized to the same number of events before subtraction, the electron signal from strong-field ionization by the TiSa is not removed efficiently. Too little signal is subtracted at larger radii, whereas in the image center too much intensity is subtracted. This suggests that the TiSa intensity may have been slightly lower during the background measurement, which seems possible as the background images were recorded 3 hours after the pump-probe data. A decrease in the intensity of the TiSa laser changes the electron spectrum in a non-uniform way: high-energy electrons are suppressed more strongly than low-energy electrons. This effect cannot be removed in retrospect, and it overlaps with the diffraction structure of the photoelectrons, as can be seen in the broad positive difference along the y-axis in Fig. 5.8(c).

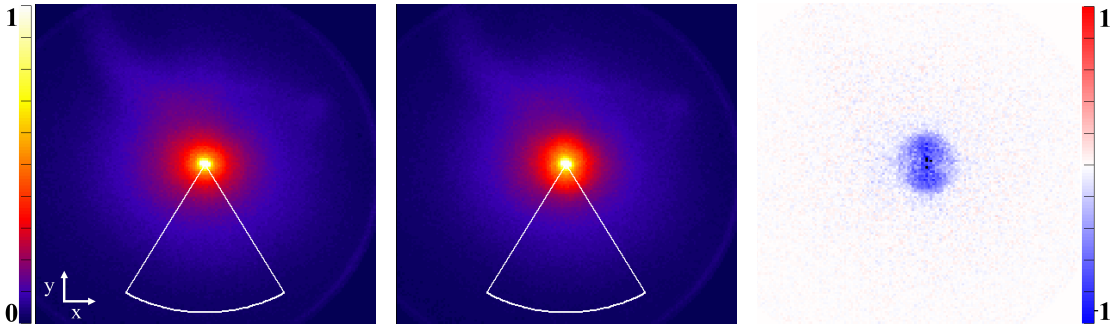

(a) TiSa 1 ps before FEL (b) TiSa 3 ps after FEL (c) 5.9(a) minus 5.9(b)

Figure 5.9: Electron detector images for two different settings of the delay stage and their difference image. The TiSa laser polarization direction lies along y and the intensity has been decreased such that the TiSa laser alone is non-ionizing. The absolute calibration of the delay value is determined from Fig. 5.10. (c) is scaled by a factor of 2 with respect to (a) and (b). The white lines indicate regions of interest for the plots in Fig. 5.10.

When the TiSa laser polarization is rotated such that it is perpendicular to the detector plane, the images in the bottom row of Fig. 5.8 result after the background without the FEL has been subtracted. The negative difference in the center of the image that stems from electrons created by the TiSa alone, see Fig. 5.7(f), is not completely removed, confirming that probably the TiSa intensity was lower when the background was recorded. Still, a faint structure can be identified in the difference photoelectron distribution that shows a positive difference along y and a negative difference along x, similar to what was observed for ionization by only the FEL, see Fig. 5.5(c). This suggests that it may be possible to see delay-dependent effects of this angular distribution. However, the TiSa laser dissociates the molecules much less efficiently if its polarization direction is perpendicular to the molecular alignment, thus it is questionable which fraction of the aligned molecular ensemble is dissociated in this experimental geometry before being ionized by the FEL.

5.2.4 Delay-Dependent Effects

In order to carry out a pump-probe experiment, first the spatial and temporal overlap between all laser pulses has to be established. The synchronized arrival time on the target is referred to as T_0 in the following. The coarse synchronization of the TiSa laser pulse to the FEL pulse was found by monitoring the arrival times of both pulses with a fast photodiode that can achieve a precision of about 20 ps. Afterwards, fine adjustment needs to be achieved with the help of a signal that changes depending on which of the laser pulses arrives first. Here, this has been done by rotating the TiSa laser polarization direction along the y-axis, and decreasing the TiSa intensity until no molecules were ionized by the TiSa alone, corresponding to 82% of the intensity that was used to record the pump-probe data. The delay between TiSa and FEL pulses was varied by moving a mechanical stage. The electron detector

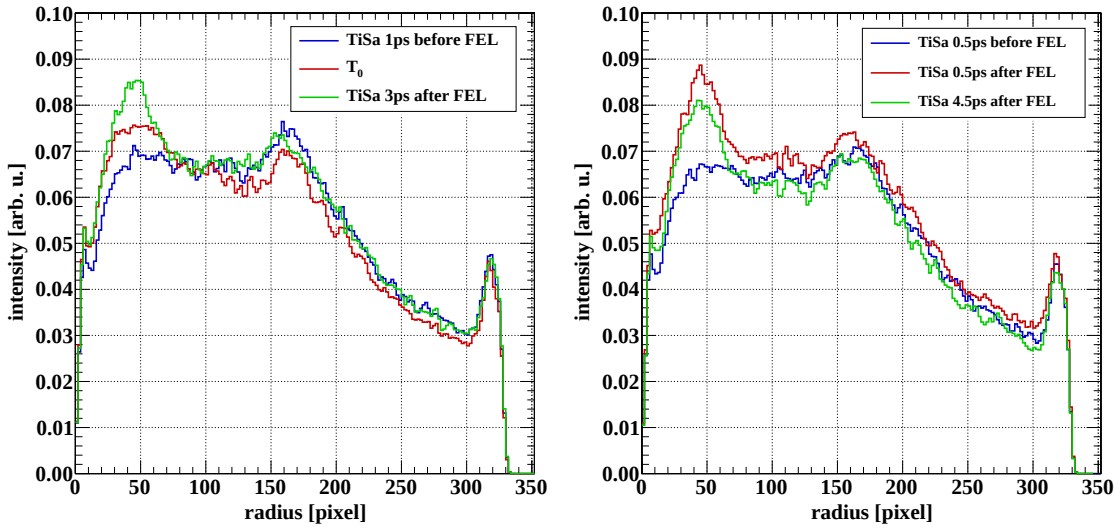

(a) (b)

Figure 5.10: Measurements to find the temporal overlap T_0 between the TiSa laser pulse and the FEL pulse (without the YAG laser). Shown are electron intensities projected to the radius in the angular region of interest marked in Fig. 5.9, see also section 3.2.4. Three different settings of the delay stage are shown, normalized to the number of FEL shots. The second measurement in (b) was necessary after a 'jump' in the arrival time of the TiSa laser pulse had occurred.

images for two different settings of the delay stage with a temporal spacing of 4 ps are shown in Fig. 5.9(a) and 5.9(b).[1] The difference image in Fig. 5.9(c) shows a pronounced negative structure in the center of the image, corresponding to electron kinetic energies of ≤ 1.5 eV. This indicates that these electrons are created by post-ionization of excited molecular states by the TiSa laser, similar to the low-energy feature that appears in all images recorded with the YAG laser. If the TiSa pulse arrives earlier than the FEL pulse, the molecules are still in the ground state and cannot be ionized by the TiSa.

In order to determine T_0, the projections of the electron intensity onto the radius on the detector are plotted in Fig. 5.10(a) for the angular regions of interest marked in Fig. 5.9. A third setting of the delay stage is plotted also. A rise of the low-energy electron signal at around $r = 50$ can be clearly identified when the TiSa pulse arrives later than the FEL pulse, whereas the intensity in the rim of the projected photoline at around $r = 170$ stays almost constant. In principle, the ionization probability of the TiSa laser should be a step function that is zero if the TiSa pulse arrives before the FEL. However, it needs to be taken into account that the arrival time jitter between the FEL and the TiSa pulses is about $0.2 - 0.3$ ps, which smears out this sharp rise and prohibits to pinpoint the temporal overlap exactly. This leads to an averaged signal between TiSa pulses arriving before and after the FEL at T_0, as

[1] The relative delay in femtoseconds is given by subtracting the respective values of the LCLS LAS:FS1:Angle:Shift:Ramp:Target parameter and multiplying them by 100.

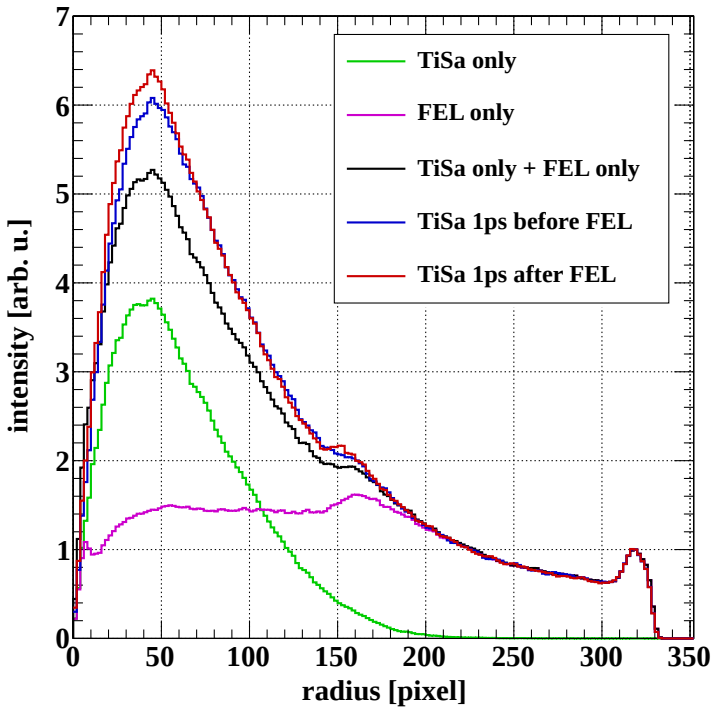

Figure 5.11: Radial projections of electron intensities for the region of interest marked in Fig. 5.9, see also section 3.2.4. The distributions are normalized to the signal on the edge of the detector at $r = 320$. Pump-probe data for two different settings of the delay stage (blue, red) are shown as well as reference curves for only the TiSa laser (green) and only the FEL present (magenta). The sum of the reference measurements is plotted for comparison (black).

is seen for the red curve in Fig. 5.10(a). This setting is defined as T_0. Recording data at more closely spaced delay stage settings could maybe have helped to settle T_0 more precisely. By now, X-ray-optical cross-correlation methods are available that allow to correct for the arrival time jitter [172–174], such that the temporal resolution of an IR-pump, X-ray-probe experiment is only limited by the respective pulse durations [175].

After successful determination of the temporal overlap, the TiSa polarization was rotated back, parallel to the z-axis, and the intensity was set back to the original value. For this setting, three pump-probe data sets were recorded, at the nominal zero delay T_0 and for two delays of ± 1 ps, respectively. Figure 5.11 shows radial projections of electron detector images for the case when the TiSa pulse arrives 1 ps before the FEL pulse, and 1 ps after the FEL pulse. The angular region of interest is the same as in Fig. 5.9. Reference measurements taken with only the TiSa and with only the FEL, as well as their sum are also shown for comparison. When comparing these two reference distributions, it becomes clear that roughly 50 % of the total electron intensity is created by strong-field ionization from the TiSa. Their high-energy tail overlaps with the rim of the photoline at around $r = 170$, even in this case where the TiSa laser polarization direction was perpendicular to the detector

surface. Electron intensities at $r \geq 220$, with higher kinetic energies than the direct photoelectrons are created only by the FEL. These are most likely bromine MNN-Auger electrons with kinetic energies of < 100 eV. Figure 5.11 leads to the conclusion that the photoelectrons are superimposed with the electrons created by the pump pulse at all radii, which makes correct a subtraction of the low-energy electron peak indispensable.

If the TiSa laser pulse interacts with the molecular ensemble after it has been ionized by the FEL, the Br($2p$) photoelectrons should not be affected much. The electrons from strong-field ionization on the other hand can be enhanced by the preceding FEL pulse, as has been seen in the procedure for finding the temporal overlap. When comparing the red and the black curves in Fig. 5.11, it can be seen that their general shape is very similar, but the peak at small radii is larger when the FEL pulse ionizes the molecules before the TiSa pulse arrives, which is consistent with the effect that was seen in the T_0 determination. However, when the TiSa pulse arrives earlier than the FEL pulse, the peak in the blue curve is only slightly lower than in the red curve and significantly higher than for the reference measurement. Another possible reason for changes in the peak at smaller radii is a drift in the TiSa laser intensity between the different measurements. Strong-field ionization depends non-linearly on the laser intensity, thus small fluctuations can have significant effects. As the reference spectrum with only the TiSa pulse has been recorded twelve hours after the pump-probe data, a small decrease in the laser intensity within that time seems possible. Unfortunately, the TiSa intensity was not monitored during the data taking, no reference measurements were recorded in between the different data sets and simultaneous background recording was not possible as the LCLS data acquisition operated only at 60 Hz in 2010. An additional problem can arise if the arrival time of the TiSa with respect to the FEL changes. The T_0 determination process was not repeated within the three hours of data acquisition, and considering that a temporary laser set-up at an accelerator-based light source is usually less stable than in a laboratory under optimized conditions, it seems not unlikely that the arrival time of the TiSa pulses may fluctuate 0.5-1 ps within three hours. This makes it very difficult to investigate systematic differences between different delays, and no delay-dependent electron angular distributions could be extracted from this set of data.

However, upon closer inspection of Fig. 5.11, a difference between the two delay settings can be identified: when the TiSa pulse arrives before the FEL pulse, the maximum of the photoline at around $r = 150$ is slightly decreased, and a small rise in the region around $r = 110 - 140$ can be detected. An explanation for this could be a change in the Br($2p_{3/2}$) binding energy after the ionization by the TiSa laser. For comparison, the krypton ($2p_{3/2}$) binding energy is 1678 eV for the neutral atom [31] but 1690 and 1704 eV for the singly and doubly ionized atom, respectively [176], which corresponds to an increase of 0.7 and 1.5 %, respectively. Bromine is only 1 amu lighter than krypton, thus these ratios can be considered for a rough estimate. For an isolated Br($2p_{3/2}$) with a ground state binding energy of 1550 eV, this would

result in binding energies of 1561 and 1574 eV for the singly and doubly charged atom, respectively. As the photon energy is only 1570 eV this would mean that the ionization of an isolated Br^+ results in photoelectrons with only 9 eV and Br^{++} could not be ionized at all.

As the arrival time of the TiSa laser sometimes experienced random 'jumps' by about 1 ns or more during the experiment, it was necessary to re-calibrate T_0 after recording of the three data sets described above. The second calibration measurement is shown in Fig. 5.10(b). In comparison with Fig. 5.10(a) it can be seen that two delay-stage settings correspond to TiSa pulses arriving after the FEL and one to the TiSa pulse arriving before the FEL. The averaged red curve from Fig. 5.10(a) that was defined as T_0 is not reproduced here, but it is assumed to be centered between the two settings resulting in the blue and the green curve in Fig. 5.10(b). In the following, five different pump-probe delays between 0 and 2.5 ps were recorded for vertical TiSa polarization and two delays for horizontal TiSa polarization, but no data was taken with the TiSa pulse arriving before the FEL pulse. As no delay-dependent effects in the Br($2p$) photoelectrons are expected when the TiSa arrives after the FEL, and as no other delay-dependent signal was found, this second, larger data set is not shown.

6 Critical Discussion

This chapter discusses advantages and disadvantages of different experimental conditions in the view of the obtained results, and suggests potential improvements for future experiments aimed at retrieving time-dependent information on changing molecular geometries with photoelectron diffraction.

6.1 Electron Energy and Initial State

For a given molecule, the molecular-frame photoelectron angular distribution is determined by the initial electronic state, the light polarization and the final photoelectron kinetic energy. It is difficult to answer in general, which energy and which initial state are the "best" choices for imaging molecular structure with photoelectron diffraction, as this depends, for example, on the geometry of the molecule, the electron detection set-up, the respective photoabsorbtion and elastic electron scattering cross sections, and the available photon energies. Nevertheless, some general remarks can be made that could help planning a future experiment with an experimental set-up similar to the one presented in this work. The optimum electron energy and initial state are first considered from the viewpoint of the laboratory frame and the molecular frame respectively, and finally in the light of available theoretical approaches.

6.1.1 From the Viewpoint of the Laboratory Frame

From an experimental point of view, in order to obtain clean information on photoelectron angular distributions, it should be taken care that the photoelectron signal is separated as good as possible from all other electrons that contribute to the image on the detector. The presented data on two model systems, dibromobenzene and pFAB with 12 and 14 atoms, respectively, demonstrate that inner-shell ionization of polyatomic molecules creates a considerable amount of secondary electrons. These result from shake-off, shake-up or inelastic intra-molecular scattering events, and have a continuous energy spectrum that has a maximum at zero energy and decreases slowly towards higher energies, see Fig. 4.19. Moreover, above-threshold or strong-field ionization of a laser pump-pulse may create electrons with energies of 20 eV or more, see Fig. 5.11. This sets a lower limit to the applicable photoelectron kinetic energy. For the pFAB data in chapter 4, the separation was achieved

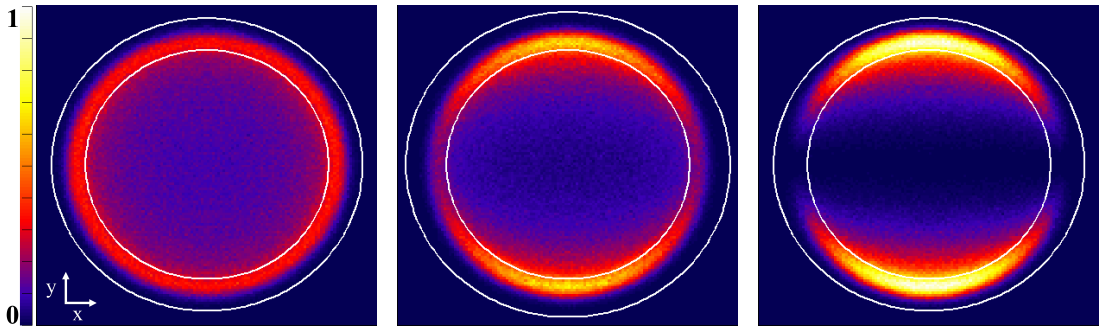

(a) $\beta = 0.0$ (b) $\beta = 1.0$ (c) $\beta = 2.0$

Figure 6.1: Simulated photoelectron distributions with different asymmetry parameters β, projected onto a two-dimensional detector. The light polarization direction lies along y.

reasonably well, although increasing the photoelectron energy by some ten eV probably would have helped to accomplish a cleaner distinction. In the dibromobenzene experiment in chapter 5 however, the photoelectrons with 20 eV kinetic energy were hardly distinguishable from the low-energy electrons. Here, higher kinetic energies would surely have been beneficial, but the spectrometer could not be operated at higher voltages at the time, thus limiting the maximum kinetic energy of the electrons that could be collected in full solid angle.

Moreover, Auger electrons are created after inner-shell ionization. For light elements such as fluorine and carbon, they have kinetic energies of several hundred electron volts [31]. In the presented data on pFAB, they were thus only collected in a small solid angle, creating a small background everywhere on the detector that has an isotropic angular distribution. For heavier elements with $Z \geq 20$ on the other hand, for example for bromine, MNN-Auger electrons can have energies below 100 eV, thus creating a significant background in the radial region of the photoelectron line at 20 eV kinetic energy, see Fig. 5.11. These considerations imply that either the photoelectron kinetic energy has to be chosen far away from all Auger lines, or, alternatively, the Auger electrons could be captured in the complete solid angle. In this case, an inversion of the image would allow to separate the contributions with different kinetic energies, see section 3.2.5. The choice of the photoelectron energy may however be limited by the energy acceptance of the spectrometer and by the decreasing photoionization cross sections for energies high above the threshold, as well as by the available photon energies that determine the achievable photoelectron kinetic energy for a given atomic level.

For the data shown here that contain only one photoline, the inversion did not yield a notable advantage and might even introduce artifacts due to the continuous distribution of low-energy electrons that may not be fitted well by the basis functions used in the *pBasex* algorithm [143]. It is thus desirable to separate the photoelectrons from the low-energy continuum as good as possible in the projected detector image. This separability is not only influenced by the photoelectron kinetic energy,

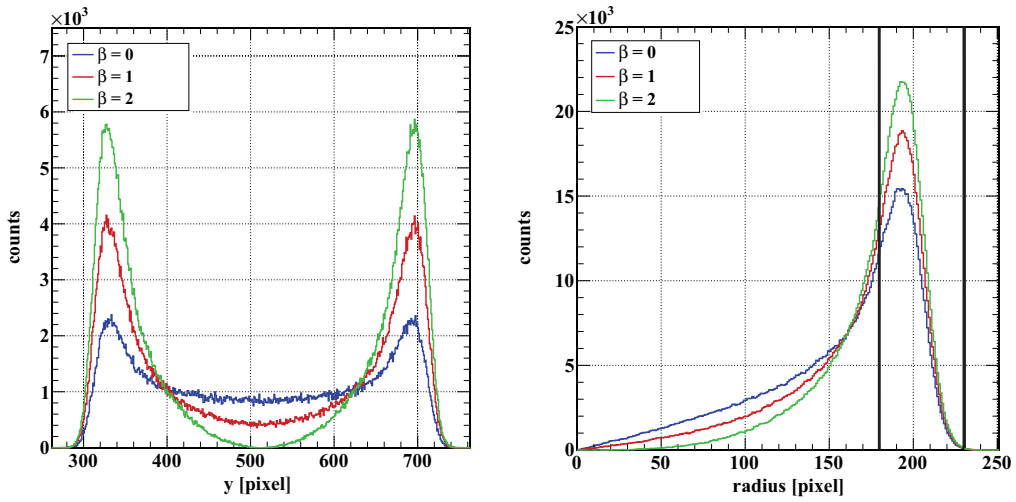

(a) (b)

Figure 6.2: (a) Cuts parallel to the y axis through the center of the images in Fig. 6.1. (b) Radial projections of the images in Fig. 6.1, see also section 3.2.4. The simulated electron kinetic energy has a Gaussian distribution centered at r = 200 pixels with a width of $\sigma_r = 5$ pixels.

but also by the initial electronic state, which affects the shape of the initial photoelectron wave. To illustrate this, Fig. 6.1 shows projections of three-dimensional photoelectron distributions onto a two-dimensional detector for different asymmetry parameters β, see Eq. 2.5. For all cases, a large fraction of the photoelectron intensity is contained in the rim of the projected photoline, close to the maximum radius on the detector, but this fraction varies depending on the asymmetry of the photoelectron wave. This is further elucidated by plotting cuts parallel to the y axis, through the center of the images, as shown in Fig. 6.2(a), and by projecting the electron intensity to the radius on the detector, as shown in Fig. 6.2(b). The center of the image contains less intensity for distributions with larger asymmetry.

A typical radial region of interest for the evaluation of the polar angular distribution of the photoelectrons is depicted in Fig. 6.1 by the white circles and in Fig. 6.2(b) by the black lines. The range of $180 \leq r \leq 230$ defines an azimuth opening angle of $\pm 26°$ for the central energy corresponding to r = 200 pixels. This radial region contains 43 % of the total intensity for $\beta = 0$, 52 % of the intensity for $\beta = 1$ and 60 % of the electrons for $\beta = 2$. In this sense, an angular distribution with a large asymmetry is favorable in order to better separate photoelectrons from low-energy electrons in the projected detector image. The largest anisotropy can be achieved by ionization of an s-orbital by linearly polarized light, which is the only case for which a pure p-wave is created (for atoms), see section 2.2. In general, all other cases result in a less anisotropic photoelectron wave. This difference can be seen when comparing the photoline resulting from F($1s$) photoionization of pFAB in Fig. 4.10(a), to the Br($2p$) photoline of DBB in Fig. 5.5(a), which shows an almost round laboratory-frame electron distribution.

6.1.2 From the Viewpoint of the Molecular Frame

The previous considerations referred to the experimental determination of the electron angular distribution in the laboratory frame. However, more importantly, the photoelectron energy also determines the molecular-frame photoelectron angular distribution for a given molecular geometry. In general, for higher electron kinetic energies more interference maxima and minima can arise, see Fig. 2.8(b). Moreover, the MFPAD of a more complicated molecule contains contributions of many atomic constituents and, thus, is more structured already at lower energies. This situation is further complicated by the fact that not all interference maxima that are present according to simple geometrical considerations can be observed experimentally. This becomes clear when taking into account that in directions with very little intensity of the initial wave, the intensity cannot be maximized by interference. It can be seen in Fig. 2.8(b) that independent of the energy, most intensity maxima are located at scattering angles in the range of 40° to 140°. If the p-wave is rotated parallel to the molecular axis, only little intensity of the direct wave can be found in this region due to the node at 90°, as can be seen in Fig. 2.9(b). For the case of 50 eV electrons, the maxima at 80° and 280° are strongly reduced. If enough statistics could be collected, these angles may however still be exploited, and for photoelectron holography on surfaces it has even been argued that more structural information can be obtained close to a node of the direct photoelectron wave [65, 52]. However, for the experiment on dilute, gas-phase pFAB molecules, three hours of data recording did not result in statistically significant intensity in the node of the photoelectron wave, as can be seen in Fig. 4.10.

One way to overcome this problem may be to use a more symmetric photoelectron wave. A spherical s-wave cannot be created exclusively in photoionization, but an approximately spherical wave can result from interference of different partial waves for certain initial electronic states and electron energies. For example, ionization of the Br($2p_{3/2}$) orbital in dibromobenzene at a photon energy of 1570 eV results in an almost spherical wave, see Fig. 5.5. However, this adds an additional level of complexity to the interpretation of the resulting photoelectron angular distribution, as theoretical calculations that involve different partial waves are challenging and appropriate photon energies may not be easy to identify. Alternatively, for ionization of an s-orbital, the X-ray polarization direction can be rotated such that the molecular axis lies close to the node in the resulting p-wave. In this case, depicted in Fig. 2.9(d), only two of the six interference maxima for the case or 500 eV electrons are lost, however, in this configuration only very little intensity of the direct wave is emitted in the direction of the scatterer, resulting in very low scattered intensity.

A compromise can be to chose the light polarization direction neither parallel nor perpendicular, but at an intermediate angle to the molecular axis, for example at $\alpha = 45°$ as shown in Fig. 2.9(c). In this case, the interference structure is largely preserved, while at the same time more intensity of the direct wave is emitted in the direction of the scatterer. The angle between the axis and the light polariza-

tion could be tuned depending on the given electron angular distribution and the scattering probabilities. However, this geometry breaks the mirror symmetry of the experiment. On one hand, this is an advantage, as in this case the two nodes in the direct wave suppress different interference maxima, such that for the case of a mirror symmetric molecule the information that is lost at an angle ϕ is preserved at ϕ+180°. On the other hand, this complicates the experimental set-up: in order to be able to interpret the projected photoelectron angular distribution on the detector, the molecular axis and the light polarization direction should both lie in the detector plane. For an experiment on laser-aligned molecules, this requires the detector plane to be perpendicular to the light propagation direction, thus the X-ray and the alignment laser would have to penetrate through a hole in the detector. The photoelectron angular distributions of oriented pFAB molecules in Fig. 4.15 have been recorded at an angle of 45° between the light polarization direction and the molecular axis, but here the molecular axis was rotated out of the detector plane. It is thus difficult to judge from the projected distribution whether the angular distribution in the plane of the molecule shows more structure. Moreover, when the electric field of the spectrometer is used to induce the orientation, the molecules cannot be oriented while being aligned parallel to the detector surface.

In summary, there is no simple answer to the question which photoelectron kinetic energy produces the "best" molecular-frame photoelectron angular distribution under experimental conditions. Preferably, the angular positions of interference maxima in the MFPAD should be located neither at the minimum nor at the maximum of the unscattered wave. To achieve this, it can be beneficial to chose an experimental geometry where the polarization direction is not parallel to the molecular axis or an initial wave that does not contain a node. In addition, when choosing the initial electronic state and the electron kinetic energy, the availability of a reliable theoretical model should be taken into account, as will be discussed in the following.

6.1.3 Theoretical Modeling of MFPADs

Ideally, the molecular structure would be directly reconstructed from the recorded data, for example by interpreting them as a hologram [66, 64]. It has been suggested that this can be achieved for gas-phase molecules [59] when using high-energy photoelectrons. From a theoretical point of view, it would thus be beneficial to use high electron energies for the photoelectron diffraction experiment, for which multiple scattering events can be neglected and scattering can be described within the first Born approximation, see section 2.3.2. However, for several reasons that have been discussed in the previous paragraphs, very high electron energies may not be achievable or desirable from an experimental point of view. Therefore, an important open question is, at which electron energies the approximation of single scattering becomes valid. Up to now, suitable data sets were missing that would allow for a systematic comparison between experimental results and theoretical predictions over a wide energy range, especially for high energies, and for different molecules.

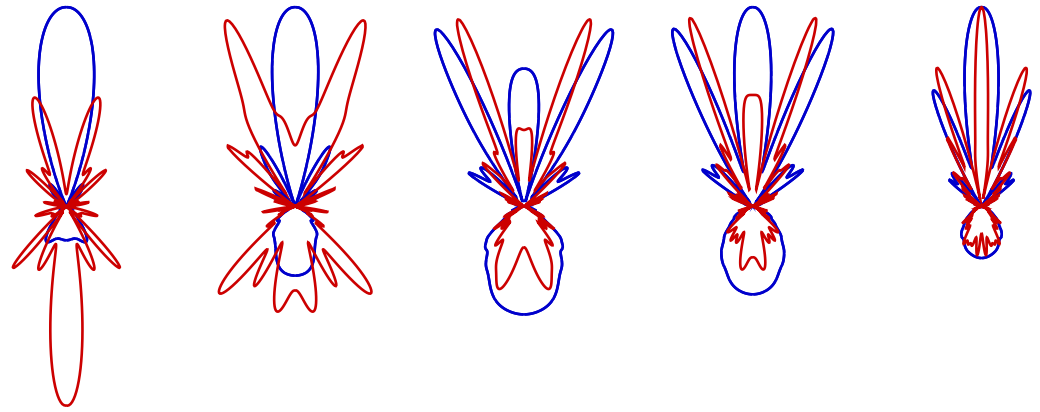

(a) 100 eV (b) 200 eV (c) 300 eV (d) 400 eV (e) 500 eV

Figure 6.3: Comparison of MFPADs for perfectly three-dimensionally oriented pFAB molecules, calculated within the first Born approximation (blue) and with density functional theory (red) for different kinetic energies of the photoelectron. The fluorine atom points towards the bottom. The distributions are normalized to the same maximum.

The validity of the first Born approximation for lower energies can however be tested by investigating in which energy regime density functional theory converges to the same results. DFT can be regarded as a complementary theoretical approach, which takes into account the full molecular potential and is thus also suitable for lower electron energies, see section 2.3.3. The calculations for complex molecules and high electron energies can become computationally demanding, but it was found that nevertheless for pFAB molecules, calculations of up to 500 eV electron energy can be performed in a reasonable time frame. The resulting MFPADs for different electron kinetic energies between 100 and 500 eV are plotted in Fig. 6.3, together with results obtained with the single scattering model by Krasniqi *et al.* [59]. For the cases of 100 and 200 eV electrons, very little similarities can be seen for the different calculations. However, in the region from 300 to 500 eV, the distributions clearly start to look more alike. For the case of 500 eV electrons, the structure of the MFPADs is very similar, except for a small difference in the angular position of the maxima and the width of the most prominent peak. In general, the DFT calculations show some finer structure, especially for the highest energy, as compared to the single scattering results.

Neither the FEL nor the synchrotron data shown in this thesis are of a quality that allows unambiguous verification or falsification of a theoretical model, but the experimentally obtained difference photoelectron angular distributions of pFAB are well reproduced by DFT calculations, see Fig. 4.13. During the experiment at PETRA, several smaller molecules with five to eight atoms have also been investigated at multiple electron energies up to 250 eV. This data set is currently under analysis and will hopefully provide the basis for a systematic comparison between theory and experiment in the near future.

6.2 Fixing Molecules in Space

For the above considerations it has been implicitly assumed that molecular-frame photoelectron angular distributions could be measured for molecules that are perfectly fixed in all three spatial coordinates and 100 % oriented, but unfortunately this is not possible. This section discusses the influence of the finite molecular alignment on the photoelectron angular distributions and considers advantages and disadvantages of laser-alignment and electron-ion coincidence measurements.

6.2.1 Laser-Alignment of Molecules

Adiabatic laser-alignment confines the axes of the molecular ensemble to an approximately Gaussian distribution that is centered around the polarization direction of the alignment laser and has a standard deviation $(\sigma_\phi, \sigma_\theta)$, see section 2.4.1. ϕ and θ are the polar and azimuthal angle respectively, measured with respect to the alignment-laser polarization direction. Here, the Gaussian is assumed to be cylindrically symmetric, thus $\sigma_\phi = \sigma_\theta = \sigma$. The width σ determines the degree of alignment, $\langle\cos^2\theta_{2D}\rangle$, and can be characterized experimentally by monitoring ionic fragments that are emitted along the direction of the molecular axis, projected onto a two-dimensional detector, see Eq. 4.1. The relation between these two quantities can be obtained from simulating such projected distributions of fragment ions that result from a Gaussian axes distribution, and then calculating the alignment parameter for that image. Figure 6.4 shows simulations of such projections for different degrees of molecular alignment. The image in Fig. 6.4(a) corresponds to the value of $\langle\cos^2\theta_{2D}\rangle = 0.97$ that was reported for alignment of iodobenzene molecules in reference [155], whereas Figs. 6.4(b) and 6.4(c) illustrate the degree of alignment that was achieved for pFAB and dibromobenzene molecules in the data presented here.[1] It is obvious that in both experiments the alignment was not perfect. The relationship between the width σ and the alignment parameter $\langle\cos^2\theta_{2D}\rangle$ can be found in Tab. 6.1 and in Fig. 6.4(d). Small deviations from the ideal value of $\langle\cos^2\theta_{2D}\rangle = 1.0$ correspond to a fast increase in the width of the molecular axis distribution.

σ [°]	0	5	10	15	20	25	30	35	40	45
$\langle\cos^2\theta_{2D}\rangle$	1.00	0.99	0.97	0.94	0.89	0.84	0.79	0.74	0.69	0.65
σ [°]	50	55	60	65	70	75	80	85	90	95
$\langle\cos^2\theta_{2D}\rangle$	0.61	0.58	0.56	0.54	0.53	0.52	0.51	0.51	0.51	0.50

Table 6.1

[1] The shape of the projected ion distribution also depends on the kinetic energy of the ions. Here, a Gaussian radial distribution around a nominal radius R with a standard deviation of $\sigma_r = 0.05\,R$ has been assumed. The resulting values of $\langle\cos^2\theta_{2D}\rangle$ are independent of the choice of σ_r.

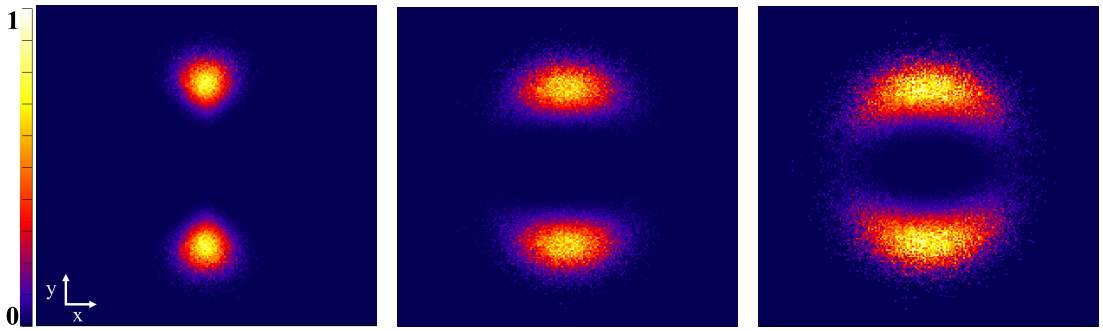

(a) $\langle\cos^2\theta_{2D}\rangle = 0.97$, $\sigma = 10°$ (b) $\langle\cos^2\theta_{2D}\rangle = 0.89$, $\sigma = 20°$ (c) $\langle\cos^2\theta_{2D}\rangle = 0.78$, $\sigma = 31°$

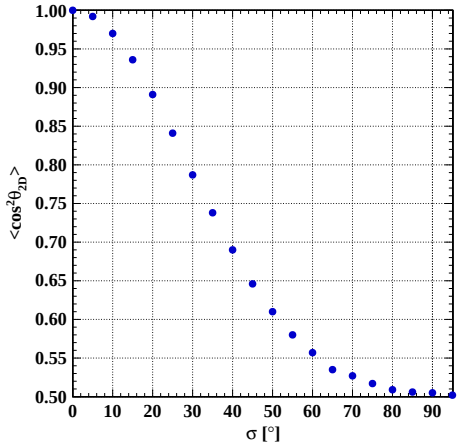

(d)

Figure 6.4: Top: Simulated ion distributions for molecular ensembles with different degrees of molecular alignment. The linear polarization of the alignment laser lies along y. All images contain the same number of ions and the kinetic energy is the same for all images. (b) is scaled by a factor of 2 and (c) is scaled by a factor of 4 with respect to (a). Bottom: Relation of the standard deviation σ of the Gaussian axes distribution to the alignment parameter $\langle\cos^2\theta_{2D}\rangle$.

The non-perfect molecular alignment results in an uncertainty in fixing the molecular frame with respect to the laboratory frame that directly influences the measurement of a molecular-frame photoelectron angular distribution. To illustrate this, the MFPADs of CO as obtained from the simple man's model in section 2.3.1 are averaged over a Gaussian distribution of angles between the molecular axis and the light polarization. For a linear molecule, the MFPAD is cylindrically symmetric, and it is sufficient to average over only one angle. The angle α in Eq. 2.12 is replaced by $\alpha' = \alpha + \alpha_{\mathrm{rdm}}$, where α_{rdm} has a Gaussian distribution with a standard deviation σ that determines the molecular alignment, see Tab. 6.1. The evolution of the photoelectron angular distributions in the molecular frame for different degrees of molecular alignment is shown in Fig. 6.5 for two different photoelectron energies. The top row shows PADs obtained from an initial s-wave. From Fig. 6.5(a) to Fig. 6.5(b), almost no change is observed for electrons of 50 eV kinetic energy, whereas the distribution for 500 eV electrons looks already very different from the

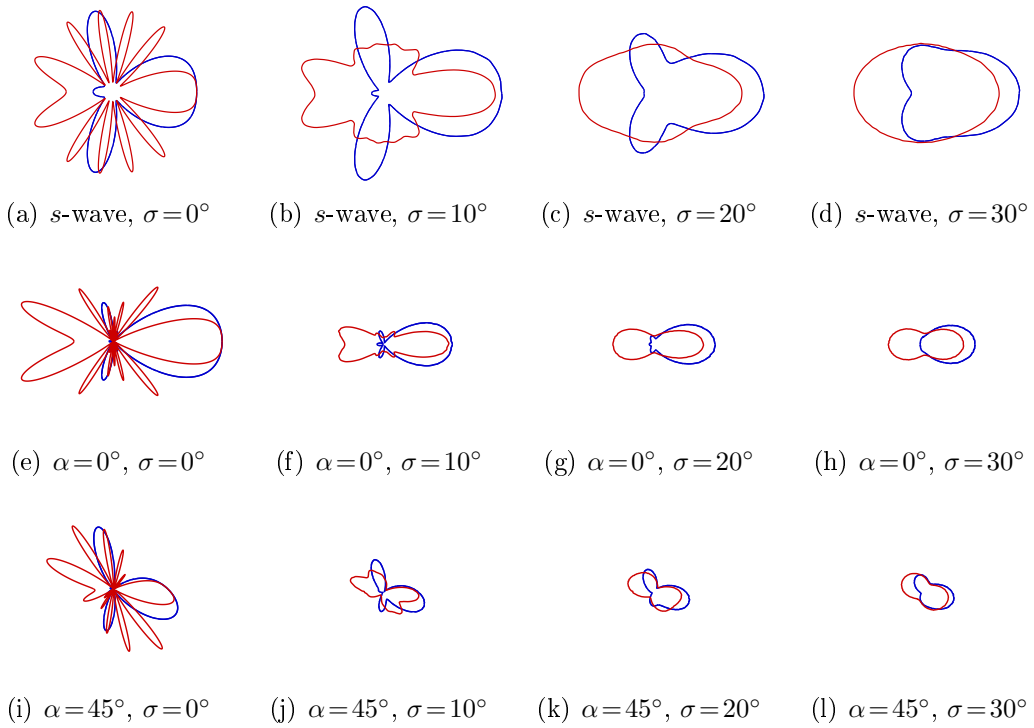

(a) s-wave, $\sigma = 0°$ (b) s-wave, $\sigma = 10°$ (c) s-wave, $\sigma = 20°$ (d) s-wave, $\sigma = 30°$

(e) $\alpha = 0°$, $\sigma = 0°$ (f) $\alpha = 0°$, $\sigma = 10°$ (g) $\alpha = 0°$, $\sigma = 20°$ (h) $\alpha = 0°$, $\sigma = 30°$

(i) $\alpha = 45°$, $\sigma = 0°$ (j) $\alpha = 45°$, $\sigma = 10°$ (k) $\alpha = 45°$, $\sigma = 20°$ (l) $\alpha = 45°$, $\sigma = 30°$

Figure 6.5: Simulated MFPADs for oriented CO molecules for different degrees of molecular alignment, given by the width of the Gaussian axes distribution, σ, and for different source waves. Top row: s-wave, bottom two rows: p-waves with different angles α between the light polarization direction and the molecular axis. Blue: 50 eV electron energy, red: 500 eV electron energy. All distributions are plotted on the same radial scale.

one for perfectly aligned molecules. The four maxima between 60 and 130° are almost inseparable. This can be explained by the fact that for 500 eV electrons, the spacing between two neighboring maxima is about 10°, as can be seen in Fig. 2.8(b). This corresponds to the standard deviation of the Gaussian axis distribution for this degree of alignment. When the degree of alignment is decreased further, the distributions in Figs. 6.5(c) and 6.5(d) arise. The two maxima in the PAD for 50 eV can still be distinguished, while the angular distribution of 500 eV electrons shows no clear structure.

The second row of Fig. 6.5 shows the PADs obtained from a p-shaped source wave when the light polarization direction is parallel to the molecular axis. It can be seen in Fig. 6.5(f) that due to the node in the direct wave, the intensity maxima are already small for a degree of alignment of $\langle \cos^2\theta_{2D} \rangle = 0.97$. When the alignment is decreased further, see Figs. 6.5(g) and 6.5(h), all structure disappears. When the light polarization direction is rotated by 45°, as depicted in the bottom row of Fig. 6.5, much more structure can be seen for all degrees of alignment. Even for the case of $\langle \cos^2\theta_{2D} \rangle = 0.79$, in Fig. 6.5(l), the 50 eV electrons still show one maximum in the upper left corner that would be sufficient for the retrieval of the CO bond length.

Even from these very simple calculations for a diatomic molecule, it becomes clear that the quality of the laser-alignment is of great importance for recording molecular-frame photoelectron angular distributions. In general, measuring MFPADs with finer structure requires better alignment, thus higher electron energies or more atoms in the molecule complicate the situation. As a rule of thumb, it can be stated that the molecular axes need to be fixed with at least the same precision that is required for resolving the individual maxima of the MFPAD. In other words, if the MFPAD contains maxima that are spaced more closely than 10°, it is not possible to resolve them in an experiment on laser-aligned molecules with the degree of alignment that was achieved up to now. However, a degree of alignment of about $\langle\cos^2\theta_{2D}\rangle = 0.97$ should be sufficient to resolve photoelectron angular distributions that contain structural information about the molecule, if the individual maxima in the electron angular distribution are not too close. A possibility to improve the degree of molecular alignment can be to employ electron-ion coincidence measurements, as discussed in the following paragraph.

6.2.2 Electron-Ion Coincidence Experiments

Instead of actively aligning the molecules in space, their orientation can, in certain cases, be determined in retrospect by recording the momentum vector of one or more characteristic ionic fragments in coincidence with the photoelectron, see section 4.1. An advantage of this method is that any alignment geometry with respect to the detector plane and the light polarization can be chosen. Moreover, the molecules are automatically not only aligned, but oriented, provided that the recorded fragment is unique. For three-dimensional orientation, three-fold coincidences between the photoelectron and two characteristic ionic fragments would be required. Disadvantages of the coincidence method can be that a suitable fragment to fix the molecular frame to the laboratory frame may not exist, especially not for large molecules, and that it can be challenging to collect sufficient data in the time frame of one experiment. This paragraph shortly discusses both requirements.

The determination of the molecular frame based on an ionic fragment requires that its momentum vector reflects the direction of the molecular axis at the time of the photoionization. This implies that the molecule has to dissociate fast, such that no rotation occurs before the ion has left the molecule, which is referred to as *axial recoil approximation* [149, 150]. Moreover, if more than two charged fragments are created in the break-up of the molecule, which can easily happen after inner-shell ionization, the momentum of the ionic fragments is determined by the three-body Coulomb repulsion, and is thus not necessarily directed along the initial bond direction. The PIPICO map of pFAB in Fig. 4.3 reveals that all fragmentation channels involving F^+ ions exhibit rather broad lines (except for the two-body break-up), suggesting that fluorine ions mostly result from break-up channels that involve more than two charged fragments. The emission direction of the fluorine atom may thus not

strictly reflect the direction of the F-C axis.[2] Furthermore, no rearrangement of the molecular structure must take place during the dissociation, in order for the above assumption to be valid, which is not always fulfilled. For example, it was shown in section 4.1 that some ionic fragments are created in the dissociation of pFAB molecules which can only occur if rearrangement of hydrogen atoms takes place during the dissociation.

If a fragment ion can be identified that defines the direction of the molecular axis, a very high degree of molecular alignment can in principle be achieved with the coincidence technique when narrowing the condition on the ion momentum. A major practical limitation is however the amount of statistics that can be collected in this way. If 95% of the shots shall contain only one photoionization, the mean number of ionization events per shot needs to be smaller than 0.35 according to Poisson statistics [177]. Assuming a typical detection efficiency of about 50%, this means that the mean number of detected photoelectrons should be smaller than 0.17. In addition, this electron needs to be recorded in coincidence with the fragment ion that defines the molecular frame. Depending on the fragmentation channels, this can considerably reduce the number of usable events. For large molecules, a variety of fragmentation channels exists, as is illustrated by the PIPICO map for pFAB in Fig. 4.3, and only few of them may result in the desired, characteristic ionic fragment that can provide the information about the orientation of the molecule. For the pFAB experiment at PETRA, only 1.5% of the detected electrons were recorded in coincidence with an F^+ ion.

To collect sufficient data is especially challenging if the experiment is carried out at a Free-Electron Laser. At the moment, the highest repetition rate available at an FEL is the multi-bunch mode of FLASH [178] that currently achieves an effective repetition rate of 1 kHz. Here, a mean number of 0.17 electrons per readout cycle corresponds to a maximum electron count rate of 170 Hz. For pFAB, only 1.5% of the electrons were detected in coincidence with F^+, which would result in a usable count rate of 2.5 Hz.[3] These photoelectrons stem from ionization of a randomly oriented molecular ensemble. If only molecules are selected that are aligned within a 10° opening angle around an arbitrary axis, the number of electron counts is decreased by another factor of $\sim 10^{-3}$, to 0.0025 Hz. For comparison, in the presented LCLS experiments with laser aligned molecules, the mean number of electron hits per shot was 300 in the dibromobenzene experiment and 140 in the pFAB experiment. Assuming that about half of those are photoelectrons, and considering that the YAG alignment laser operates at 30 Hz, this corresponds to a photoelectron count rate of 4.5 and 2.1 kHz, for pFAB and DBB respectively. This is about six orders of magnitude larger than what can currently be achieved

[2] However, the fact that fluorine fragments from laser-aligned pFAB are confined to the polarization direction of the alignment laser implies that a certain relation of the emission direction to the molecular axis is preserved.

[3] Note that FLASH does not provide photons with energies that are high enough to ionize the F($1s$) level.

in a coincidence mode. When using a different molecule with a more favorable fragmentation, at most about one order of magnitude can be gained. Once the *European XFEL* starts operation at a repetition rate of 27 kHz, the statistics could be increased by a factor of 30. Another interesting possibility would be to combine laser-alignment with a coincidence measurement to increase the number of molecules that are aligned along a given axis. This could be achieved by using the 1 kHz multi-bunch mode of the TiSa available at FLASH for nonadiabatic alignment. Nevertheless, the collection of enough data in a photoelectron-photoion coincidence experiment will remain very challenging.

6.3 Pump-Probe Experiments

Once good experimental conditions for the static measurements have been found, the goal is to record molecular-frame photoelectron angular distributions of changing molecular geometries. To this end, it is necessary to trigger a reaction, and the best way to do this highly depends on the particular reaction to be studied. Here, only photochemical reactions are considered that can be triggered with a short-pulsed laser.

In this work, an 800 nm titanium:sapphire laser pulse has been used that populates various excited and valence-ionized states of dibromobenzene, among them dissociative states. However, the absorption of a single photon, with an energy that is tuned to an electronic transition would be better suited to trigger a specific reaction in a given molecule. For example, the absorption of a single UV photon in pFAB is expected to dissociate the molecule via one or a few pathways that proceed through transition states, see chapter 7. Another complication of a pumping step that is based on multi-photon processes is the strong dependence on the laser intensity. Small fluctuations can significantly change the electron spectrum, as was shown in Fig. 5.11, and possibly also the relative population of different fragmentation channels. This requires a laser set-up that can provide a very stable intensity over an extended period of time. Moreover, multi-photon processes can be sensitive to the orientation of the molecule with respect to the laser polarization direction. Dibromobenzene molecules that are aligned parallel to the TiSa polarization are ionized more strongly than molecules aligned perpendicular to that axis, as has been shown in Fig. 5.2. This may be exploited to pump aligned molecules more efficiently, but it may also interfere with other experimental requirements. Furthermore, averaging over intensities in different regions of the laser focus cannot be avoided.

Another difficulty in pump-probe photoelectron diffraction experiments is the fact that the binding energy of a core level can increase considerably when a (valence) electron is removed from the molecule, see also section 5.2.4. This has implications for pump-probe experiments in which an ionized molecule is created in the pumping step. The energy of the photoelectron is decreased, for example by about 10 eV for the Br($2p$) level after the ionization. The MFPAD of the ionized molecule may

thus be altered, not because of changing molecular structure but simply due to the different electron kinetic energy. It was shown for pFAB molecules that a 10 eV change in the photon energy, corresponding to a 10 eV change in electron kinetic energy, changes the difference photoelectron angular distribution considerably, see Fig. 4.13. Furthermore, the evaluation of difference images between data recorded with the pump pulse arriving before and after the probe pulse cannot be easily interpreted because the radius of the photoline on the detector changes. A way to overcome this problem is to take as a reference not the distribution for negative time-delays, but the MFPAD that occurs at zero time delay, directly after the ionization took place but before nuclear motion starts, but this requires a very good temporal resolution. A second possibility is to trigger a photochemical reaction in which the molecule remains neutral. This may however be difficult to achieve, and complications can arise from the fact that the neutral fragments cannot be detected easily before probing them by a second pulse.

Finally, it has to be taken into account that in an experiment on adiabatically laser-aligned molecules, the pump as well as the probe process takes place in the presence of an additional, strong electric field of the alignment laser. It was demonstrated in sections 4.4 and 5.1 that this can alter the fragmentation of the molecule and cause multi-color effects, also in the photoelectrons. A possibility to avoid this is to use field-free alignment, see section 2.4.4. In general, the degree of molecular alignment that can be achieved with this method is however significantly lower than for adiabatic alignment [110]. Considering that a high degree of alignment is crucial for the photoelectron diffraction approach, as was discussed in section 6.2, impulsive alignment does not appear to be an attractive alternative at the moment.

7 Conclusion

The objective of this thesis was to investigate the possibility of imaging molecular structure by recording photoelectron angular distributions of polyatomic, fixed-in-space molecules. The goal of recording a *molecular movie* with photoelectron diffraction is certainly not yet achieved, and the discussion in the previous chapter makes clear that several questions remain only partly answered. Nevertheless, important insight is gained from the studies presented here. Most of the difficulties that prevented, up to now, the recording of a delay-dependent photoelectron angular distribution were particular to the experiments described in this work and may be avoided in the future, although even with careful preparation, a temporary experimental set-up at an accelerator-based light source always bears the risk to encounter instabilities and unforeseen problems.

Ensembles of gas-phase 1-ethynyl-4-fluorobenzene (pFAB) molecules were adiabatically laser-aligned and mixed-field oriented, and the angular distributions of photoelectrons resulting from ionization of the fluorine 1s level by an ~ 80 fs X-ray pulse were recorded for five different photoelectron energies between 30 and 60 eV. Despite the fact that a significant amount of molecular clusters were present in the molecular beam, a clear dependence of the difference photoelectron angular distribution on the electron energy and the molecular orientation can be observed that is well reproduced by density functional theory calculations. The inter-atomic distances in pFAB range from 1.2 to 7.6 Å, and the chosen electron energies correspond to wavelengths of 1.6 to 2.2 Å, thus an interpretation of this effect in terms of intra-molecular scattering of the photoelectron wave is suggested. Interference effects depend on the wavelength, as well as on the geometry of the scattering object, thus the change of the angular distribution for decreasing wavelengths gives an indication for changes that could be expected when a molecule with increasing internuclear distances is imaged at a fixed wavelength. In this sense, the results of this experiment indicate that photoelectron diffraction is sensitive to the molecular structure, and may be interpreted as 'freeze frames' of a molecular movie, taken with an X-ray FEL.

In a second step, it was investigated to what extent this technique can be utilized to record snapshots of changing molecular structure by evaluating data from an IR-pump, X-ray-probe experiment on laser-aligned 1,4-dibromobenzene (DBB) molecules. Here, an 800 nm laser pulse was used to dissociate the molecules before the Br($2p_{3/2}$) level was ionized by the X-ray pulse, resulting in photoelectrons of 20 eV kinetic energy. Although the effect of the molecular alignment on the photoelectron angular distribution can also be observed in the presence of all three light pulses, no dependence of this signal on the delay between the laser pulse and the

X-ray pulse is found. Reasons for this are the temporal resolution of the experiment that was limited to about 300 fs due to the arrival time jitter between the laser pump and the X-ray probe pulse, the comparably low degree of molecular alignment, and the fact that only one data set could be recorded for which the pump pulse arrived at the target significantly earlier than the probe pulse.

Both experiments involving adiabatically laser-aligned molecules demonstrate that the alignment laser pulse significantly influences the fragmentation of the molecule in the pumping and the probing steps, and can also affect the photoelectrons due to two-color effects. Alternatively, the molecules can be fixed in space by the photoelectron-photoion coincidence technique. Photoelectron angular distributions from ionization of the fluorine 1*s* level in pFAB were recorded in coincidence with F^+ ions. When the fluorine ions are emitted in opposite directions, the electron angular distributions are mirror images of each other, however, they look similar to the distribution measured for randomly oriented molecules. The photoion-photoion coincidence map illustrates that many fragmentation channels exist, and that only few of them involve the emission of an F^+ ion. These channels exhibit rather broad lines in the PIPICO map, indicating that more than two charged fragments have been created.

All experiments reveal that recording a molecular-frame photoelectron angular distribution of a polyatomic molecule is challenging, with the major issue being to align the molecules accurately in space. A degree of alignment of $\langle\cos^2\theta_{2D}\rangle = 0.97$ is expected to improve the angular resolution of the photoelectron angular distribution significantly, and has already been successfully demonstrated for adiabatically laser-aligned, state-selected iodobenzene molecules [155]. Although the coincidence method can, in principle, achieve a high degree of alignment, the fragment ions are not always strictly emitted along the direction of the molecular bond, for example if more than two charged fragments are created, or when structural rearrangement takes place during the dissociation, setting a principle limit to the achievable alignment. Imaging a changing molecular structure, for example during an isomerization reaction, is only possible with this method if the marker atom does not move. Moreover, the variety of fragmentation channels for molecules that contain more than a few atoms can make it difficult to find ionic fragments that are suitable to fix the molecule in space. In contrast, the laser-alignment technique is applicable to all molecules with an anisotropic polarizability, and moreover offers the possibility of aligning the molecules in three dimensions without losing many of the events. However, in this case the contributions of all different fragmentation channels are summed up. Moreover, the molecular alignment may be influenced if the polarizability of the molecule changes during the reaction.

When designing a future photoelectron diffraction experiment, several choices should be carefully considered. The optimum photon energy and the electron initial state which determine the energy and the shape of the initial photoelectron wave depend on the particular molecule and reaction to be studied. In general, the energy should be high enough to separate the photoelectrons from low-energy electrons.

Increasing the electron energy up to a regime where the scattering can be described within the first Born approximation would significantly simplify the interpretation and the theoretical prediction of photoelectron angular distributions. Comparison of density functional theory calculations and calculation within the first Born approximation indicate that this regime may already be reached for energies of a few hundred eV. By now, photoelectron angular distributions have been recorded for several molecules with kinetic energies as high as 250 eV with a very similar experimental set-up at the PETRA synchrotron facility, which should enable a systematic comparison between data and different theoretical predictions. Benchmarking a theory which can make reliable predictions of experimental photoelectron angular distributions of polyatomic molecules would tremendously help to identify the optimum experimental conditions in advance of an experiment. Moreover, it may be beneficial to change the set-up such that the alignment direction of the molecule can be rotated within the detector plane. In addition, using a more symmetric initial wave circumvents the problem of information loss due to the node in the initial wave, however, the theoretical description of the superposition of different partial waves is generally more complicated.

In general, a stable experimental set-up and a good control of all experimental parameters is crucial, especially in a pump-probe experiment aiming at imaging changing molecular structure. The molecular beam should be well characterized, to ensure that the molecules are rotationally cold and preferably state-selected, and that no molecular clusters are created. The properties of the laser pulse and the FEL pulse have to be well controlled, or, if this is not possible, be recorded on a shot-to-shot basis. The arrival time jitter between laser-pump and X-ray-probe pulse that limited the temporal resolution to about 300 fs in 2010 can now be corrected for by employing cross-correlation techniques [173, 174, 172]. Moreover, the pulse durations of FEL and laser pulse are constantly shortened and should enable an overall temporal resolution of about 10 fs in the near future. Furthermore, the intensities of table-top X-ray sources exploiting high-harmonic generation continuously increase, thus they may soon become an attractive alternative to experiments at accelerator based lightsources, avoiding the problem of the arrival time jitter between pump and probe pulses. Triggering a photochemical reaction with a single photon, for example in the UV range, with an energy tuned to a specific transition is expected to have several advantages over using a multi-photon process. Fewer excess electrons are created, the process is less sensitive to small fluctuations in the laser intensity, and ideally the molecule remains neutral which facilitates the comparison to photoelectrons from molecules in the ground state.

To illustrate the results that may be expected in a successful time-resolved photoelectron diffraction experiment, Fig. 7.1 shows calculated molecular-frame photoelectron angular distributions for different molecular geometries of pFAB which are predicted to occur within less than 1 ps after photoexcitation by a UV pho-

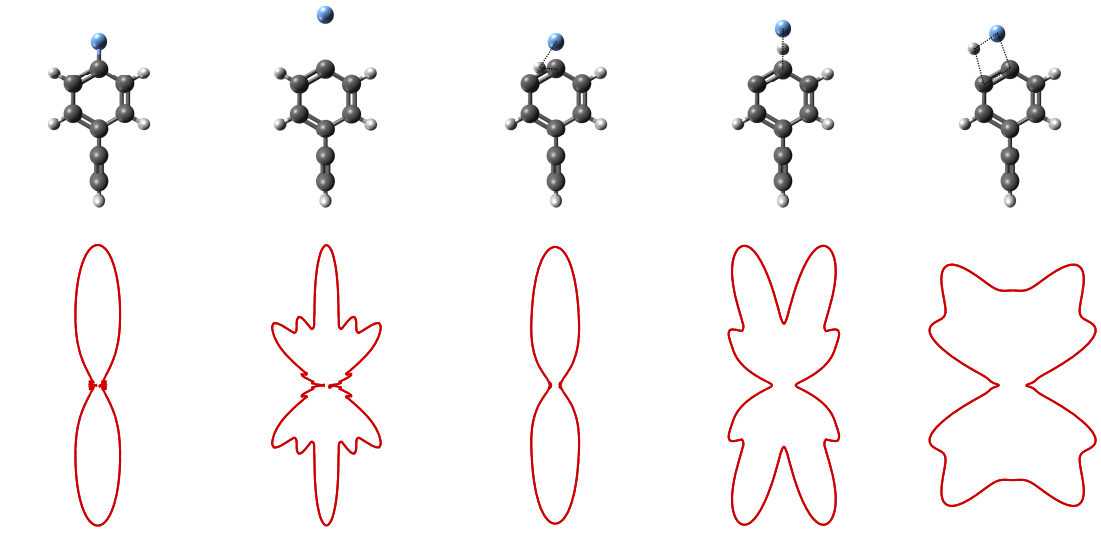

(a) equilibrium (b) doubled F-C bond length (c) transition state 2 (d) transition state 3 (e) transition state 4

Figure 7.1: Photoelectron angular distributions of perfectly one-dimensionally aligned pFAB molecules with different intermediate geometries, obtained from DFT calculations at a photoelectron kinetic energy of 35 eV. Transition state 2 is followed by transition state 3, see also Fig. 1.2(b). The fluorine and the hydrogen atom are located out of the molecular plane in (c) and (d), and the benzene ring is slightly distorted [179, 180].

ton [4, 145, 179, 180], see also Fig. 1.2(b)[1]. The resulting MFPADs are clearly different when the molecules are perfectly aligned, suggesting that it could be possible to image the reaction pathway through one of these intermediate geometries in a UV-pump, FEL-probe experiment even with non-perfect molecular alignment. However, a transition state is by no means a static geometry in which the molecule remains, but a saddle point in the reaction coordinate through which the change in molecular structure proceeds, often very fast. Moreover, the molecular wave packet may spread out considerably, such that several different intermediate geometries are populated at the same time, which could not be distinguished even if the experiment had an infinitely good temporal resolution. It is therefore not obvious, whether it would be possible to directly image the different predicted transition states, but for certain cases it may be possible to distinguish different pathways.

In summary, if the above discussed problems can be overcome, time-resolved photoelectron diffraction and holography can offer a complementary approach to time-resolved X-ray and electron diffraction. It holds the potential to image the geometric structure of gas-phase molecules with few-femtosecond temporal and sub-Ångström spatial resolution, at photon energies only a few hundred eV above a given inner-shell threshold. Using electrons as opposed to X-rays for imaging has the advantage of much higher elastic scattering cross sections, which is particularly

[1] Transition state 4 is referred to as transition state 1 in Fig. 1.2(b) that is taken from reference [4].

important for targets containing lighter atoms such as carbon, nitrogen, or oxygen that do not scatter X-rays efficiently. Using photoelectrons instead of an electron beam has the additional benefit of avoiding the problem of velocity mismatch in laser-pump electron-probe experiments on gas-phase targets. Due to the element specificity of X-ray photoionization it is possible to launch the photoelectron wave from a specific atom within an extended molecule, offering the opportunity to create a localized source and to image only the local environment of the emitter. An upcoming experiment at FLASH as well as a proposal for a future LCLS experiment aim at recording time-resolved photoelectron angular distributions, implementing the insights obtained in this work.

A Appendix

A.1 Estimate of the Number of pFAB Clusters

The time-of-flight spectrum of pFAB recorded during the LCLS experiment contained a large, broad parent ion peak, as well as a broad peak of singly ionized pFAB dimers and dimers that miss a fluorine atom, as shown in Figure 4.7. These ions are attributed to the presence of molecular clusters, and the fact that these peaks are broad demonstrates that the ions possess kinetic energy and, thus, are probably created from break-up of trimers or larger clusters. These clusters are, most likely, not aligned by the YAG laser pulse, which is of particular importance for the analysis of photoelectron angular distributions of aligned molecules. The recorded ion data do not provide an unambiguous way of determining the ratio of isolated molecules and molecules in clusters in the molecular beam, but several hints are taken into consideration to provide a rough estimate.

Figures A.1(a) and A.1(b) show typical distributions of F^+ fragments on the ion detector after ionization of pFAB by the LCLS pulse, recorded with and without the YAG alignment laser. Both images contain the same number of events. It is obvious that additional F^+ ions are created when the YAG laser is added, which have a lower kinetic energy and are isotropically distributed, in contrast to the ions with higher kinetic energy that are emitted along the YAG laser polarization direction. It was shown in reference [181] that the kinetic energy of iodine fragments created by UV absorption of iodomethane molecules decreases when two to three molecules are bound in a molecular cluster, and that their angular distribution becomes more isotropic as compared to single molecules, which is attributed to collisions of the iodine ion within the cluster. This suggests that in the present case, the additional ions result from ionization of excited, randomly oriented pFAB molecules by the YAG pulse that are bound in a molecular cluster.

To estimate the degree of alignment that was achieved for single molecules, the low-energy peak that is superimposed with the signal of aligned molecules is removed from the image. The central peak can be fitted by a two-dimensional Lorentz distribution, and then be subtracted, resulting in the distribution in Fig. A.1(c). These ion images not only enable the determination of the degree of alignment, but also provide limited information about the fraction of unaligned clusters in the molecular beam. When assuming that the additional, low-energy ions with an isotropic distribution originate from unaligned molecular clusters, the ratio

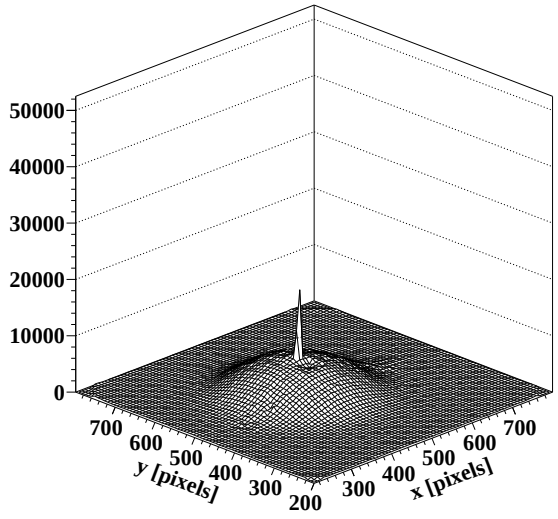

(a) without YAG

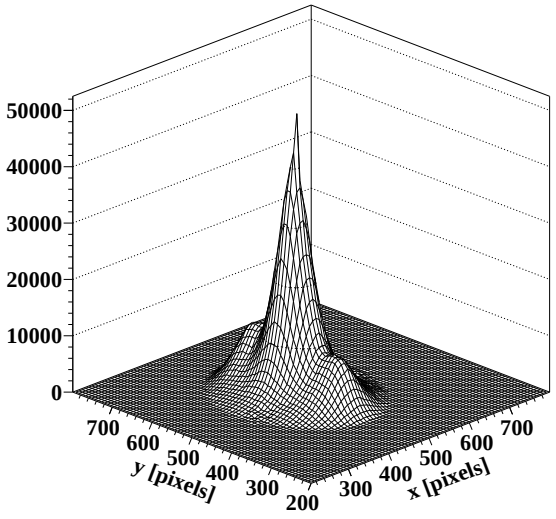

(b) with YAG

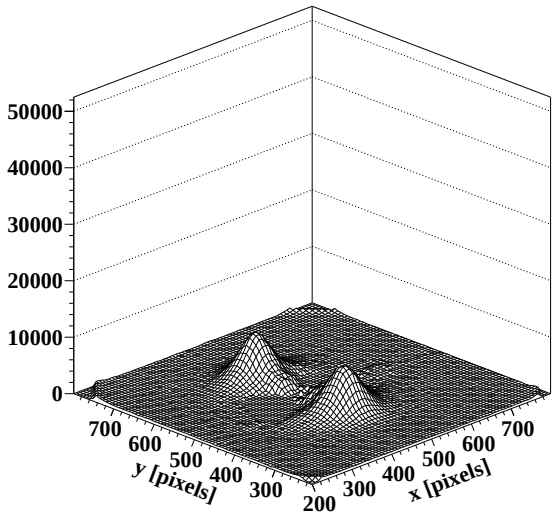

(c) A.1(b) with 2d Lorentz fit subtracted

Figure A.1: Ion detector images for ionization of pFAB molecules by the LCLS, recorded at a photon energy of 723 eV with and without the YAG alignment laser. The detector is gated to the time-of-flight peak of F^+. The polarization directions of FEL and YAG laser lie along y. The integrated number of detector hits is doubled when the YAG laser is present. A two-dimensional fit of a Lorentz function to the central peak in (b) has been subtracted, resulting in the image in (c). These are the same data as presented in Figs. 4.8(c) to 4.8(f).

E_{kin} [eV]	with YAG laser	without YAG laser	ϱ_1	outer peaks	central peak	ϱ_2
31	11270	5310	0.47	1916	7098	0.27
36	3626	2085	0.58	830	2166	0.38
46	3781	2321	0.61	555	2308	0.24
51	4928	4316	0.86	-	-	-
62	9215	5349	0.58	1689	5793	0.29

Table A.1: Number of ion hits on the detector divided by 10^3, with and without the YAG alignment laser, and in the central and the outer peaks in the image recorded with the YAG laser. The background from residual water in the chamber has been subtracted. For the case of 51 eV electrons, the high voltage on the drift tube on the ion side of the spectrometer broke down during the measurement, thus the central peak could not be fitted well and the number of detector hits may not be fully reliable.

$$\varrho_1 = \frac{\text{number of detector hits without YAG laser}}{\text{number of detector hits with YAG laser}} \tag{A.1}$$

as obtained from the images in Figs. A.1(a) and A.1(b) can provide an estimate of the fraction of molecular clusters. Table A.1 summarizes the results for the five data sets recorded at different kinetic energies of the photoelectron E_{kin}. Alternatively, the ratio

$$\varrho_2 = \frac{\text{number of detector hits in outer peaks with YAG laser}}{\text{number of detector hits in central peak with YAG laser}} \tag{A.2}$$

can be evaluated, the resulting values are also given in Tab. A.1. According to the values of ϱ_1, about $40-50\%$ of the detector hits stem from F^+ fragments that originate from ionization of molecular clusters, according to ϱ_2 even $60-80\%$ of the hits. It is however not known, how the fragmentation of a pFAB cluster after inner-shell ionization differs from the fragmentation of a free molecule. The emission of a singly charged fluorine atom from an ionized cluster may be less likely than emission from an isolated molecule, as within the cluster more possibilities exist to transfer the charge to other atoms. The numbers given in Tab. A.1 therefore can only provide a qualitative estimate and should be interpreted as a rough upper limit for the ratio of free molecules to molecules bound in clusters.

Moreover, not only the ion images but also the simultaneously recorded photoelectrons can be exploited to extract information on the number of molecular clusters, when complemented with DFT calculations. The calculated photoionization cross sections of aligned pFAB molecules, σ_{al}, and of randomly oriented molecules, σ_{rdm}, are different in the energy range investigated here, as was shown in the ratio in Fig. 4.14 and is shown for the partial cross section in Fig. A.2. When unaligned molecular clusters are present, the overall ionization probability for the data recorded with the YAG laser thus does not correspond to the calculated cross section for

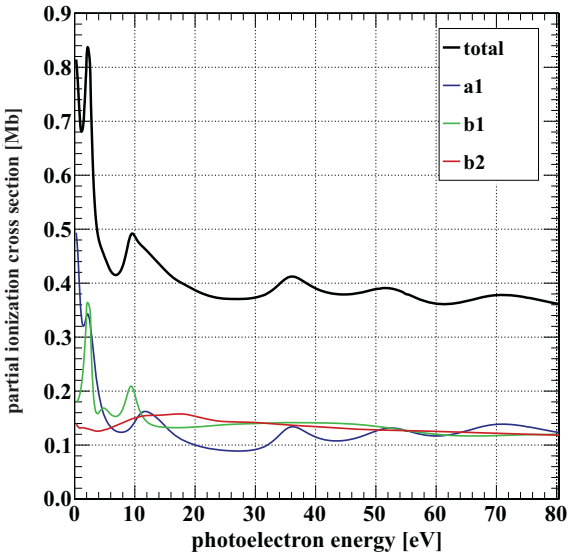

Figure A.2: Calculated photoionization cross sections for the F($1s$) level in pFAB. For the partial ionization cross sections, the molecules are assumed to be perfectly three-dimensionally aligned. The X-ray polarization direction is along y. a1 corresponds to pFAB molecules in the (x, y) detector plane with the major molecular axis along y, b1 corresponds to pFAB molecules in the (x, y) plane with the major molecular axis along x, and b2 corresponds to pFAB molecules in the (x, z) plane with the major molecular axis along x.

aligned molecules, but results from the sum of aligned and randomly oriented ionization cross sections with unknown relative contributions. The number of aligned, single molecules, n, and the number of unaligned molecules in clusters, n_{cl} determine the total number of electron hits in the photoline, referred to as N_{on} for data recorded with the YAG laser, and N_{off} for data recorded without the alignment laser.

$$N_{\mathrm{on}} = \sigma_{\mathrm{al}}\, n + \sigma_{\mathrm{rdm}}\, n_{\mathrm{cl}} \tag{A.3}$$

$$N_{\mathrm{off}} = \sigma_{\mathrm{rdm}}\, n + \sigma_{\mathrm{rdm}}\, n_{\mathrm{cl}}. \tag{A.4}$$

The ratio between single molecules and molecules bound in clusters can then be derived as

$$\varrho_3 = \frac{n}{n_{\mathrm{cl}}} = \frac{N_{\mathrm{off}}\,\sigma_{\mathrm{rdm}} - N_{\mathrm{on}}\,\sigma_{\mathrm{rdm}}}{N_{\mathrm{on}}\,\sigma_{\mathrm{rdm}} - N_{\mathrm{off}}\,\sigma_{\mathrm{al}}}. \tag{A.5}$$

All relevant numbers for the different recorded photoelectron energies are listed in Tab. A.2.[1] For the case of 46 eV electrons, the calculated cross section ratio is < 1 but the experimental ratio is > 1, and for the case of 62 eV electrons the data does not match the calculation, see also Fig. 4.14, thus the resulting ratios ϱ_3 are unphysical. The remaining values suggest that $50 - 80\%$ of the molecules that are photoionized

[1] As the aligned molecules are not perfectly fixed in space, σ_{al} is not the value of a1 as derived from Fig. A.2, but it was recalculated with DFT for the experimentally achieved degree of alignment for the five measured energies.

E_{kin} [eV]	N_{on}	N_{off}	N_{on} / N_{off}	σ_{al}	σ_{rdm}	σ_{al} / σ_{rdm}	ϱ_3	ϱ_4
31	2592	2742	0.945	309.4	380.5	0.8133	0.41	0.11
36	1630	1765	0.923	290.9	370.7	0.7849	0.55	0.30
46	862	853	1.010	404.3	412.3	0.9804	-0.35	0.10
51	1774	1801	0.985	344.9	385.5	0.8946	0.17	0.10
62	1883	1924	0.978	390.8	390.9	0.9996	-1.02	0.05

Table A.2: Number of electron hits in a radial region of interest around the outer edge of the photoline, divided by 10^3, recorded with and without the YAG alignment laser. Calculated ionization cross sections are given in kb.

when the YAG laser is present are in fact randomly oriented. It is however unclear, whether it is valid to assume that σ_{rdm} is identical for free molecules and molecules in clusters.

Finally, the shape of the experimentally obtained difference photoelectron angular distributions (ΔPADs, see section 4.3) can be used to determine the number of randomly oriented molecules. The experimental PADs, recorded with and without the YAG, $I_{on}(\phi)$ and $I_{off}(\phi)$, result from the sum of aligned and randomly oriented PADs, I_{al} and I_{rdm}, depending on the number of free molecules n and molecules bound in clusters n_{cl}.

$$N_{on}\, I_{on}(\phi) = n\, I_{al}(\phi) + n_{cl}\, I_{rdm}(\phi) \tag{A.6}$$

$$N_{off}\, I_{off}(\phi) = n\, I_{rdm}(\phi) + n_{cl}\, I_{rdm}(\phi) \tag{A.7}$$

When comparing the experimentally obtained $\Delta\mathrm{PAD}_{exp} = N_{on}\, I_{on}(\phi) - N_{off}\, I_{off}(\phi)$ to calculations, the calculated PADs are normalized to the experimentally obtained number of hits N_{on}, N_{off} and then subtracted. When the contribution of clusters is not taken into account, this would result in a calculated $\Delta\mathrm{PAD}_{ideal} = N_{on}\, I_{al}(\phi) - N_{off}\, I_{rdm}(\phi)$, which significantly overestimates the magnitude of the expected difference and can even alter the shape of the ΔPAD. Instead, $\Delta\mathrm{PAD}_{calc} = N_{on}\, I_{on}(\phi) - N_{off}\, I_{off}(\phi)$ needs to be calculated. Figure A.3, demonstrates the evolution of the calculated ΔPADs for the five different electron energies when varying the ratio

$$\varrho_4 = \frac{n}{n_{cl}} \tag{A.8}$$

from ($n = 1$, $n_{cl} = 0$) to ($n = 0.1$, $n_{cl} = 0.9$) in steps of 0.1. The resulting ratios that are plotted in Fig. 4.13 for comparison with the experimental data are listed in Tab. A.2. They suggest that $70 - 90\%$ of the molecules are randomly oriented. In summary, it can be stated that although the ratios obtained with the different methods differ, and the considerations are not expected to produce reliable absolute values, overall they all suggest that a significant number of molecules were bound in molecular clusters.

Figure A.3: Calculated ΔPADs for pFAB. Top to bottom: increasing electron kinetic energies of 31, 36, 46, 51, and 62 eV. Left to right: increasing amount of clusters in the molecular beam, from ($n = 1$, $n_{\mathrm{cl}} = 0$) to ($n = 0.1$, $n_{\mathrm{cl}} = 0.9$) in steps of 0.1. The radial scale is identical for all images of one electron kinetic energy.

A.2 Results of Density Functional Theory Calculations

Additional, non-averaged molecular-frame photoelectron angular distributions calculated from density functional theory for different photoelectron energies are shown in Figs. A.4 and A.5. Figure A.4 shows MFPADs for ionization of the fluorine 1s level in perfectly oriented pFAB molecules for different photoelectron kinetic energies. The results of symmetrizing these distributions, corresponding to perfectly aligned molecules, are plotted in Fig. A.5. Also shown are results of averaging over a Gaussian axes distribution with a width of $\sigma = 20°$.

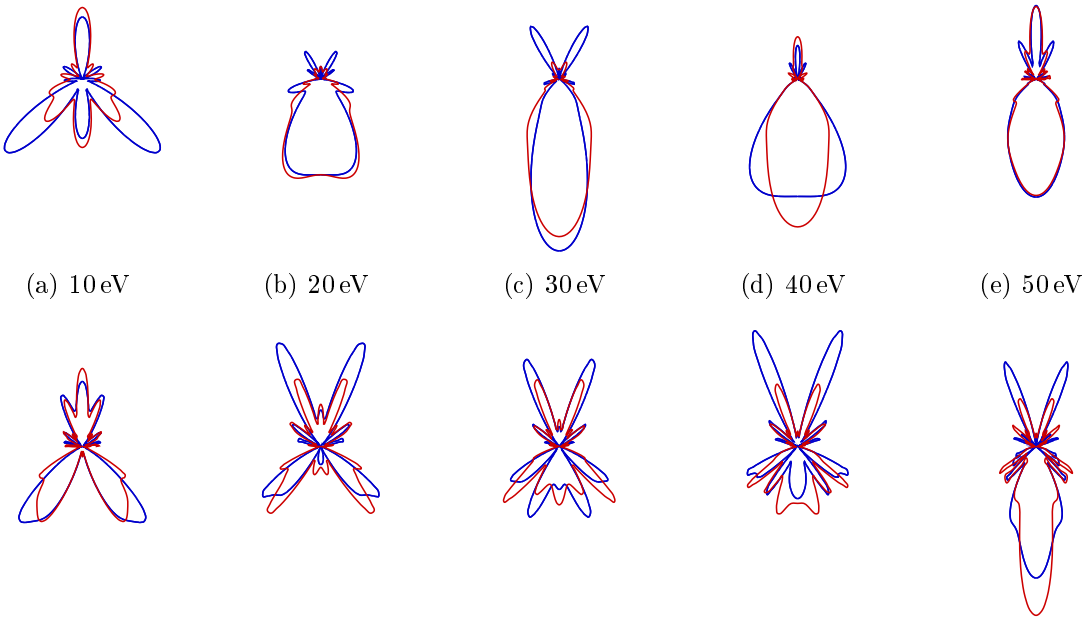

(a) 10 eV (b) 20 eV (c) 30 eV (d) 40 eV (e) 50 eV

(f) 60 eV (g) 70 eV (h) 80 eV (i) 90 eV (j) 100 eV

Figure A.4: Calculated MFPADs for F(1*s*) ionization of pFAB for different electron kinetic energies. Blue: 3d-orientation, red: 1d-orientation. The fluorine is located on the bottom.

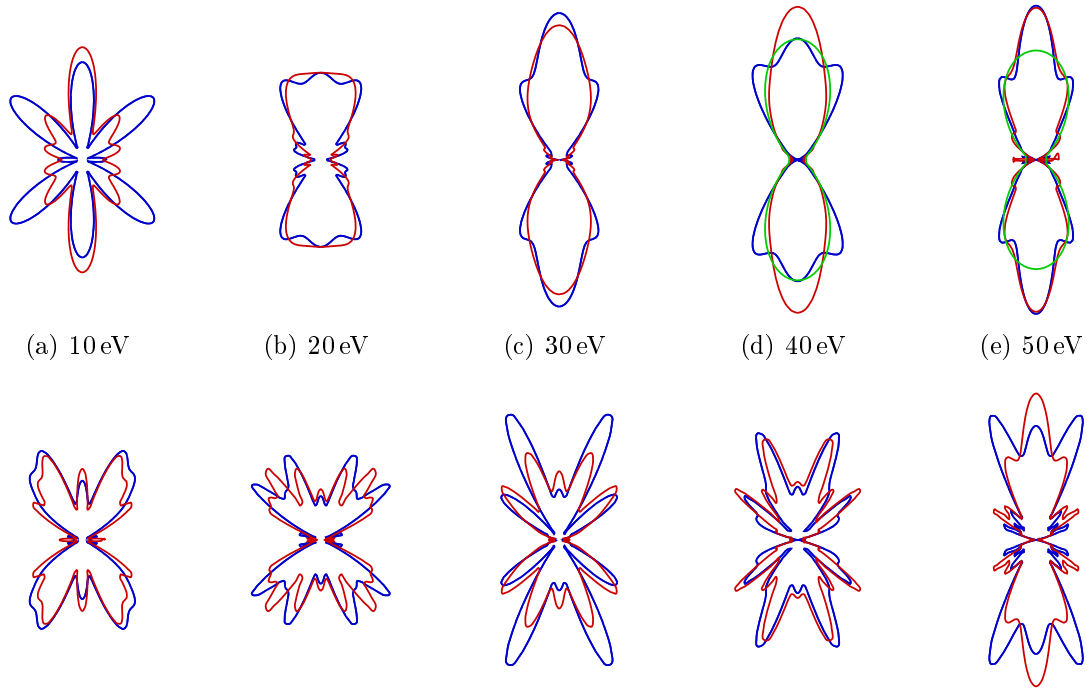

(a) 10 eV (b) 20 eV (c) 30 eV (d) 40 eV (e) 50 eV

(f) 60 eV (g) 70 eV (h) 80 eV (i) 90 eV (j) 100 eV

Figure A.5: Calculated MFPADs for F(1*s*) ionization of pFAB for different electron kinetic energies. Blue: 3d-alignment, red: 1d-alignment, green: 1d-alignment with $\langle \cos^2\theta_{2D} \rangle = 0.89$.

A.3 Experimental Parameters

Additional technical parameters are given for the three different experiments presented in this thesis. In section A.3.2 only parameters are listed that are different from the ones given in section A.3.1. Details for individual data sets are given in Tab. A.3

A.3.1 LCLS Experiment on pFAB Molecules, 2011

LCLS

- repetition rate: 120 Hz
- photon energy: 723 - 754 eV
- pulse length: $\sim$80fs
- pulse energy: 0.7 - 1.3 mJ
- spot size: 50x50 μm^2 FWHM
- bandwidth: 0.2 - 1.0 % [120]

Nd:YAG Alignment Laser

- model: Spectra Physics Quanta Ray Pro 270-50
- repetition rate: 30 Hz
- photon energy: 1.17 eV
- wavelength: 1064 nm
- pulse length: 10 ns
- pulse energy: 500 mJ
- spot size: 70x70 μm^2 FWHM
- intensity: $\sim 5 \times 10^{11}$ W/cm^2

Molecular Beam

- 1-ethynyl-4-fluorobenzene, C_8H_5F
- carrier gas: helium, 50 bar
- repetition rate: 60 Hz
- length of deflector: 24 cm

Other

- phosphor screen: Photonis APD 2 PS 75/32/25/8 D 60:1 NR P20
- MOSFET push-pull switch: Behlke HTS 31-03-GSM
- CCD camera: Adimec Opal-1000
- gate length ions: 168 ns
- gate length electrons: 168 ns

A.3.2 LCLS Experiment on DBB Molecules, 2010

LCLS

- repetition rate: 60 Hz
- photon energy: 1572 eV, 1587 eV
- pulse length: 100 fs
- pulse energy: 3 mJ
- beam waist: $\omega_0 = 30\mu$m

Nd:YAG Alignment Laser

- pulse energy: 300 mJ
- beam waist: $\omega_0 = 65\mu$m
- intensity: $\sim 3\times 10^{11}\,\mathrm{W/cm^2}$

Ti:Sapphire Pump Laser

- repetition rate: 60 Hz
- photon energy: 1.55 eV
- wavelength: 800 nm
- pulse length: 70 fs
- pulse energy: ~ 2 mJ
- beam waist: $\omega_0 = 50\mu$m
- intensity: $\sim 10^{14}\,\mathrm{W/cm^2}$

Molecular Beam

- 1,4-dibromobenzene, $C_6H_4Br_2$, Sigma-Aldrich, 98% purity
- carrier gas: helium, 50 bar
- repetition rate: 60 Hz
- nozzle diameter: 150 μm
- nozzle opening time: 10 μs
- nozzle temperature: 55 °C
- skimmer: BeamDynamics model 50.8, diameter 4 and 2 mm

Other

- delay line anode: Roentdek DLD-80
- gate length ions: 400 ns
- gate length electrons: 900 ns
- width of slit on bottom side of spectrometer: 0.5 mm
- extraction field: 260 V/cm

A.3.3 PETRA Experiment on pFAB Molecules, 2013

PETRA

- repetition rate: 125 MHz
- photon energy: 765 eV
- spot size: $\sim 50\,\mu\mathrm{m} \times 3$ mm

Molecular Beam

- 1-ethynyl-4-fluorobenzene, C_8H_5F
- carrier gas: helium, 200 mbar
- repetition rate: continuous

	electron energy [eV]	photon energy [eV]	pulse energy [mJ]	DTT [kV]	L2T [kV]	L1T [kV]	L1B [kV]	L2B [kV]	DTB [kV]	radial range [pixels]	$\langle \cos^2 \theta_{2D} \rangle$
pFAB PETRA	73	765		−9.00	−9.01	−1.36	+2.90	+6.27	+9.00		
pFAB	31	723.2	0.69	+4.50	+2.48	+0.40	−1.05	−3.60	−4.50	270-320	0.89
LCLS	36	728.4	0.75	+4.50	+2.25	+0.53	−1.05	−2.55	−4.50	240-290	0.80
	46	738.2	0.68	+6.00	+3.30	+0.53	−1.40	−4.80	−6.00	300-330	0.78
	51	743.3	1.23	+6.00	+3.32	+0.68	−1.37	−3.32	−6.00	320-360	
	62	753.8	0.83	+7.00	+3.50	+0.62	−1.63	−5.00	−7.00	325-360	0.83
DBB LCLS	20	1570	3.00	+3.00	+1.70	+0.57	−0.35	−1.50	−3.00	140-230	0.78

Table A.3: Overview of the experimental parameters. T: top side of VMI, B: bottom side of VMI, L1: first electrostatic lens, closest to interaction point, L2: second lens, DT: drift tube, see also Figs. 3.1 and 3.4. The radial range in pixels denotes the integration region for the raw data.

B Bibliography

[1] *A Horse's Motion Scientifically Determined*, Scientific American **29**, 241 (1878).

[2] P. S. Skell and J. G. Traynham, *Radical brominations of alkyl bromides and the nature of beta-bromoalkyl radicals*, Accounts of Chemical Research **17**, 160 (1984).

[3] M. J. Paterson, M. A. Robb, L. Blancafort, and A. D. DeBellis, *Mechanism of an exceptional class of photostabilizers: a seam of conical intersection parallel to excited state intramolecular proton transfer (ESIPT) in o-hydroxyphenyl-(1,3,5)-triazine*, The Journal of Physical Chemistry A **109**, 7527 (2005).

[4] C. L. Huang, J. C. Jiang, A. M. Mebel, Y. T. Lee, and C. K. Ni, *Photodissociation dynamics of fluorobenzene*, Journal of the American Chemical Society **125**, 9814 (2003).

[5] R. S. Judson and H. Rabitz, *Teaching lasers to control molecules*, Physical Review Letters **68**, 1500 (1992).

[6] A. Assion, *et al.*, *Control of Chemical Reactions by Feedback-Optimized Phase-Shaped Femtosecond Laser Pulses*, Science **282**, 919 (1998).

[7] T. Brixner and G. Gerber, *Femtosecond polarization pulse shaping*, Optics Letters **26**, 557 (2001).

[8] H. Kang, K. T. Lee, B. Jung, Y. J. Ko, and S. K. Kim, *Intrinsic Lifetimes of the Excited State of DNA and RNA Bases*, Journal of the American Chemical Society **124**, 12958 (2002).

[9] *Reaction Coordinate*, in *IUPAC Compendium of Chemical Terminology*, edited by M. Nič, J. Jirát, B. Košata, A. Jenkins, and A. McNaught (Blackwell Scientific Publications, Oxford, 2009) 2nd ed.

[10] *http://www.nobelprize.org/nobel_prizes/chemistry/laureates/1999/* (2014).

[11] H. Ihee, *et al.*, *Direct Imaging of Transient Molecular Structures with Ultrafast Diffraction*, Science **291**, 458 (2001).

[12] A. H. Zewail, *Femtochemistry: Atomic-Scale Dynamics of the Chemical Bond*, The Journal of Physical Chemistry A **104**, 5660 (2000).

[13] L. P. H. Schmidt, T. Jahnke, A. Czasch, M. Schöffler, H. Schmidt-Böcking, and R. Dörner, *Spatial Imaging of the H_2^+ Vibrational Wave Function at the Quantum Limit*, Physical Review Letters **108**, 073202 (2012).

[14] Z. R. Grabowski, K. Rotkiewicz, and W. Rettig, *Structural Changes Accompanying Intramolecular Electron Transfer: Focus on Twisted Intramolecular Charge-Transfer States and Structures*, Chemical Reviews **103**, 3899 (2003).

[15] O. Björneholm, *et al.*, *Doppler splitting of in-flight Auger decay of dissociating oxygen molecules: The localization of delocalized core holes*, Physical Review Letters **84**, 2826 (2000).

[16] B. Erk, *et al.*, *Ultrafast Charge Rearrangement and Nuclear Dynamics upon Inner-Shell Multiple Ionization of Small Polyatomic Molecules*, Physical Review Letters **110**, 053003 (2013).

[17] T. Osipov, *et al.*, *Photoelectron-Photoion Momentum Spectroscopy as a Clock for Chemical Rearrangements: Isomerization of the Di-Cation of Acetylene to the Vinylidene Configuration*, Physical Review Letters **90**, 233002 (2003).

[18] A. Stolow, A. E. Bragg, and D. M. Neumark, *Femtosecond Time-Resolved Photoelectron Spectroscopy*, Chemical Reviews **104**, 1719 (2004).

[19] J. Ullrich, R. Moshammer, A. Dorn, R. Dörner, L. P. H. Schmidt, and H. Schmidt-Böcking, *Recoil-ion and electron momentum spectroscopy: reaction-microscopes*, Reports on Progress in Physics **66**, 1463 (2003).

[20] Y. H. Jiang, *et al.*, *Ultrafast Extreme Ultraviolet Induced Isomerization of Acetylene Cations*, Physical Review Letters **105**, 263002 (2010).

[21] H. N. Chapman, *et al.*, *Femtosecond X-ray protein nanocrystallography*, Nature **470**, 73 (2011).

[22] J. Küpper, *et al.*, *X-Ray Diffraction from Isolated and Strongly Aligned Gas-Phase Molecules with a Free-Electron Laser*, Physical Review Letters **112**, 083002 (2014).

[23] W. C. Röntgen, *Über eine neue Art von Strahlen*, Annalen der Physik **300**, 1 (1898).

[24] W. Friedrich, P. Knipping, and M. Laue, *Interferenzerscheinungen bei Röntgenstrahlen*, Annalen der Physik **346**, 971 (1913).

[25] K. J. Gaffney and H. N. Chapman, *Imaging Atomic Structure and Dynamics with Ultrafast X-ray Scattering*, Science **316**, 1444 (2007).

[26] R. Neutze, R. Wouts, D. van der Spoel, E. Weckert, and J. Hajdu, *Potential for biomolecular imaging with femtosecond X-ray pulse*, Nature **406**, 752 (2000).

[27] I. Schlichting and J. Miao, *Emerging opportunities in structural biology with X-ray free-electron lasers*, Current Opinion in Structural Biology **22**, 613 (2012).

[28] N. D. Loh, *et al.*, *Fractal morphology, imaging and mass spectrometry of single aerosol particles in flight*, Nature **486**, 513 (2012).

[29] T. Gorkhover, *et al.*, *Nanoplasma Dynamics of Single Large Xenon Clusters Irradiated with Superintense X-Ray Pulses from the Linac Coherent Light Source Free-Electron Laser*, Physical Review Letters **108**, 245005 (2012).

[30] L. Redecke, *et al.*, *Natively Inhibited Trypanosoma brucei Cathepsin B Structure Determined by Using an X-ray Laser*, Science **339**, 227 (2013).

[31] A. C. Thompson, ed., *X-Ray Data Booklet*, 3rd ed. (Berkeley, CA, 2009).

[32] *NIST Electron Elastic-Scattering Cross-Section Database: Version 3.2* (2013).

[33] M. Chergui and A. H. Zewail, *Electron and X-Ray Methods of Ultrafast Structural Dynamics: Advances and Applications*, ChemPhysChem **10**, 28 (2009).

[34] G. Sciaini and R. J. D. Miller, *Femtosecond electron diffraction: heralding the era of atomically resolved dynamics*, Reports on Progress in Physics **74**, 096101 (2011).

[35] R. J. D. Miller, *Mapping Atomic Motions with Ultrabright Electrons: The Chemists' Gedanken Experiment Enters the Lab Frame*, Annual Review of Physical Chemistry **65**, 583 (2014).

[36] R. J. D. Miller, *Femtosecond Crystallography with Ultrabright Electrons and X-rays: Capturing Chemistry in Action*, Science **343**, 1108 (2014).

[37] C. Hensley, J. Yang, and M. Centurion, *Imaging of Isolated Molecules with Ultrafast Electron Pulses*, Physical Review Letters **109**, 133202 (2012).

[38] T. van Oudheusden, P. L. E. M. Pasmans, S. B. van der Geer, M. J. de Loos, M. J. van der Wiel, and O. J. Luiten, *Compression of Subrelativistic Space-Charge-Dominated Electron Bunches for Single-Shot Femtosecond Electron Diffraction*, Physical Review Letters **105**, 264801 (2010).

[39] J. B. Hastings, *et al.*, *Ultrafast time-resolved electron diffraction with megavolt electron beams*, Applied Physics Letters **89**, 184109 (2006).

[40] Y. Murooka, N. Naruse, S. Sakakihara, M. Ishimaru, J. Yang, and K. Tanimura, *Transmission-electron diffraction by MeV electron pulses*, Applied Physics Letters **98**, 251903 (2011).

[41] H. Delsim-Hashemi, K. Floettmann, M. Seebach, and S. Bayesteh, *Charge Monitors at the Relativistic Electron Gun for Atomic Exploration – REGAE*, in *Proceedings of IBIC2013* (Oxford, UK, 2013) p. 868.

[42] T. Popmintchev, M.-C. Chen, P. Arpin, M. M. Murnane, and H. C. Kapteyn, *The attosecond nonlinear optics of bright coherent X-ray generation*, Nature Photonics **4**, 822 (2010).

[43] P. B. Corkum and F. Krausz, *Attosecond science*, Nature Physics **3**, 381 (2007).

[44] P. Agostini and L. F. DiMauro, *The physics of attosecond light pulses*, Reports on Progress in Physics **67**, 813 (2004).

[45] J. Itatani, *et al.*, *Tomographic imaging of molecular orbitals*, Nature **432**, 867 (2004).

[46] M. Lein, *Molecular imaging using recolliding electrons*, Journal of Physics B **40**, R135 (2007).

[47] C. Lin, A. Le, Z. Chen, T. Morishita, and R. Lucchese, *Strong-field rescattering physics—self-imaging of a molecule by its own electrons*, Journal of Physics B **43**, 122001 (2010).

[48] C. I. Blaga, *et al.*, *Imaging ultrafast molecular dynamics with laser-induced electron diffraction*, Nature **483**, 194 (2012).

[49] M. Meckel, *et al.*, *Laser-Induced Electron Tunneling and Diffraction*, Science **320**, 1478 (2008).

[50] C. S. Fadley, *Diffraction and Holography with Photoelectrons and Fluorescent X-rays*, Progress in Surface Science **54**, 341 (1997).

[51] C. S. Fadley, M. A. Hove, A. Kaduwela, S. Omori, L. Zhao, and S. Marchesini, *Photoelectron and X-ray holography by contrast: enhancing image quality and dimensionality*, Journal of Physics: Condensed Matter **13**, 10517 (2001).

[52] J. Wider, *et al.*, *Atomically Resolved Images from Near Node Photoelectron Holography Experiments on Al(111)*, Physical Review Letters **86**, 2337 (2001).

[53] C. S. Fadley, *Atomic-level characterization of materials with core- and valence-level photoemission: basic phenomena and future directions*, Surface and Interface Analysis **40**, 1579 (2008).

[54] C. S. Fadley, *The Study of Surface Structures by Photoelectron Diffraction and Auger Electron Diffraction*, in *Synchrotron Radiation Research*, edited by Robert Z. Bachrach (Plenum Press, New York, 1992) pp. 421–518.

[55] U. Becker, O. Gessner, and A. Rüdel, *Photoelectron scattering in molecules and fullerenes*, Journal of Electron Spectroscopy and Related Phenomena **108**, 189–201 (2000).

[56] A. Landers, *et al.*, *Photoelectron Diffraction Mapping: Molecules Illuminated from Within*, Physical Review Letters **87**, 013002 (2001).

[57] D. Rolles, *Scattering and Coherence Phenomena in the Photoionization of Small Molecules*, PhD thesis, TU Berlin (2005).

[58] B. Zimmermann, *et al.*, *Localization and loss of coherence in molecular double-slit experiments*, Nature Physics **4**, 649 (2008).

[59] F. Krasniqi, B. Najjari, L. Strüder, D. Rolles, A. Voitkiv, and J. Ullrich, *Imaging molecules from within: Ultrafast angström-scale structure determination of molecules via photoelectron holography using free-electron lasers*, Physical Review A **81**, 033411 (2010).

[60] M. Kazama, *et al.*, *Theoretical study of X-ray photoelectron diffraction for fixed-in-space CO molecules*, Chemical Physics **373**, 261 (2010).

[61] M. Kazama, T. Fujikawa, N. Kishimoto, T. Mizuno, J.-i. Adachi, and A. Yagishita, *Photoelectron diffraction from single oriented molecules: Towards ultrafast structure determination of molecules using X-ray free-electron lasers*, Physical Review A **87**, 063417 (2013).

[62] E. Gagnon, *et al.*, *Soft X-ray-Driven Femtosecond Molecular Dynamics*, Science **317**, 1374 (2007).

[63] F. Kelkensberg, *et al.*, *XUV ionization of aligned molecules*, Physical Review A **84**, 051404 (2011).

[64] J. J. Barton, *Photoelectron Holography*, Physical Review Letters **61**, 1356 (1988).

[65] T. Greber and J. Osterwalder, *Near node photoelectron holography*, Chemical Physics Letters **256**, 653 (1996).

[66] D. Gabor, *A New Microscopic Principle*, Nature **161**, 777 (1948).

[67] L. V. Keldysh, *Ionization in the field of a strong electromagnetic wave*, Soviet Physics JETP **20**, 1307 (1965).

[68] *Atomic Calculation of Photoionization Cross-Sections, http://ulisse.elettra.trieste.it/services/elements/WebElements.html* (2013).

[69] B. H. Bransden and C. J. Joachain, *Physics of atoms and molecules*, 1st ed. (Longman, London, 1983).

[70] J. Campbell and T. Papp, *Widths of the atomic K–N7 levels*, Atomic Data and Nuclear Data Tables **77**, 1 (2001).

[71] J. Zobeley, R. Santra, and L. S. Cederbaum, *Electronic decay in weakly bound heteroclusters: Energy transfer versus electron transfer*, The Journal of Chemical Physics **115**, 5076 (2001).

[72] T. Jahnke, *et al.*, *Ultrafast energy transfer between water molecules*, Nature Physics **6**, 139 (2010).

[73] M. Mucke, *et al.*, *A hitherto unrecognized source of low-energy electrons in water*, Nature Physics **6**, 143 (2010).

[74] J. E. Lennard-Jones, *The electronic structure of some diatomic molecules*, Transactions of the Faraday Society **25**, 668 (1929).

[75] *http://chemwiki.ucdavis.edu/Physical_Chemistry/Quantum_Mechanics/Atomic_Theory/Electrons_in_Atoms/Electronic_Orbitals* (2014).

[76] W. Demtröder, *Experimentalphysik 3: Atome, Moleküle und Festkörper* (Springer, Berlin; Heidelberg, 2003).

[77] C. B. Lang and N. Pucker, *Mathematische Methoden in der Physik* (Elsevier, Spektrum, Akad. Verl., München; Heidelberg, 2005).

[78] T. Suzuki, *Femtosecond Time-Resolved Photoelectron Imaging*, Annual Review of Physical Chemistry **57**, 555 (2006).

[79] J. Cooper and R. Zare, *Angular distribution of photoelectrons*, The Journal of Chemical Physics **48**, 942 (1968).

[80] I. Powis, *Photoelectron circular dichroism of the randomly oriented chiral molecules glyceraldehyde and lactic acid*, The Journal of Chemical Physics **112**, 301 (2000).

[81] I. Powis, *Photoelectron Spectroscopy and Circular Dichroism in Chiral Biomolecules: L-Alanine*, The Journal of Physical Chemistry A **104**, 878 (2000).

[82] D. J. Kennedy and S. T. Manson, *Photoionization of the noble gases: cross sections and angular distributions*, Physical Review A **5**, 227 (1972).

[83] D. Dill, *Fixed-molecule photoelectron angular distributions*, The Journal of Chemical Physics **65**, 1130 (1976).

[84] A. P. Hitchcock and J. Stöhr, *K-shell shape resonances and intramolecular bond lengths. Comments on ''The relationship between shape resonances and bond lengths''*, The Journal of Chemical Physics **87**, 3253 (1987).

[85] T. Seideman, *Time-Resolved Photoelectron Angular Distributions: Concepts, Applications, and Directions*, Annual Review of Physical Chemistry **53**, 41 (2002).

[86] Y.-I. Suzuki, T. Horio, T. Fuji, and T. Suzuki, *Time-resolved photoelectron imaging of S2 -> S1 internal conversion in benzene and toluene*, The Journal of Chemical Physics **134**, 184313 (2011).

[87] T. Seideman, *Time-resolved photoelectron angular distributions as a means of studying polyatomic nonadiabatic dynamics*, The Journal of Chemical Physics **113**, 1677 (2000).

[88] R. Moshammer, *Lecture Notes of the XXXI Heidelberg Physics Graduate Days* (2013).

[89] Y.-K. Kim and J.-P. Desclaux, *Ionization of carbon, nitrogen, and oxygen by electron impact*, Physical Review A **66**, 012708 (2002).

[90] *NIST Electron-Impact Cross Section Database* (2013).

[91] J. E. Sansonetti and W. C. Martin, *NIST Handbook of Basic Atomic Spectroscopic Data* (2013).

[92] M. A. Coplan, J. H. Moore, and J. P. Doering, *(e, 2e) spectroscopy*, Reviews of Modern Physics **66**, 985 (1994).

[93] B. H. Bransden and C. J. Joachain, *Quantum Mechanics*, 2nd ed. (Pearson, Harlow, 2000).

[94] H. Bachau, E. Cormier, P. Decleva, J. E. Hansen, and F. Martin, *Applications of B-splines in atomic and molecular physics*, Reports on Progress in Physics **64**, 1815 (2001).

[95] D. Toffoli, M. Stener, G. Fronzoni, and P. Decleva, *Convergence of the multicenter B-spline DFT approach for the continuum*, Chemical Physics **276**, 25–43 (2002).

[96] M. Stener, G. Fronzoni, and P. Decleva, *Time-dependent density-functional theory for molecular photoionization with noniterative algorithm and multicenter B-spline basis set: CS_2 and C_6H_6 case studies*, The Journal of Chemical Physics **122**, 234301 (2005).

[97] R. Van Leeuwen and E. J. Baerends, *Exchange-correlation potential with correct asymptotic behavior*, Physical Review A **49**, 2421 (1994).

[98] D. Dill and J. L. Dehmer, *Electron-molecule scattering and molecular photoionization using the multiple-scattering method*, The Journal of Chemical Physics **61**, 692 (1974).

[99] A. V. Golovin and N. A. Cherepkov, *Angular distributions of photoelectrons from K-shells of a fixed-in-space CO molecule calculated by the multiple scattering $X\alpha$ method*, Journal of Physics B **35**, 3191 (2002).

[100] F. García de Abajo, M. Van Hove, and C. Fadley, *Multiple scattering of electrons in solids and molecules: A cluster-model approach*, Physical Review B **63**, 075404 (2001).

[101] F. García de Abajo, *Electron Diffraction in Atomic Clusters* (2014).

[102] R. D. Muiño, *et al.*, *Multiple scattering theory for non-spherical potentials: application to photoelectron angular distributions from oriented diatomic molecules and the study of shape resonances*, Journal of Electron Spectroscopy and Related Phenomena **114–116**, 99 (2001).

[103] J. A. Davies, R. E. Continetti, D. W. Chandler, and C. C. Hayden, *Femtosecond Time-Resolved Photoelectron Angular Distributions Probed during Photodissociation of NO_2*, Physical Review Letters **84**, 5983 (2000).

[104] A. Yagishita, K. Hosaka, and J.-I. Adachi, *Photoelectron angular distributions from fixed-in-space molecules*, Journal of Electron Spectroscopy and Related Phenomena **142**, 295 (2005).

[105] K. L. Reid, *Photoelectron angular distributions: developments in applications to isolated molecular systems*, Molecular Physics **110**, 131 (2012).

[106] B. Friedrich and D. Herschbach, *Polarization of molecules induced by intense nonresonant laser fields*, The Journal of Physical Chemistry **99**, 15686 (1995).

[107] H. Stapelfeldt and T. Seideman, *Colloquium: Aligning molecules with strong laser pulses*, Reviews of Modern Physics **75**, 543 (2003).

[108] H. Stapelfeldt, *Alignment of molecules by strong laser pulses*, The European Physical Journal D **26**, 15 (2003).

[109] T. Seideman and E. Hamilton, *Nonadiabatic alignment by intense pulses. Concepts, theory, and directions*, Advances in atomic, molecular, and optical physics **52**, 289 (2006).

[110] R. Torres, R. de Nalda, and J. Marangos, *Dynamics of laser-induced molecular alignment in the impulsive and adiabatic regimes: A direct comparison*, Physical Review A **72**, 023420 (2005).

[111] M. Poulsen, T. Ejdrup, H. Stapelfeldt, E. Hamilton, and T. Seideman, *Alignment enhancement by the combination of a short and a long laser pulse*, Physical Review A **73**, 033405 (2006).

[112] A. Goban, S. Minemoto, and H. Sakai, *Laser-Field-Free Molecular Orientation*, Physical Review Letters **101**, 013001 (2008).

[113] C. Dion, A. Ben Haj-Yedder, E. Cancès, C. Le Bris, A. Keller, and O. Atabek, *Optimal laser control of orientation: The kicked molecule*, Physical Review A **65**, 063408 (2002).

[114] K. Oda, M. Hita, S. Minemoto, and H. Sakai, *All-Optical Molecular Orientation*, Physical Review Letters **104**, 213901 (2010).

[115] S. De, *et al.*, *Field-Free Orientation of CO Molecules by Femtosecond Two-Color Laser Fields*, Physical Review Letters **103**, 153002 (2009).

[116] L. Strüder, *et al.*, *Large-format, high-speed, X-ray pnCCDs combined with electron and ion imaging spectrometers in a multipurpose chamber for experiments at 4th generation light sources*, Nuclear Instruments and Methods in Physics Research A **614**, 483 (2010).

[117] R. W. Schoenlein, *et al.*, *Generation of femtosecond pulses of synchrotron radiation*, Science **287**, 2237 (2000).

[118] B. W. J. McNeil and N. R. Thompson, *X-ray free-electron lasers*, Nature Photonics **4**, 814 (2010).

[119] S. Düsterer, *et al.*, *Femtosecond x-ray pulse length characterization at the Linac Coherent Light Source free-electron laser*, New Journal of Physics **13**, 093024 (2011).

[120] P. Emma, *et al.*, *First lasing and operation of an ångstrom-wavelength free-electron laser*, Nature Photonics **4**, 641 (2010).

[121] T. Ishikawa, *et al.*, *A compact X-ray free-electron laser emitting in the sub-ångström region*, Nature Photonics **6**, 540 (2012).

[122] J. Viefhaus, *et al.*, *The Variable Polarization XUV Beamline P04 at PETRA III: Optics, mechanics and their performance*, Nuclear Instruments and Methods in Physics Research A **710**, 151 (2013).

[123] C. Bostedt, *et al.*, *Ultra-fast and ultra-intense x-ray sciences: first results from the Linac Coherent Light Source free-electron laser*, Journal of Physics B **46**, 164003 (2013).

[124] W. Demtröder, *Molekülphysik: theoretische Grundlagen und experimentelle Methoden* (Oldenbourg, München, 2003).

[125] D. R. Miller, *Free Jet Sources*, in *Atomic and Molecular Beam Methods*, Vol. 1, edited by G. Scoles (Oxford University Press, Oxford, 1988).

[126] W. Demtröder and H.-J. Foth, *Molekülspektroskopie in kalten Düsenstrahlen*, Physikalische Blätter **43**, 7 (1987).

[127] J. P. Toennies and K. Winkelmann, *Theoretical studies of highly expanded free jets: Influence of quantum effects and a realistic intermolecular potential*, The Journal of Chemical Physics **66**, 3965 (1977).

[128] F. Filsinger, *et al.*, *Quantum-state selection, alignment, and orientation of large molecules using static electric and laser fields*, The Journal of Chemical Physics **131**, 064309 (2009).

[129] F. Filsinger, U. Erlekam, G. von Helden, J. Küpper, and G. Meijer, *Selector for Structural Isomers of Neutral Molecules*, Physical Review Letters **100**, 133003 (2008).

[130] U. Even, J. Jortner, D. Noy, N. Lavie, and C. Cossart-Magos, *Cooling of large molecules below 1K and He clusters formation*, The Journal of Chemical Physics **112**, 8068 (2000).

[131] A. T. J. B. Eppink and D. H. Parker, *Velocity map imaging of ions and electrons using electrostatic lenses: Application in photoelectron and photofragment ion imaging of molecular oxygen*, Review of Scientific Instruments **68**, 3477 (1997).

[132] B. Rudek, *Multiple Ionization of Heavy Atoms by Intense X-Ray Free-Electron Laser Pulses*, PhD thesis, University of Heidelberg (2012).

[133] *SIMION 8.0 Industry standard charged particle optics simulation software.*

[134] T. M. Bücking, *Development of a Novel Velocity Map Imaging Spectrometer*, Internship report (DESY, 2013).

[135] I. Ali, *et al.*, *Multi-hit detector system for complete momentum balance in spectroscopy in molecular fragmentation processes*, Nuclear Instruments and Methods in Physics Research Section B **149**, 490 (1999).

[136] J. J. John, *et al.*, *PImMS, a fast event-triggered monolithic pixel detector with storage of multiple timestamps*, Journal of Instrumentation **7**, C08001 (2012).

[137] C. S. Slater, *et al.*, *Covariance imaging experiments using a pixel-imaging mass-spectrometry camera*, Physical Review A **89**, 011401 (2014).

[138] RoentDek Handels GmbH, *COBOLD* (2011).

[139] L. Foucar, *et al.*, *CASS—CFEL-ASG software suite*, Computer Physics Communications **183**, 2207 (2012).

[140] *ROOT - A Data Analysis Framework* (2013).

[141] J. Eland, *The dynamics of three-body dissociations of dications studied by the triple coincidence technique PEPIPICO*, Molecular Physics **61**, 725 (1987).

[142] V. Ayvazyan, *et al.*, *A new powerful source for coherent VUV radiation: Demonstration of exponential growth and saturation at the TTF free-electron laser*, The European Physical Journal D **20**, 149 (2002).

[143] G. A. Garcia, L. Nahon, and I. Powis, *Two-dimensional charged particle image inversion using a polar basis function expansion*, Review of Scientific Instruments **75**, 4989 (2004).

[144] G. G. Paulus, W. Nicklich, H. Xu, P. Lambropoulos, and H. Walther, *Plateau in above threshold ionization spectra*, Physical Review Letters **72**, 2851 (1994).

[145] R. Boll, *et al.*, *Femtosecond photoelectron diffraction on laser-aligned molecules: Towards time-resolved imaging of molecular structure*, Physical Review A **88**, 061402(R) (2013).

[146] R. Boll, *et al.*, *Imaging Molecular Structure through Femtosecond Photoelectron Diffraction on Aligned and Oriented Gas-Phase Molecules*, Faraday Discussions **171**, in press (2014).

[147] D. Davis, D. Shirley, and T. Thomas, *X-ray photoelectron spectroscopy of fluorinated benzenes*, Journal of the American Chemical Society **94**, 6565 (1972).

[148] M. Schürholz, *Pump-Probe Experimente an Molekülen mit intensiven Laserpulsen*, Diplomarbeit, University of Heidelberg (2009).

[149] R. N. Zare, *Dissociation of H2+ by Electron Impact: Calculated Angular Distribution*, The Journal of Chemical Physics **47**, 204 (1967).

[150] R. M. Wood, Q. Zheng, A. K. Edwards, and M. A. Mangan, *Limitations of the axial recoil approximation in measurements of molecular dissociation*, Review of Scientific Instruments **68**, 1382 (1997).

[151] D. W. Lindle, *et al.*, *Angle-resolved photoemission from the Ar 2p subshell*, Physical Review A **38**, 2371 (1988).

[152] R. Lucchese, *et al.*, *Polar and azimuthal dependence of the molecular frame photoelectron angular distributions of spatially oriented linear molecules*, Physical Review A **65**, 020702 (2002).

[153] M. Lebech, *et al.*, *Complete description of linear molecule photoionization achieved by vector correlations using the light of a single circular polarization*, The Journal of Chemical Physics **118**, 9653 (2003).

[154] D. Dowek and R. R. Lucchese, *Photoionization Dynamics: Photoemission in the Molecular Frame of Small Molecules Ionized by Linearly and Elliptically Polarized Light*, in *Dynamical Processes in Atomic and Molecular Physics* (Bentham Books, 2012).

[155] L. Holmegaard, *et al.*, *Laser-Induced Alignment and Orientation of Quantum-State-Selected Large Molecules*, Physical Review Letters **102**, 023001 (2009).

[156] M. Stener, S. Furlan, and P. Decleva, *Density functional calculations of photoionization with an exchange-correlation potential with the correct asymptotic behaviour*, Journal of Physics B **33**, 1081 (2000).

[157] D. P. Woodruff and A. M. Bradshaw, *Adsorbate structure determination on surfaces using photoelectron diffraction*, Reports on Progress in Physics **57**, 1029 (1994).

[158] A. S. Sandhu, *et al.*, *Observing the Creation of Electronic Feshbach Resonances in Soft X-ray-Induced O2 Dissociation*, Science **322**, 1081 (2008).

[159] X. Zhou, P. Ranitovic, C. W. Hogle, J. H. D. Eland, H. C. Kapteyn, and M. M. Murnane, *Probing and controlling non-Born–Oppenheimer dynamics in highly excited molecular ions*, Nature Physics **8**, 232 (2012).

[160] M. Krikunova, *et al.*, *Time-resolved ion spectrometry on xenon with the jitter-compensated soft X-ray pulses of a free-electron laser*, New Journal of Physics **11**, 123019 (2009).

[161] F. J. Wuilleumier and M. Meyer, *Pump-probe experiments in atoms involving laser and synchrotron radiation: an overview*, Journal of Physics B **39**, R425 (2006).

[162] M. Meyer, J. T. Costello, S. Düsterer, W. B. Li, and P. Radcliffe, *Two-colour experiments in the gas phase*, Journal of Physics B **43**, 194006 (2010).

[163] P. Kruit, J. Kimman, H. G. Muller, and M. J. Van der Wiel, *Electron spectra from multiphoton ionization of xenon at 1064, 532, and 355 nm*, Physical Review A **28**, 248 (1983).

[164] A. K. Kazansky, I. P. Sazhina, and N. M. Kabachnik, *Effect of partial temporal coherence of XUV pulses in IR-laser-assisted photoionization*, Physical Review A **86**, 033404 (2012).

[165] D. Rolles, *et al.*, *Femtosecond X-Ray Photoelectron Diffraction on Gas-Phase Dibromobenzene Molecules*, Journal of Physics B **47**, in press (2014).

[166] *NIST XCOM: Photon Cross Sections Database* (2014).

[167] J. Ullrich, A. Rudenko, and R. Moshammer, *Free-Electron Lasers: New Avenues in Molecular Physics and Photochemistry*, Annual Review of Physical Chemistry **63**, 635 (2012).

[168] B. Erk, *et al.*, *Inner-shell multiple ionization of polyatomic molecules with an intense x-ray free-electron laser studied by coincident ion momentum imaging*, Journal of Physics B **46**, 164031 (2013).

[169] J. L. Hansen, *et al.*, *Ionization of one- and three-dimensionally-oriented asymmetric-top molecules by intense circularly polarized femtosecond laser pulses*, Physical Review A **83**, 023406 (2011).

[170] Y. Morishita, *et al.*, *Formation mechanisms of multi-charged Kr ions through 2p shell photoionization using a coincidence technique*, Journal of Physics B **39**, 1323 (2006).

[171] *NIST Chemistry WebBook* (2014).

[172] M. R. Bionta, *et al.*, *Spectral encoding of X-ray/optical relative delay*, Optics Express **19**, 21855 (2011).

[173] S. Schorb, *et al.*, *X-ray–optical cross correlator for gas-phase experiments at the LCLS free-electron laser*, Applied Physics Letters **100**, 121107 (2012).

[174] M. Harmand, *et al.*, *Achieving few-femtosecond time-sorting at hard X-ray free-electron lasers*, Nature Photonics **7**, 215 (2013).

[175] B. Erk, *et al.*, *Imaging Charge Transfer in Molecules upon X-ray Photoabsorption*, submitted to Science (2014).

[176] S. K. Son, *Private Communication* (2013).

[177] B. Wales, E. Bisson, R. Karimi, J.-C. Kieffer, F. Légaré, and J. Sanderson, *A coincidence detection algorithm for improving detection rates in coulomb explosion imaging*, Nuclear Instruments and Methods in Physics Research A **667**, 11 (2012).

[178] W. Ackermann, *et al.*, *Operation of a free-electron laser from the extreme ultraviolet to the water window*, Nature Photonics **1**, 336 (2007).

[179] C.-Y. Wu, Y.-J. Wu, and Y.-P. Lee, *Molecular elimination in photolysis of fluorobenzene at 193 nm: Internal energy of HF determined with time-resolved Fourier-transform spectroscopy*, The Journal of Chemical Physics **121**, 8792 (2004).

[180] H. Ebadi and S. Techert, *Private Communication* (2013).

[181] J. A. Syage, *Angle-velocity-resolved measurements of I from CH_3I cluster photodissociation at 266 and 304 nm*, Chemical Physics Letters **245**, 605 (1995).

Acknowledgment

During my doctoral studies, I had the chance to meet many great people who contributed to the thesis at hand, in one way or another. At this point, I would like to thank:

Daniel Rolles, for adopting me as a doctoral student, for patiently answering a thousand questions and for many enjoyable days and nights of physics-related and non-physics-related discussions.

Artem Rudenko, Benjamin Erk and Benedikt Rudek, for teaching me everything I did not know about AMO physics and experiments, and for a wonderful time at beamlines around the world, at Mexican restaurants, barbecues and coffeehouses.

Joachim Ullrich, for inspiring ideas and for supervising this work, even from afar.

Sascha Epp, for bringing me to the photoelectron holography project, even if things turned out differently than expected.

Lutz Foucar, for providing 24/7 emergency data analysis support.

Faton Krasniqi, for explaining and providing his electron scattering code.

All other members of the Max Planck Advanced Study Group, for a great time.

Jochen Küpper, Sebastian Trippel and Stephan Stern, for providing the molecular beam set-up, and for fruitful discussions about how to tame molecules.

Henrik Stapelfeldt and Lauge Christensen, for sharing their knowledge on how to make molecules hold still and for help in interpreting the data.

Arnaud Rouzée, for disciplining the laser pulses and for his insights on how to make detector images look nice.

Piero Decleva and Mauro Stener, for providing the DFT calculations and for their patience when I changed my mind about the parameters multiple times.

Gustavo Garcia, for taking the time to adapt the pBasex code to my data.

The AMO staff at LCLS, in particular Christoph Bostedt, and Ryan Coffee, without whom the experiments would not have been possible.

Selim Jochim, for reading and reviewing this thesis.

Kirsten Vincke, Sadia Bari, and Alvin Shubert, for finding all mistakes and typos in my thesis except the ones that are still in it.

My parents, who encouraged every step I took to become who I am today.

And, most of all, the person who always makes me smile, even when everything goes wrong. The best part of the past three years was that I met you.